UNIVERSITÀ DEGLI STUDI DI MILANO

Catalytic and photocatalytic processes for the production of alternative fuels and chemicals from renewable sources

PhD Course in Industrial Chemistry (XXX cycle)

Supervisor: Prof. Ilenia ROSSETTI

PhD candidate:
Matteo COMPAGNONI

Academic year: 2014-2017

Contents

“An expert is a person who has made all the mistakes that can be made in a very narrow field”

Niels Bohr (1885 – 1962)

1. Hydrogen Production

Introduction - There is a pressing need to underpin the sustainable and economic growth of a biofuel-based industry that can put together the rising fuel demand with environmental issues. Hydrogen is the ideal energy carrier to solve these problems and there is a growing interest for effective alternatives to produce it cleanly and safely from renewable sources [1]. Among the various achievable and renewable feedstocks, bioethanol is considered a promising raw material, because it can be obtained by biomass fermentation and it is expected to be commercially available on a large scale in the near future from 2nd generation biomass [2]. Ethanol Steam Reforming (ESR) is a promising way to produce hydrogen thermochemically, although the process needs thermal input because the reaction is endothermic. The possibility to work at low temperature (LT) is very interesting for this process in order to decrease the thermal energy input, which leads to lower operation costs, and to avoid catalyst deactivation by sintering [3]. Moreover, the carbon monoxide concentration in the outlet gas is strongly reduced by the higher activity of the exothermal Water Gas Shift (WGS) reaction within the whole reaction network. This is a crucial point for process intensification in the production of pure hydrogen, e.g. for application in Fuel Cells. Therefore, the research of catalysts to promote as much as possible the Steam Reforming of Ethanol at Low Temperature (LT-ESR) is very challenging.

1.1. Low Temperature Ethanol Steam Reforming: Ni/M_xO-ZrO_2 catalysts

The ethanol steam reforming reaction network is usually affected by the formation of several by-products, reducing the selectivity to H_2 and sometimes leading to the formation of coke, especially at low temperature where carbon gasification is inhibited [4]. Besides tuning the operating conditions, the use of highly stable catalysts plays a crucial role, overcoming the activity and selectivity aspects, due to the much easier reformation of ethanol with respect to other non-oxygenated traditional substrates such as CH_4 or heavier hydrocarbons [5].

In this part of the PhD project, several catalysts for the LT-ESR (300-500°C) were synthesized and tested. Nickel was chosen as active phase, because of its high activity among non-noble metals, coupled with much lower cost and availability for industrial purposes [6]. However, poor resistance to carbon formation with respect to noble metals, forced to find alternative preparation routes and material formulations because of the tight correlation between the coking phenomena and support properties/metal dispersion [7].

Carbon deposition can occur through three different pathways: i) hydrocarbon decomposition; ii) disproportion of CO (Boudouard reaction); iii) polymerization of olefins. During the LT-ESR, coking occurs mainly by the last two routes, because the former is strongly endothermic, prevailing at higher temperature (650-800°C) [8]. Ethylene is the main olefin generated during the process, by ethanol dehydration over acid sites, while CO disproportion strongly depends on the selectivity of the catalysts [9]. In addition, not only the source but also the nature of the carbon formed is fundamental. Carbon could be formed as ordered (graphitic or filamentous) or amorphous [5].

The support plays a crucial role towards coking resistance [10], thanks to its own acid-base character and to metal-support interactions [11]. The modification of the support properties can be done choosing carriers with different features such as La_2O_3, TiO_2, MgO [12–15], or combining different properties by doping [2]. ZrO_2 has been proposed as support for catalytic reforming of methane [16] and oxygenated compounds [18]. Its beneficial features are attributed to the steam adsorption ability, which promotes activation of water and coke gasification. Strong metal-support interaction can be also achieved when nickel is used as active phase [19]. In addition, the high thermal stability and good redox properties of this oxide allow its use in thermocatalytic processes [20,21]. A possible criticism is represented by its intrinsic acidity, usually of Lewis type, possibly leading to ethanol dehydration and polymerisation to form coke. Doping with alkali and alkali-earth metal oxides can be a valuable way to improve the catalyst stability toward deactivation phenomena [22–25]. Although the CaO doping by traditional synthetic routes demonstrated significant performance at low

temperature [26,27], the influence of the synthetic method and the nature of the dopant remain a critical point. Major drawbacks of traditional synthetic approaches are the long processing time, batch-to-batch procedure and uneasy control over active phase dispersion. By contrast, flame- and aerosol-based processes offer the advantages of simple and often lower cost synthesis, with a continuous production process combined with a short processing time [28].

Flame Spray Pyrolysis (FSP) was employed in this work for the synthesis of the materials, due to its ability to impart strong metal-support interaction and high metal dispersion [29]. These are key points to ensure sufficient resistance to coking for this application. Indeed, the carbides accumulation at the interface between metal particles and support, the main step for the growth of carbon nanofilaments, can be conveniently limited in small Ni particles. Therefore, achieving strong metal-support interaction is a convenient route towards increasing metal dispersion and stabilising the metal particles. The basic doping of the support by means of FSP was also addressed and related to the catalytic results. CaO, MgO and K_2O were chosen as basic promoters for ZrO_2 in order to limit the role of surface acidity on coking. Low operating temperatures (300-500°C) and stoichiometric steam-to-carbon ratio were investigated as very stressing conditions for carbon formation.

1.1.1. Catalyst Synthesis: Flame Spray Pyrolysis

The main preparation method used for catalyst synthesis was Flame Spray Pyrolysis (FSP). This method allows the production of metal oxides with particular features suitable for high and low temperature processes [30–32]. This technique allows to synthesize single and mixed oxides with a high phase purity. It is a one step preparation where in the same time the material is synthesized and calcined. In the beginning, proper salts (precursor) are dissolved in a combustible organic solvent. The solution is then pumped, using a syringe pump, through a capillary needle to the center of a vertical nozzle in the middle of a special designed burner. The end of the needle is skirt by a coaxial flow of oxygen. This intense flow acts both as dispersing agent and as oxidant for the organic fuel. The solution is dispersed in very small droplets and the mixture droplets/O_2 give rise to the main flame, which is surrounded and stabilized by twelve small flames.

The main flame generated is characterized by a different temperature depending on the nature of the solvent, O_2/fuel ratio and on the different flow of the solution or of the gases [30]. Inside the flame the droplets are instantly evaporated and the precursor is thermally decomposed (pyrolysis) generating the first oxide particles. Coalescence and condensation are the main aggregation pathways that occurs that lead to the final oxides powder (Figure 1.1).

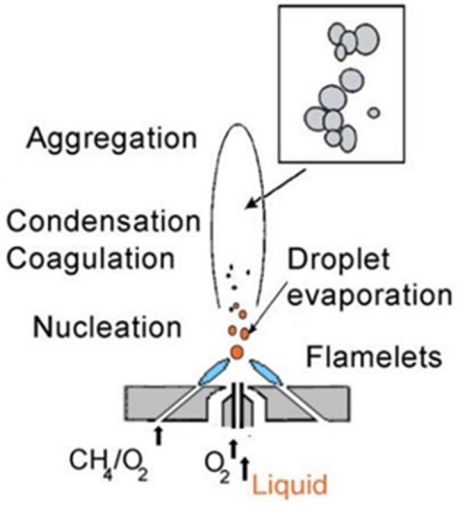

Figure 1.1. Schematic representation of main steps of particle formation and growth into the flame.

The mechanism of particle formation depends case by case on the operating conditions. Solvent volatility is a key parameter. The higher is the evaporation rate of the solvent the higher is the probability that oxide formation proceeds through monomer or cluster formation, whilst slow solvent evaporation can lead to the formation of "eggshell" hollow particles, which are susceptible to breakdown from the explosive evaporation of the residual solvent inside them.

The FSP apparatus is constituted by: 1) the burner; 2) the feeding rate control devices; 3) the collection system for the powder produced. The main flame is ignited and supported by a ring of twelve premixed $O_2 + CH_4$ small flames. Gas flow rates are controlled by MKS Instruments mass flow regulators. Oxygen linear velocity and pressure drop across the nozzle are varied by selecting the proper feeding rate and/or adjusting the nozzle discharge cross-section and geometry. Calibrated manometers provide for control of the oxygen inlet pressure. Another ring of small air-feeding nozzles enables maintenance of an oxidizing atmosphere around the burner and helps convey the product to the powder collection section.

The properties of the prepared material by FSP depends on many different parameters that sometimes contrast with one another. The following are the most representative:

1. **O_2 flow rate to the main nozzle**. The enhancement of O_2 flow rate leads to a higher dispersion degree of the particles within the flame, decreasing the probability of collision between them. Moreover, it has also a quenching effect, decreasing the flame temperature and hence the particle sintering rate and sample crystallinity.

2. **Pressure drop across the nozzle and nozzle geometry.** The geometry of the burner allows the modification of nozzle configuration between convergent to convergent–divergent by

simply moving the inner part of the burner. This influences deeply the pressure across the nozzle and by consequence the discharge velocity and residence time inside the flame. Pressure drop increases by narrowing the nozzle discharge section. The increased O_2 velocity leads to a decrease of flame height, affecting the residence time in the flame.

3. **Nature of the organic solvent and the metal precursor.**
4. **Organic liquid solution flow rate.** Although the productivity of the system is proportional to liquid flow rate, too high rate leads to high concentration of particles produced in the flame which increases the frequency of particle collision and sintering. Therefore, a compromise between productivity and particle size is usually adopted.
5. **Concentration of precursors in the organic liquid solution**. Higher precursor concentration leads to higher powder production per unit time, which means higher productivity. However, precursor solubility limits and high concentration of primary particles in the flame can become critical. High particle concentration favors particle collision and sintering.
6. **O_2 and CH_4 flow rate to the supporting small flames**. The role of the small flames surrounding the main flame is to support and constantly ignite the mixture.

All this parameters were optimized in previous works made in the laboratories of Professor Ilenia Rossetti at Università degli Studi di Milano [30–32] and all the conditions used in the recipe for every catalyst were the optimal ones obtained in the last years.

Preparation of Ni/M_xO-ZrO_2 - Samples were prepared diluting Zirconium acetyl-acetonate (Aldrich, pur. 98%), the alkaline precursor and Nickel (II) acetate tetrahydrate (Aldrich, pur. 98%), in a mixture 1:1 (vol/vol) of o-xylene (Aldrich, pur. >98%) and propionic acid (Aldrich, pur. 97%), with a 0.22 M final concentration. Alkaline precursors were: Calcium acetate (Aldrich, pur. >99%), Magnesium acetate (Aldrich, pur. >99%) and Potassium acetate (Baker, pur. >99%). Preparations were carried out to achieve 10 wt.% Ni loading and 4 wt.% M_xO in the zirconia matrix. The solution was fed to the burner using a 50 ml glass syringe with a flow rate of 2.2 ml/min and a 0.7 bar pressure drop across the nozzle, cofed with 5 L/min of O_2. Ni/M_xO-ZrO_2 catalysts with the following composition were prepared: Ni 10 wt.% / ZrO_2 (labelled as Zr-Ni); Ni 10 wt.%/ CaO 4 wt.% - ZrO_2 (labelled as CaZr-Ni); Ni 10 wt.% / MgO 4 wt.% - ZrO_2 (labelled as MgZr-Ni); Ni 10 wt.% / K_2O 4 wt.% - ZrO_2 (labelled as KZr-Ni). The concentration was selected based on a preliminary screening and based on precursors solubility in the mother solution. The expected value of flame temperature, *ca*. 1500°C, was ensured by the selected propionic acid/o-xylene ratio and the decomposition of

acetate precursors, whose combustion contributes to increase the total combustion enthalpy, and by selecting proper pressure drop across the nozzle (ΔP = 0.7 bar), liquid and oxygen flowrates. The use of acetates as metal precursors was chosen considering their better solubility with respect to nitrate in the selected solvent mixture, and their further contribution to the combustion enthalpy.

Additionally, a precipitation-impregnation technique was used (PC). $Zr(OH)_4$ was prepared by a precipitation method in the laboratories of Professor Michela Signoretto (Università Cà Foscari Venezia). The precipitation was carried out at constant pH of 10. $ZrOCl_2*8H_2O$ (Sigma–Aldrich, purity ≥99.5%) was dissolved in distilled water and added with a peristaltic pump under vigorous stirring to an ammonia (33%, Riedel-de Haën) solution. During the precipitation, the pH value was kept constant at 10.0 ± 0.1 by the continuous addition of a 33% ammonia solution. After the complete addition of the salt solution, the hydroxide suspension was aged for 20 h at 90 °C, then filtered and washed with warm distilled water until it was free from chloride ions ($AgNO_3$ test). The samples were dried overnight at 110 °C. $Zr(OH)_4$ was impregnated with an aqueous solution containing both the metal ($Ni(NO_3)_2*6H_2O$, Sigma–Aldrich, purity ≥98.5%) and the dopants ($Ca(NO_3)_2*4H_2O$, Fluka, purity ≥99%, KNO_3, Fluka, purity ≥99%,) precursors. The active phase (Ni) and the dopants (CaO and K_2O) were added to $Zr(OH)_4$ simultaneously by means of the incipient wetness impregnation technique. Ni was added at the loading of 10 wt.%, whereas CaO and K varied at 9 wt.% (optimal promoter amount on a base of previous work [26]). The samples were dried overnight at 110 °C and finally heated (2 °C/min) up to 500 °C in flowing air (30 mL/min STP) and kept at this temperature for 4 h.

1.1.2. Catalysts characterization

X-ray powder diffraction (XRD) analysis was carried out at room temperature by means of a PHILIPS PW3020 diffractometer with Bragg-Brentano θ-2θ geometry with the CuK radiation (λ = 1.5406 Å). Intensities were collected over a 21° – 90° 2θ range with 0.03° step size and 4 s step time. The apparatus was provided with graphite monochromator. The voltage and current intensity of the generator were set at 40 kV and 30 mA respectively.

The surface area and porosity distribution were determined by N_2 adsorption-desorption at -196 °C using a Micromeritics ASAP 2020 instrument. Surface area was calculated on the basis of the Brunauer, Emmet and Teller equation (BET), while the pores size distribution was determined by the BJH method, applied to the N_2 desorption branch of the isotherm. Prior to the analysis the samples were outgassed at 300°C for 24 hours.

TPR (Temperature Programmed Reduction) measurements were performed by placing the catalyst in a quartz reactor and heating by 10°C min^{-1} from r.t. to 800°C in a 10 vol% H_2/N_2 gas stream flowing at 40 ml/min.

Temperature Programmed Oxidation (TPO) experiments were run placing the spent catalysts in a quartz reactor. The temperature was ramped at a rate of 10 °C min-1 from r.t. to 800 °C in 10 vol% O_2/He gas stream flowing at 40 mL min^{-1}. Deconvolution of the peaks was carried out by means of the Origin Pro 9.0 software. The number of peaks was chosen considering the best fitting of the whole curve using Gaussian functions.

SEM images have been obtained using a Field Emission Gun Electron Scanning Microscopy LEO 1525, after metallization with Cr. Elemental composition was determined using a BrukerQuantax EDS.

TEM images of spent samples have been obtained using a Philips 208 Transmission Electron Microscope. The samples were prepared by putting one drop of an ethanol dispersion of the catalysts on a copper grid pre-coated with a Formvar film and dried in air.

Micro-Raman sampling was made by an OLYMPUS microscope (model BX40) connected to an ISA Jobin–Yvon model TRIAX320 single monochromator, with a resolution of 1 cm^{-1}. The source of excitation was a Melles Griot 25LHP925 He Ne laser that was used in single line excitation mode at 632.8 nm. The power focused on the samples was always less than 2 mW. The scattered Raman photons were detected by a liquid-nitrogen cooled charge coupled device (CCD, Jobin Yvon mod. Spectrum One).

1.1.3. Activity tests

Activity tests were performed by means of a micropilot plant constituted by an Incoloy 800 continuous downflow reactor (i.d. 0.9 cm, length 40 cm), heated by an electric oven. Temperature was controlled by a Eurotherm 3204 TIC. The reactor was fed with gaseous reactants. The catalysts were pressed, ground and sieved into 0.15–0.25 mm particles and *ca.* 0.5 g were loaded into the reactor after dilution 1:3 (vol/vol) with SiC of the same particle size. Catalyst activation was accomplished by feeding 50 cm^3 min^{-1} of a 20 vol% H_2/N_2 gas mixture at 500 °C for 1 h. During activity testing 0.017 cm^3 min of a 3:1 (mol/mol) water/ethanol liquid mixture were fed to the reactor by means of a Hitachi, mod. L7100, HPLC pump, added with 57 cm^3 min^{-1} of N_2, used as internal standard, and 174 cm^3 min^{-1} of He. The liquid mixture was vaporized in the hot inlet of the reactor before reaching the catalyst bed. Such dilution of the feed stream was calibrated so to keep the reactants mixture in the vapor phase even at zero conversion at the reactor outlet. The activity tests

were carried out at atmospheric pressure, with a Gas Hourly Space Velocity (GHSV) of 2700 h^{-1} (referred to the water/ethanol gaseous mixture) at 300, 400 and 500 °C. The testing sequence was carried out starting progressively from the highest temperature in order to avoid possible deactivation by coking of the samples. Analysis of out-flowing gas was performed by a gas chromatograph (Agilent, mod. 7980) equipped with two columns connected in series (MS and Poraplot Q) with a thermal conductivity detector (TCD), properly calibrated for the detection of ethanol, acetaldehyde, acetone, acetic acid, water, ethylene, CO, CO_2, H_2. Repeated analyses of the effluent gas were carried out every hour and the whole duration of every test at each temperature was 8 h. The raw data, expressed as mol/min of each species outflowing from the reactor, have been elaborated as detailed elsewhere [13,19]. Material balance on C-containing products was used as first hand indicator to evaluate coke deposition. Figure 1.2 shows the scheme of the plant.

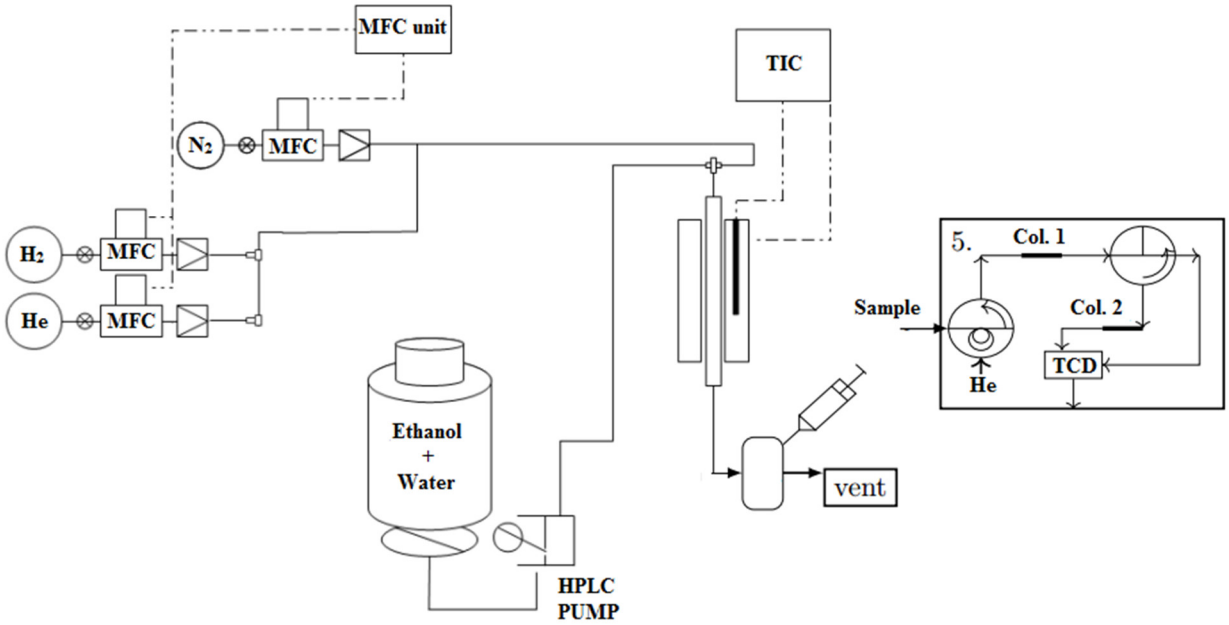

Figure 1.2. Experimental plant used for the activity tests

1.1.4. Results and Discussion

Characterization results - In order to investigate the crystalline phases present in the catalysts, XRD analyses were carried out. XRD patterns of the samples (Figure 1.3) showed only the tetragonal phase of zirconia in the case of Zr-Ni, CaZr-Ni and MgZr-Ni, characterized by the most intense peak at 2θ ≈ 30°, while mixed tetragonal and monoclinic zirconia phases were obtained for KZr-Ni.

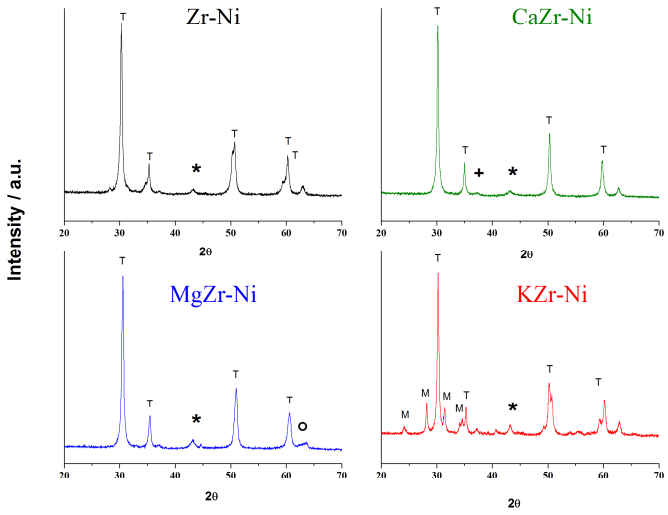

Figure 1.3. XRD patterns of catalysts with various dopants: (*) nickel oxide, (+) calcium oxide, (°) magnesium oxide, (T) tetragonal phase, (M) monoclinic phase of zirconia.

Although the tetragonal stabilization of zirconia after the addition of CaO and MgO is in accordance with the materials prepared by conventional methods [26,33], the presence of the same structure for the undoped sample suggested that the metastable phase can be effectively synthesized by FSP. On the contrary K-promotion led to a mixed phase. The stabilization effect of potassium for zirconia support is not clearly reported in literature. For instance, Li and co-workers reported the stabilization of the monoclinic phase for catalysts prepared by impregnation [34]. Generally, the polymorph phase of the flame prepared materials is tightly related with the residence time and temperature achieved during the synthesis [35], but also the dopant nature is fundamental. Mueller et al. [36], in a study on metal-free zirconia nanoparticles prepared by flame pyrolysis at different production rates, showed the correlation between phase composition and synthetic flame parameters. In particular, they found the highest content of tetragonal phase for the smallest particles and for the fastest quenching of the particles during their formation within the flame. The progressive increase of particle size led to an increase of the monoclinic phase, *i.e.* the stable phase at r.t. and atmospheric pressure for coarse grained zirconia [37]. This effect is known as Gibbs–Thomson effect and it can explain phase

composition of sample KZr-Ni, indeed characterized by larger particle size (*vide infra*). Ni crystal size, calculated from the Scherrer equation, is reported in Table 1.1.

Table 1.1. Textural and morphological properties of the FP prepared catalysts. S_{BET} = BET specific surface area; V_p = pore volume; d_p = mean pore diameter; d_{ZrO2} = ZrO_2 crystal size from XRD; d_{Ni} = NiO crystal size from XRD. [a] obtained by N_2 physisorption; [b] obtained by Sherrer equation; [c] obtained by TPR.

Catalyst	*Composition (wt.%)*			*S_{BET} [a] ($m^2 g^{-1}$)*	*V_p [a] ($cm^3 g^{-1}$)*	*d_p [a] (nm)*	*d_{ZrO2} [b] (nm)*	*d_{Ni} [b] (nm)*	*mol H_2 consumed / mol Ni [c]*
Zr-Ni	Ni - 10	-	ZrO_2	53	0.21	1.00	22	12	1.00
CaZr-Ni	Ni - 10	CaO - 4	ZrO_2	49	0.17	1.00	23	10	1.00
MgZr-Ni	Ni - 10	MgO - 4	ZrO_2	49	0.15	0.45	20	11	0.45
KZr-Ni	Ni - 10	K_2O - 4	ZrO_2	25	0.11	0.96	35	16	0.96

The presence of MgO and CaO crystalline phases revealed their partial segregation. This contrasts with the conclusions reported by Asencios et al. [38] for doped samples prepared by wet methods, where they found only the formation of solid solutions without any dopant crystalline phase. Phase segregation here observed are ascribed to aggregation mechanisms of the precursors inside the flame.

BET/BJH models were employed to calculate the specific surface area (S_{BET}), porosity and pore size distribution of the catalysts and the results are reported in Table 1.1. For all the materials a type IV isotherm was observed, with a characteristic hysteresis of materials containing slit-shaped pores or aggregates of platy particles [39]. These results were consistent with the FSP preparation adopted, which lead to the formation of particles in the nanometric size without large intrinsic mesoporosity [40], directly related to the decomposition mechanism of the oxide precursors within the flame and the subsequent agglomeration [30]. No significant difference between the adsorption/desorption isotherms shape of doped and undoped samples was evidenced. However, almost halved S_{BET} was obtained for KZr-Ni with respect to other samples. This result could be explained by different rearrangements during the particles agglomeration within the flame and by surface covering of potassium oxides produced at high temperature, in accordance with Pratsinis and co-workers [41], who revealed this effect for K-Rh/Al_2O_3 catalysts prepared by FSP for the CO_2 hydrogenation process. Ultimately, the effect can be searched in the different volatility of the alkali and alkali-earth oxides adopted (T_{melt} CaO = 2613°C, T_{melt} MgO = 2825°C, T_{melt} K_2O = 740°C) [42].

H_2-TPR analysis provides a quick characterization to evaluate the effect of a dopant on the reducibility of the active metal oxide. TPR signals are strongly influenced by metal particle size, dispersion and strength of interaction with the support [26,43]. The H_2 consumption due to the reduction of the support was ruled out in agreement with the analysis of bare ZrO_2 [44] and the H_2 consumption quantification is reported in Table 1.1. The reduction patterns during temperature

increased showing differences in the NiO reduction profiles depending on the promoters added to the zirconia support (Figure 1.4).

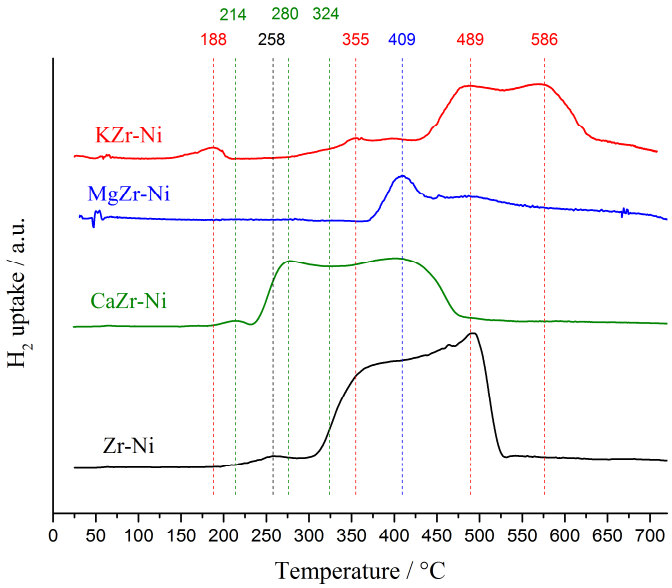

Figure 1.4. H_2-TPR profiles of the FSP catalysts prepared with different basic promoters.

In the Zr-Ni TPR profile two main peaks were detected, due to NiO strongly and weakly interacting with the zirconia support [45], *i.e.* a sharp peak at 489°C and a shoulder at 385°C, respectively. The weak signal at 258°C was ascribed to a very small amount of NiO very poorly interacting with the support and aggregated in larger particles.

CaZr-Ni was characterized by two different peaks. A broad one was obtained by the overlap of two different peaks localized at 280 and 409 °C. The former was attributed to NiO interacting with ZrO_2 influenced by oxygen vacancies due to the presence of CaO in the zirconia framework, as extensively explained elsewhere [26,46]. The latter was attributed to the NiO only interacting with bare ZrO_2. This means that doping with CaO by FSP led to the same effect of partial substitution Zr^{4+}/Ca^{2+} achieved by the traditional impregnation preparation route and, in such case, positively affecting activity and resistance to coking [26].

On the contrary, a broad reduction band in the 370 °C and 700 °C range was detected for MgZr-Ni. The sharper peak at 409 °C was assigned to the reduction of Ni^{2+} species located on the MgO-ZrO_2 surface [39]. The broad band in the range 500 °C – 750 °C was instead related to the reduction of several complex species in a solid solution of NiO-MgO-ZrO_2 (Ni^{2+}–O–Mg^{2+}) in accordance with a study of Garcia *et al.* [33].

Several peaks were detected also in the case of KZr-Ni. This reduction profile is typical when there is not a narrow particle size distribution and several species are reduced. The possible contribution of

K^+ reduction was ruled out considering the quantification of the TPR signals (Table 1.1). XRD patterns, according to the Gibbs-Thomson effect, and BET analysis, according to the lowest S_{BET}, confirm the highest heterogeneity of particle size for this sample considering ZrO_2 particles, and this fact consequently reflected on active phase dispersion as it could be seen in the TPR curve. However, this aspect did not explain peaks at very high reduction temperature (maximum at 586 °C). The latter effect is explained by a strong enhancement of the interaction strength between NiO and ZrO_2 following K doping, in agreement with the stabilization effect of K addition [47] and its direct interaction with the transition metals in the lattice [48].

Scanning Electron Microscopy (SEM) and Transmission Electron Microscopy (TEM) have been used to investigate samples morphology. This allowed deepening the average Ni values of crystal size obtained by XRD, confirming them especially in case of overlapping reflections, as in the case of NiO/Al_2O_3 [3]. The results confirmed that for KZr-Ni a broader particle size dispersion for ZrO_2 support was present. Although for all the other samples the size of NiO particles on the oxide matrix was around 10-20 nm in accordance with the XRD average values, no smaller particles were observed for the K-doped catalyst. In general, a good metal dispersion was achieved at this quite high metal loading. Few large particles (size ≥ 50nm) can be observed in accordance with the weak TPR signals at very low temperatures for every sample.

Catalytic activity testing - To unravel the different possible contributions for the catalyst deactivation, critical steam/ethanol ratio (S/E=3 mol/mol) for coke deposition was chosen, corresponding to the stoichiometric composition. This aspect must be taken into account because also ethanol conversion and H_2 production are related with this important operative parameter. Hydrogen was used as reducing agent during catalyst activation and temperature was chosen below the Tammann temperature of Nickel (590 °C) in order to limit metal sintering. Blank tests were also conducted using a reactor filled only with quartz and SiC. The results were averaged between 4-8 hours, *i.e.* under steady state conditions, for tests at 400 °C and 500 °C, as reported in Table 1.2.

Table 1.2. Activity testing for LT-ESR at 500 °C and 400 °C, 8h time-on-stream, data averaged out between 4-8 h-on-stream, GHSV = 2700 h^{-1}, Steam/Ethanol = 3 mol/mol.

Catalysts	*Zr-Ni*	*CaZr-Ni*	*MgZr-Ni*	*KZr-Ni*	*Equilibrium*
500°C					
EtOH conversion (%)	100 ± 0	100 ± 0	100 ± 0	100 ± 0	100
H_2 productivity (mol min^{-1} kg_{cat}^{-1})	1.04 ± 0.03	1.07 ± 0.10	1.04 ± 0.08	1.16 ± 0.10	1.23
CO/CO_2	0.82 ± 0.14	0.64 ± 0.10	1.13 ± 0.11	0.74 ± 0.04	0.601
C balance (%)	81 ± 3	89 ± 4	83 ± 7	87 ± 2	-
Sel. CH_4 (%)	10.7 ± 1.5	19 ± 2	9.4 ± 1.1	3.97 ± 0.10	33.4
Sel. CH_3CHO (%)	0 ± 0	0 ± 0	0 ± 0	0 ± 0	$1.1\ 10^{-8}$
Sel. CH_2CH_2 (%)	0 ± 0	0 ± 0	0.9 ± 0.9	0 ± 0	$2.2\ 10^{-6}$
400°C					
EtOH conversion (%)	100 ± 0	100 ± 0	53 ± 9	100 ± 0	100
H_2 productivity (mol min^{-1} kg_{cat}^{-1})	0.65 ± 0.04	0.752 ± 0.006	0.23 ± 0.02	1.00 ± 0.05	0.675
CO/CO_2	1.2 ± 0.2	0.2 ± 0.2	1.15 ± 0.08	0.242 ± 0.006	0.093
C balance (%)	56 ± 4	87 ± 4	86 ± 11	84.2 ± 0.7	-
Sel. CH_4 (%)	16 ± 2	37 ± 3	9 ± 2	16.7 ± 0.4	92.1
Sel. CH_3CHO (%)	0 ± 0	0 ± 0	30 ± 4	0 ± 0	$3.3\ 10^{-9}$
Sel. CH_2CH_2 (%)	0 ± 0	0 ± 0	7 ± 1	0 ± 0	$4.0\ 10^{-7}$

The expected equilibrium data were calculated for the chosen operating conditions as reference. They were calculated using the Aspen Plus package choosing a Gibbs reactor and selecting as possibly present species all the observed products and byproducts. Identical products distributions were obtained when simulating the reactor as an Equilibrium block, where selected reactions take place. The proposed reactions were:

$CH_3CH_2OH + H_2O \rightarrow 2\ CO + 4\ H_2$ (1) $\Delta H^0_{298} = +\ 255.2$ kJ mol^{-1} [49]

$CO + H_2O \leftrightarrows CO_2 + H_2$ (2) $\Delta H^0_{298} = -\ 41.2$ kJ mol^{-1} [49]

$CH_3CH_2OH \rightarrow CH_4 + CO + H_2$ (3) $\Delta H^0_{298} = +\ 49.0$ kJ mol^{-1} [49]

$CH_3CH_2OH \rightarrow CH_3CHO + H_2$ (4) $\Delta H^0_{298} = +284.9$ kJ mol^{-1} [50]

$CH_3CH_2OH \rightarrow CH_2CH_2 + H_2O$ (5) $\Delta H^0_{298} = +\ 45.0$ kJ mol^{-1} [51]

$CH_3CHO \rightarrow CH_4 + CO$ (6) $\Delta H^0_{298} = -79.5$ kJ mol^{-1} [50]

According to the results reported in Table 1.2, one may notice that full ethanol conversion is expected at every temperature and that the most favored pathway based on thermodynamic considerations would be reaction 3, leading to methane, which is the most stable compound at low temperature.

At 500°C every catalyst showed full ethanol conversion and equally negligible selectivity to common by-products such as acetaldehyde and ethylene, as prescribed by thermodynamics. However, lower

methane formation was obtained, suggesting that the catalyst would inhibit the bare thermal decomposition route (reaction 3), favoring other intermediate paths towards H_2, CO and CO_2. Considering a possible mechanism for ethanol conversion over metal particles, one may consider adsorption of ethanol, C-C bond cleavage and progressive loss of hydrogen leaving adsorbed CH_x. The latter should be further oxidized by activated oxygen or hydroxyl species, possibly before the formation of carbides, which easily migrate through the metal lattice and are responsible of carbon nanotubes formation. According to this mechanism, we can propose the hypothesis that our catalysts favor a fast oxidative path, inhibiting the recombination possibility between adsorbed CH_3 and H entities. This can explain the lower methane selectivity with respect to thermodynamics.

The absence of ethylene, which is a coke precursor, could be explained in two ways: i) all the ethylene possibly formed through ethanol dehydration is reformated and/or oligomerized to coke over the catalyst surface; ii) the materials adopted had very low activity for ethanol dehydration.

Ethylene was detected in the reactor outlet gases only for the MgZr-Ni sample. At 500 °C and 400 °C, a constant increase of ethylene yield was observed with a decrease of the ethanol conversion for this sample (Figure 1.5).

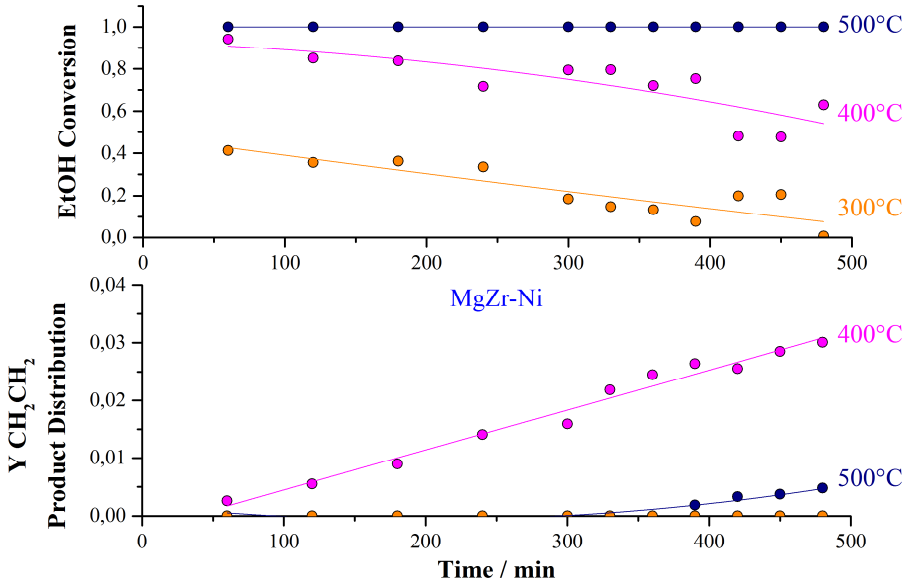

Figure 1.5. Evolution with time-on-stream of ethanol conversion (upper) and ethylene production (lower) for MgZr-Ni at different temperature.

This showed a progressive coking over catalyst surface. The formation of carbon suppressed the steam reforming reaction leading to the lowest hydrogen productivity obtained among all the samples. Moreover, the presence of acetaldehyde, product of dehydrogenation, suggested its incomplete reforming even at 500°C. However, the high C-balance could mean that also alternative deactivation

phenomena were happening. One possibility is the loss of the alkaline promoter during the tests and subsequent enhancement of acidity, progressively increasing ethylene productivity. Alkali loss at temperature higher than 300°C could happen during the steam reforming if the interaction with the support is too weak [52]. This can be a significant problem not only for the stability of the catalyst, but also for the promotion of stress corrosion in stainless steel in the coldest parts of the plant downstream the reactor. Especially in the case of MgO, steam can react with the oxide and volatilize the alkali through formation of the hydroxide (T_{melt} $Mg(OH)_2$ = 350°C [42]) :

$MgO + H_2O \leftrightarrows Mg(OH)_2$ $\Delta H^0_{298} = -81.3$ kJ mol^{-1}

Energy-Dispersive X-ray spectroscopy (EDX) was used to check the Mg loading after use. Figure 1.6 showed that the spent catalyst maintained a good Mg dispersion, without any significant loss of the promoter. This is expected from literature data [52], because the steam partial pressure here used was lower and temperature higher with respect to those needed for hydroxide formation.

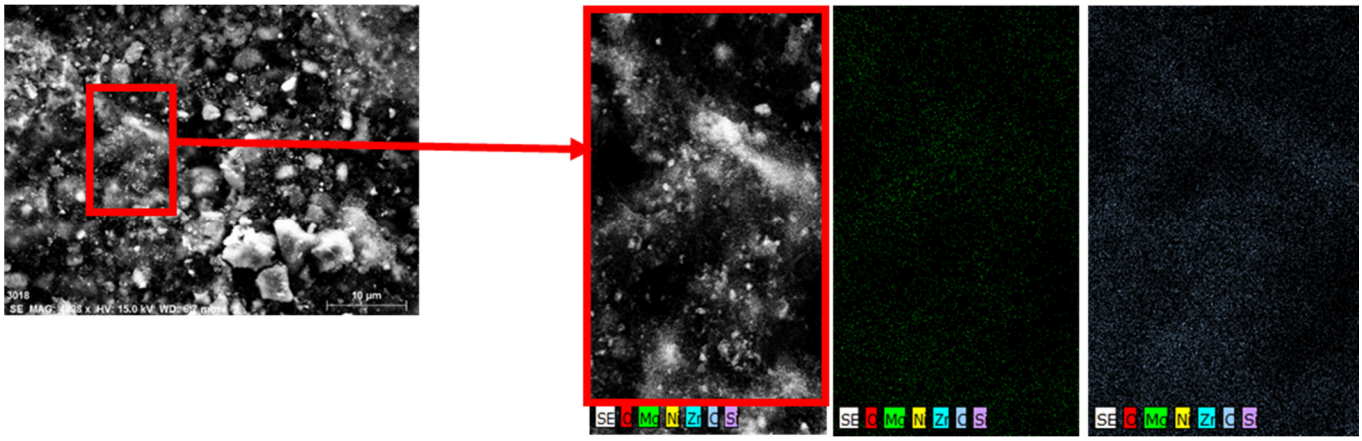

Figure 1.6. Representative elemental mapping images by EDX-SEM of Mg for spent MgZr-Ni.

Another possible cause to interpret the poor activity of the Mg-doped catalyst can be an incomplete activation treatment. TPR profile suggests that the activation by reduction at 500°C did not allow to reduce all the nickel oxide and consequently the activity was reduced. To clarify this point activation at 800°C was also carried out, but no significant increase of hydrogen productivity was detected by repeating the activity test at 500°C. However, quantitative TPR data showed that even at 800°C not all the nickel was reduced. The main reason for low and decreasing activity of the Mg-doped sample was here correlated with the increase of ethylene formation and ascribed to the progressive formation of encapsulating carbon, which progressively deactivated the metal particles.

The incomplete reduction of nickel oxide occurred also in the case of KZr-Ni. K doping led to a strong metal-support interaction, as testified by the highest reduction temperature, and this point can

be associated to the high activity exhibited by this sample. Frusteri et al. very well explained the beneficial role of K, because of the electronic enrichment of the active phase depressing carbon formation [14]. We have also drawn similar conclusions for alkali doped catalysts for different applications [53–55].

The CO/CO_2 ratio can be considered a parameter to evaluate the extent of the Water Gas Shift reaction (WGS, reaction 2). WGS reached nearly equilibrium products distribution at 500°C for the Ca-doped sample (CO/CO_2 ratio in Table 1.2). By contrast, at 400°C the WGS reaction was more favored from a thermodynamic point of view, but more limited kinetically. CaZr-Ni and KZr-Ni revealed the lowest CO/CO_2 ratio and, accordingly, the highest H_2 productivity at such a temperature. The local defect structures formation in the case of CaZr-Ni increase the oxygen-ion conduction and enhance the formation of active oxygen-containing species through water activation [56]. This may favour the oxidative paths with respect to reaction 3, which would be even more thermodynamically favoured at low temperature (higher methane selectivity calculated at equilibrium).
KZr-Ni showed the best performance in terms of H_2 productivity and low CH_4 selectivity. The beneficial impact of K on Ni-based catalyst toward methane activation and inhibition of methanation was in accordance with Rostrup-Nielsen *et al.* [57]. Experimental results confirmed the DFT-calculations concerning the strong dipole moment induced in the transition state of the dissociating methane molecule with an increase of the energy barrier for dissociation of methane and hence the formation of adsorbed carbon atoms, precursors of coke [57].

The apparently low methane selectivity in the case of MgZr-Ni was only due to the high selectivity towards acetaldehyde, and in turn, the increasing selectivity to C_2 by-products can be correlated to Ni deactivation by coking (encaspsulating).

The formation of coke is the most critical point for LT-ESR as mentioned in the introduction. Material balance on C-containing products was checked to quickly quantify coke deposition during the tests. The C balance during blank tests was *ca.* 91% at 500°C and 100% at 400°C. The addition of Ca and K promoters decreased the carbon loss, especially during the tests at 400°C (Table 1.2). The importance of these results increased comparing them with our previous data on other active phases and supports [13,58]. The beneficial role imparted by these dopants concerning the oxygen mobility, the reduction of surface acidity and the improved H_2O and CO_2 adsorption [8,26] were exploited by using the FSP preparation technique. Hydrogen productivity and H_2/CO *vs*. t-o-s are reported in Figure 1.7.

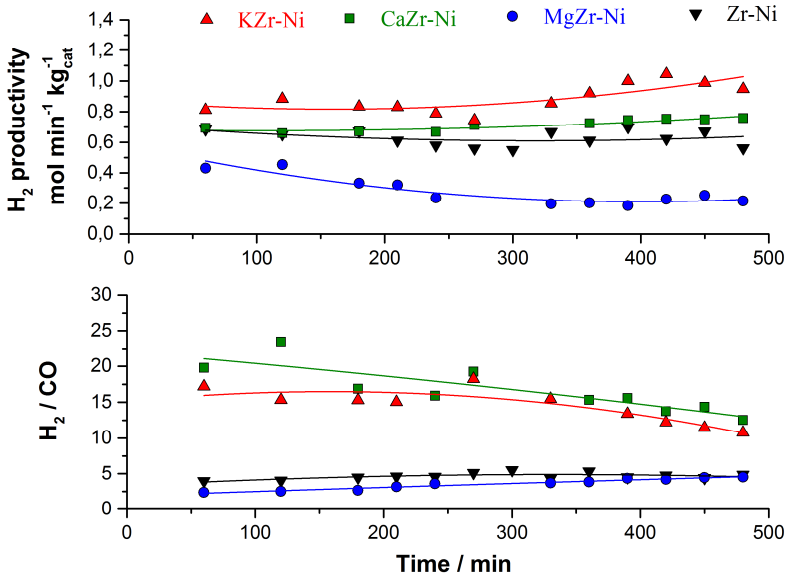

Figure 1.7. H_2 productivity and H_2/CO ratio versus time on stream at 400 °C: S/E = 3 mol/mol; GHSV = 2700 h^{-1}; P = 1 atm.

These parameters are very important because, besides improving H_2 yield, they allow to decrease the impact of the downstream H_2 purification through CO-removal steps, such as the dedicated WSG reactors [59,60]. By contrast, an higher value of CO in the stream means catalysts more suitable for the syngas production dedicated to the Fischer−Tropsch (FT) process, which needs a H_2/CO ratio of approximately 2 to obtain high molecular weight paraffin/olefin liquid transportation fuels [61,62]. CaZr-Ni and KZr-Ni revealed the best H_2 yield and lowest CO productivity. However, a progressive decrease of the H_2/CO ratio at lower temperature, not found for the respective tests at 500 °C, needs explanation. Two possible causes may coexist: i) the progressive decrease of activity toward H_2 formation by WGS and ESR reactions due to deactivation by coking; ii) the progressive increase of the Reverse Boudouard (RB) reaction due to the carbon possibly accumulated (CO_2 + C ⇆ 2CO). The increase of C-balance and the growth of H_2 production ruled out the former hypothesis. The 2nd hypothesis seems the most probable because of the positive effect of alkaline additives to prevent the Boudouard reaction and consequently favour the RB pathway, in agreement with Galetti and co-workers and their study on basic ceria doping [63]. In order to have a clear overview and an explicit comparison of the catalyst performance considering tests not limited by full conversion, a test with the best catalyst KZr-Ni was performed using a tenth of the catalyst weight used in the activity tests previously shown. The resulting Gas Hourly Space Velocity was 13800 h^{-1} and the activity results are reported in Figure 1.8.

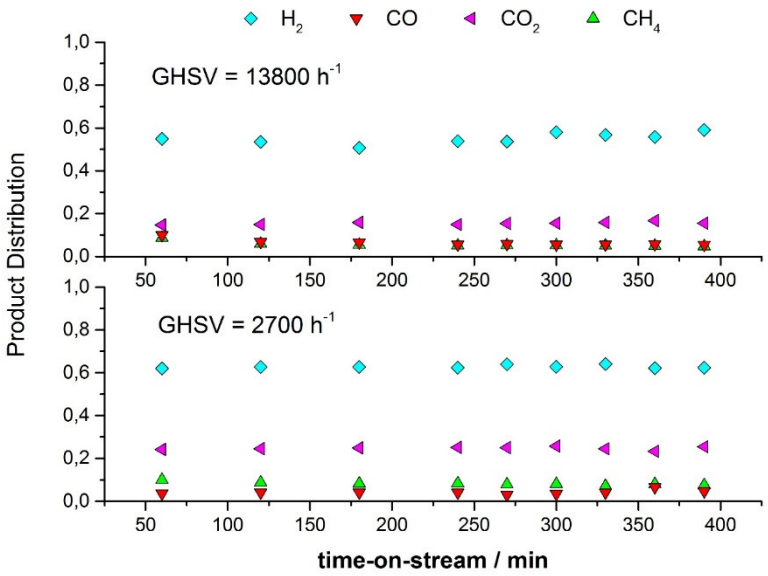

Figure 1.8. Products distribution of sample KZr-Ni considering test with a tenth of catalyst mass with respect to standard testing conditions (GHSV = 13800 h^{-1}, T = 400 °C, S/E = 3 mol/mol, P = 1 atm, Average ethanol conversion = 42 ± 4 %)

The average conversion was 42 ± 4 %. A slightly lower selectivity to hydrogen was obtained, although the general trend and the general good features already discussed above were confirmed.

Then, a more challenging temperature was investigated: 300°C. This reaction temperature is not commonly studied because of the very high catalyst activity necessary to achieve significant H_2 productivity. Usually thermodynamically more favored side reactions occur, such as the ethanol dehydrogenation without subsequent acetaldehyde reforming, or ethanol decomposition/dehydration [8]. Products distributions obtained are reported in Figure 1.9.

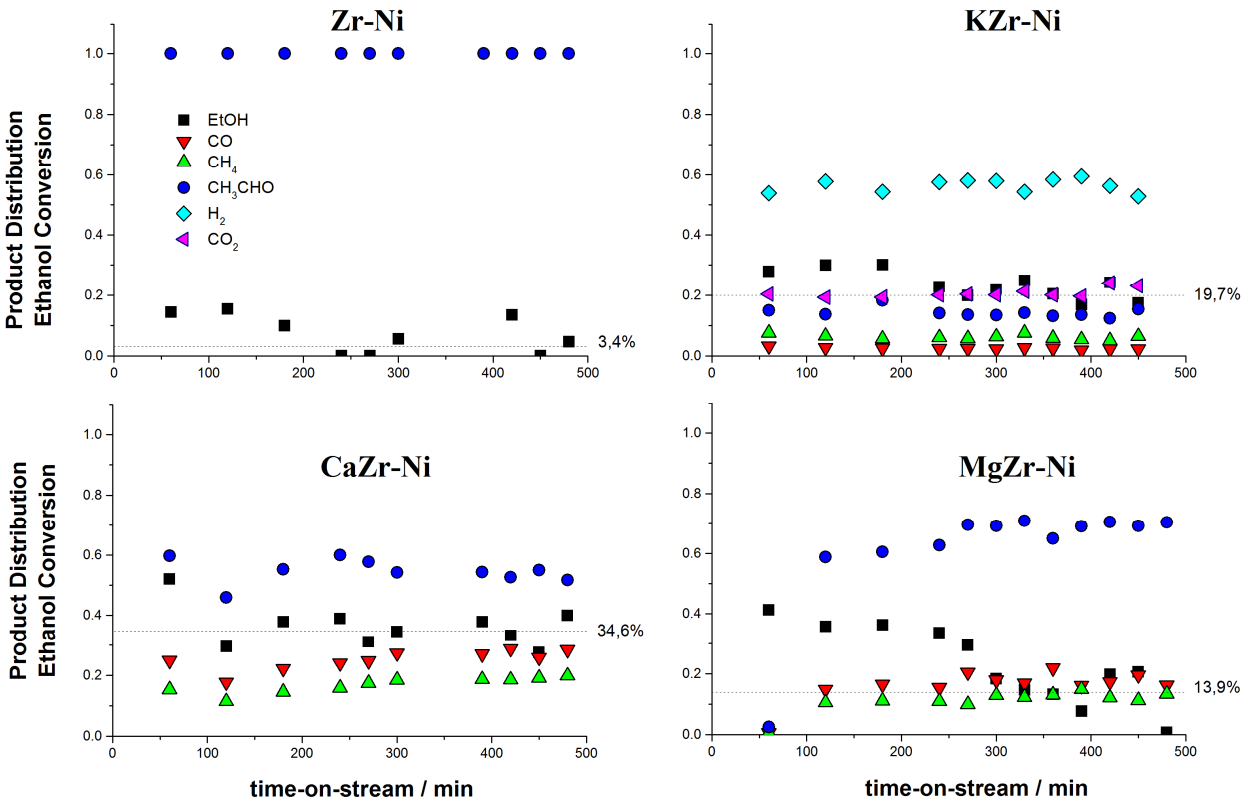

Figure 1.9. Products distribution and ethanol conversion for LT-ESR tests at 300 °C.

Generally, the low temperature ethanol steam reforming is considered divided in two steps: i) dehydrogenation of ethanol to acetaldehyde (reaction 4); ii) decarbonylation of acetaldehyde to form CO and CH_4 (reaction 6) [50].

Zr-Ni confirmed that the first step of ESR was constituted by ethanol dehydrogenation (reaction 4), as acetaldehyde was the only C-product obtained. Mattos et al. evidenced the reaction routes for acetaldehyde on oxide catalysts by means of a comprehensive IR study [8]. One route is the direct decomposition to CO and CH_4 and the other is the hydrogen abstraction from adsorbed acetaldehyde to form acetyl species and their subsequent decomposition leading to $CO_{(g)}$ and CH_3 adsorbed. Adsorbed methyl species have to undergo a further hydrogenation step for the methane evolution or consecutive dehydrogenation to the formation of carbon. The product distribution and carbon balance confirmed the presence of both routes. High resistance toward Boudouard reaction for coke formation was witnessed by the absence of CO_2. This pathway was confirmed by Choong et al., because of the surface oxygen sites modification by using CaO as dopant [64], and confirmed that the surface acidity was not the only property changed by doping with alkaline promoters.

KZr-Ni was the only material still active toward H_2 production at this very low temperature. Products obtained consisted of H_2, CO, CO_2 and CH_4. The presence of CO_2 suggests the acetaldehyde steam reforming reaction, which occurs at lower temperature with respect to ethanol SR using suitable catalysts [8]:

$$CH_3CHO + 3\ H_2O \rightarrow 5\ H_2 + 2\ CO_2 \qquad (7)$$

Under these operating conditions, doping with K led to a catalyst able to achieve the lowest CH_4 selectivity at 300°C. Methane selectivity represents one of the key points in order to obtain a good SR catalyst for low operating temperatures. Indeed, methane is more difficult to reformate with respect to the oxygenated molecules and its presence decreases the hydrogen selectivity. On the other hand methane selectivity is less sensitive to other important process parameters such as the H_2O/CH_3CH_2OH ratio [65]. Therefore, except for intrinsic catalyst activity and process temperature, S_{CH4} cannot be effectively tuned by manipulating other degrees of freedom.
The lower concentration of CO with respect to CH_4 could be explained by the higher activity toward CO_x methanation, favored at low temperature, or by the enhanced WGS reaction, due to the exothermicity of both routes. The non negligible hydrogen presence in the products suggests the last route as the most likely.

Characterization of spent samples - Qualitative and quantitative analyses were carried out on the used catalysts in order to better investigate the catalyst deactivation by coke formation or sintering. TPO is a useful technique to quantify coke amount [66]. During this temperature programmed analysis under oxidizing atmosphere, the carbon species are oxidized at different temperature in accordance with their nature. Usually amorphous carbon is oxidized at lower temperature (200-300°C) whereas carbon nanotubes and graphitic/ordered carbon at higher temperature (400-600°C) [66]. In general, graphite is the most stable phase at low temperatures, while over 400°C, the MWCNTs are the main constituents of the C deposits, as extensively reported in the literature for Co and Ni-based catalysts [18,59]. Nevertheless, amorphous carbon, the less thermodynamically stable species [67], is the one most frequently found on a practical level, because the pathways leading to its formation are much faster. TPO profiles (Figure 1.10) ruled out the presence of amorphous carbon and confirmed the presence of carbon whiskers and ordered carbon.

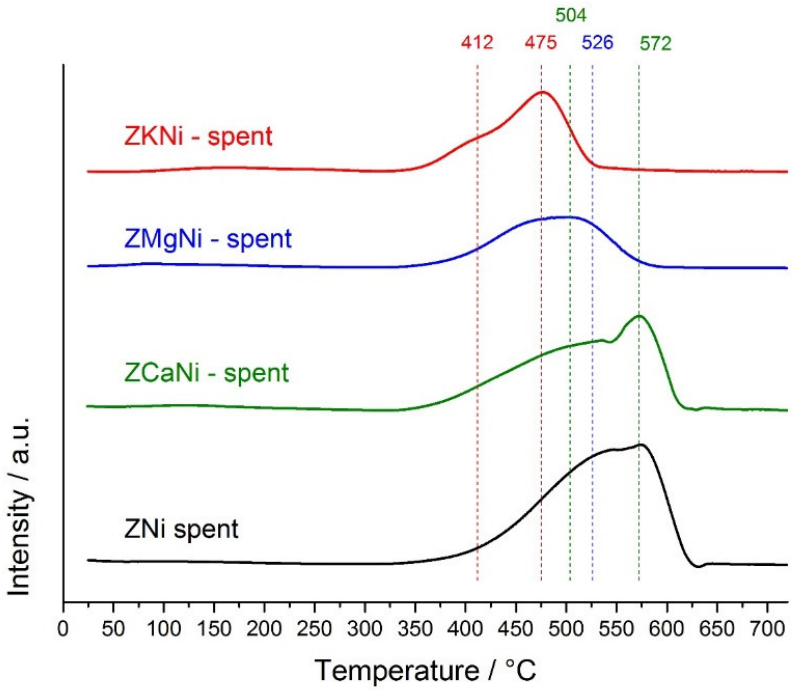

Figure 1.10. TPO profiles of the catalysts after the LT-ESR the full testing sequence at 500, 400 and 300 °C.

The absence of amorphous carbon was probably one of the main reasons to explain the lower deactivation here observed for K and Ca-doped samples with respect to other catalysts prepared by traditional techniques. Indeed ordered carbon, especially in the form of MWCNT, lead to a less evident deactivation because the tip of the metal particle can still remain accessible to the reactants due to the intrinsic mechanism of carbon formation [68]. By contrast, amorphous carbon is always encapsulating and in the presence of metal particles nearby the set up point, it can completely deactivate the active phase.

The discrimination between graphitic carbon in form of nanotubes or graphitic layers in the region between 400-600°C is very complex. TEM and SEM pictures revealed both graphitic and filamentous carbon for all the catalysts (Figure 1.11 and 1.12).

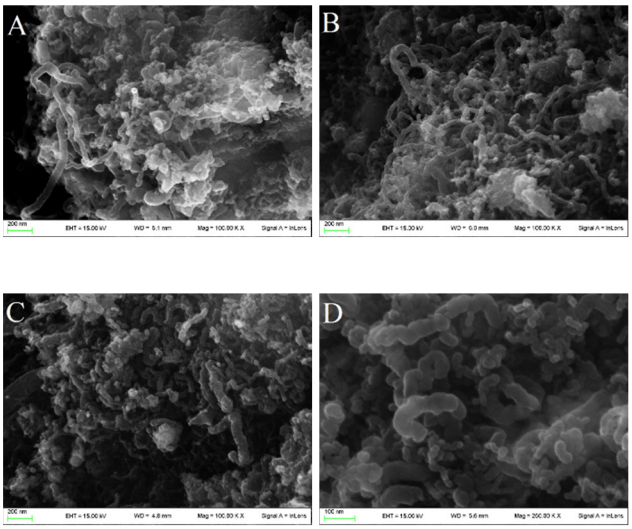

Figure 1.11. FE-SEM micrographs of catalysts after the LT-ESR tests: A) Zr-Ni; B) CaZr-Ni; C) MgZr-Ni; D) KZr-Ni. Marker size 200 nm for A), B), C), and 100 nm for D).

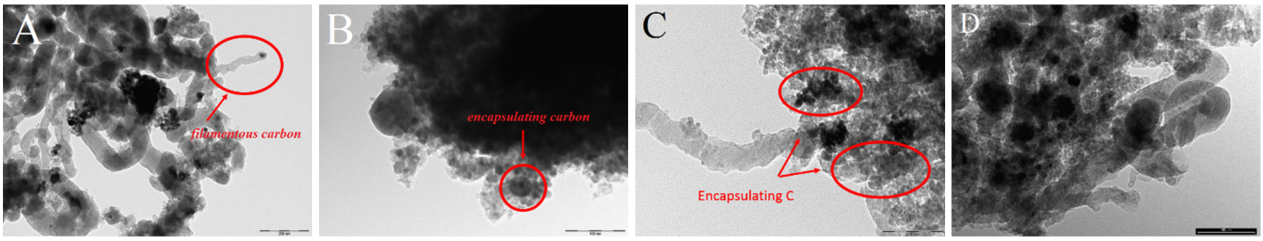

Figure 1.12. TEM micrographs of catalysts after the LT-ESR tests: A) Zr-Ni; B) CaZr-Ni; C) MgZr-Ni; D) KZr-Ni. Marker size 200 nm for A), 500 nm for C), and 100 nm for B) and D).

Deconvolution of the TPO profiles was also carried out to attempt an attribution to the different carbon species (Figure 1.13).

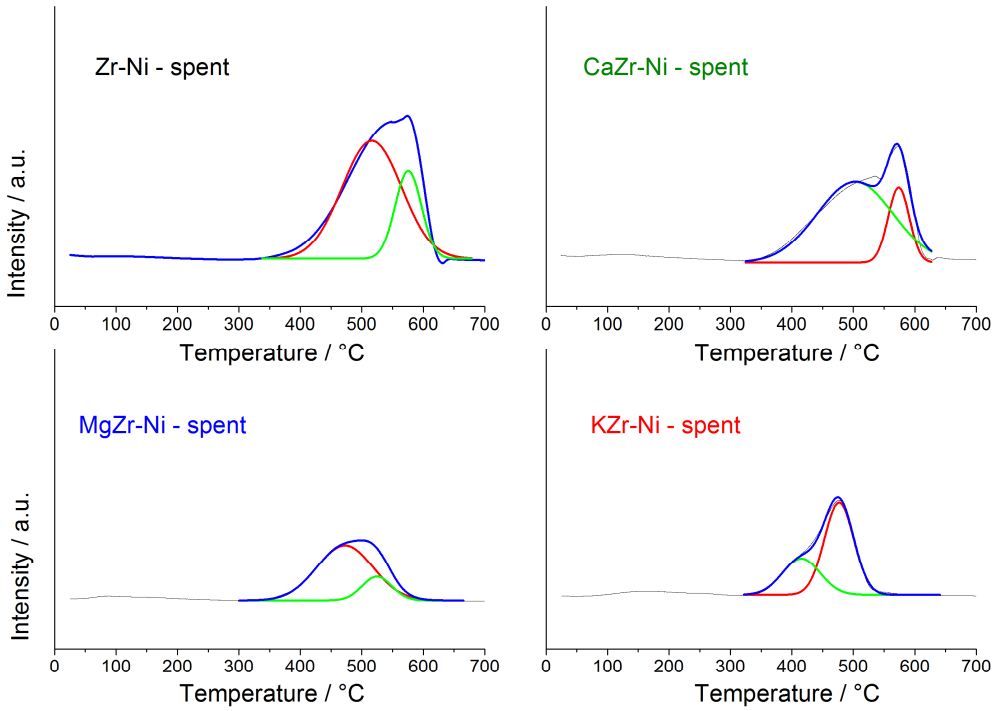

Figure 1.13. TPO profiles deconvolution of the catalysts after the LT-ESR testing.

All features were formed by the overlap of two peaks, but the position in terms of temperature changed slightly when varying the catalyst composition. As above mentioned, the higher is the order of the carbon species, the harsher is their oxidation [69]. However, the higher is the amount of carbon, the easier is the ability of the carbon to grow up in increasingly ordered structure. Raman spectroscopy (Figure 1.14) pointed out that no significant variation of the D/G bands ratio was detected. Such parameter is usually applied to discriminate between different ordered carbon species.

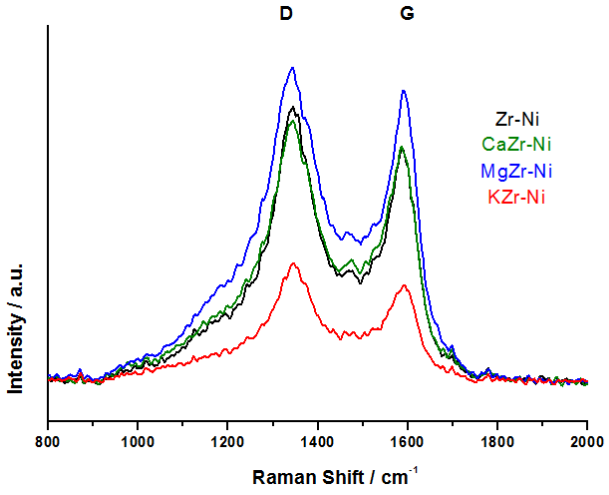

Figure 1.14 Raman spectra of the spent samples.

The D/G band intensity ratio here obtained between 1.1-1.3 confirmed the absence of amorphous carbon, because its presence usually leads to D/G intensity ratio higher than 1.8 [69].
The observed shift of the peaks in TPO analysis was therefore attributed to the different carbon amount rather than to significantly different species. The two peaks were attributed to the formation of non-filamentous coke at lower temperature, in particular in the C_β form, and filamentous coke at higher temperature [70]. The C_β form is produced by the rearrangement and polymerization of the C_α form, instead of crystalline phase formation by the dissolution of C_α in Ni particles and diffusion to the interface with the support with subsequent formation of carbon nanotubes. The C_β carbon polymer favours the encapsulation phenomena and leads to a complete de-activation of the Ni particles. For this reason Zr-Ni was less active at 400 and 300°C with respect CaZr-Ni and KZr-Ni, indeed it revealed a highest 1st peak in TPO analysis.

This explains also the higher activity of KZr-Ni with respect to CaZr-Ni, the former being characterised by an overall lower C deposition with respect to the Ca-doped sample. For MgZr-Ni the low amount of carbon formed was simply due to the lower activity of this catalyst, accumulated over the active phase, and not with the mechanism of carbon formation. The progressive deactivation revealed during the activity tests were attributed to the encapsulating carbon. This attribution was confirmed by the higher peak intensity of the 1st peak with respect the 2nd one in the TPO deconvolution and by TEM analysis.

To quantify the overall amount of C accumulated during the whole testing, TPO analysis was elaborated after calibration and the results are reported in Figure 1.15. In accordance with the C-balance of the activity tests, the lowest amount of carbon was detected for KZr-Ni and MgZr-Ni. As suggested in the Introduction, the strong metal-support interactions detected by TPR analysis confirmed to lead to the lowest carbon formation.

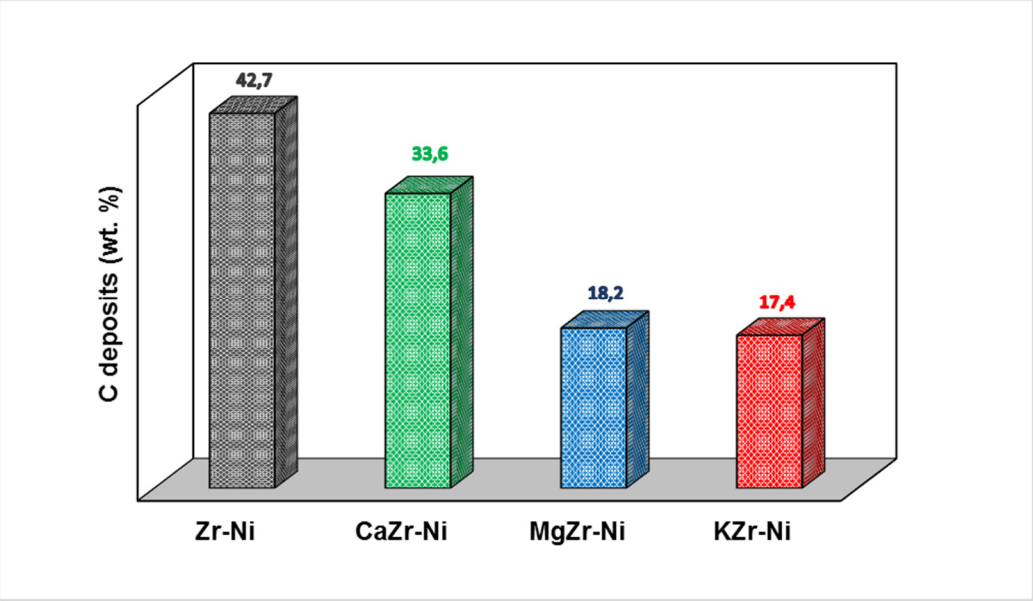

Figure 1.15. Coke accumulated over Ni-based catalysts used in the LT-ESR (temperature sequence: 500, 400, 300 °C) from TPO analysis.

Conclusion - The effect of alkali addition on the performance of Ni/ZrO_2 catalyst for the LT-ESR has been investigated. 500 °C is considered a sufficiently low temperature for this process, while 400 °C and 300 °C are often too critical as for insufficient activity and catalyst deactivation. Doped catalysts were prepared by Flame Spray Pyrolysis. Activity results showed that full ethanol conversion can be achieved even at 400 °C with the present catalysts, which thus proved very active for this application. The main differences were observed as for products distribution and resistance to coking. A strong decrease of CO/CO_2 ratio can be achieved by doping the Ni/ZrO_2 with Ca and K oxides. The results witnessed that K_2O was mainly a chemical or electronic promoter rather than textural promoter. The wider particle size distribution revealed a different agglomeration pathway within the flame during the synthesis. By contrast, the enhancement of activity at 500 °C and 400 °C, and the non negligible activity even at 300 °C, suggested K as one of the best chemical promoters for this process. Furthermore, alkaline promoters did not only affect surface acidity, but also Ni redox properties, crystalline phase and metal-support interactions.

1.2. Parametric study and kinetic testing

Understanding and unravelling ESR reaction mechanism, providing kinetic parameters, is fundamental for the scale up and process design of the technology. A simple Langmuir Hinshelwood kinetic model for a Ru-based catalyst was proposed by Vaidya et al. [71], considering the main reactions only to account for ethanol conversion and hydrogen yield, without details on intermediates formation and reforming. More detailed surface mechanism was proposed by Sahoo et al. [72] for a Co-based sample, accounting for ethanol decomposition to form methane, but methane steam reforming (MSR), acetaldehyde and ethylene formation/reforming were not considered. Mas and coworkers [73,74] focused on kinetics of supported Ni catalysts, including MSR, dry reforming of methane and surface reactions for ethanol decomposition. However, also in this they did not focus on acetaldehyde or ethylene which, as previously underlined, may be important byproducts.

Insights on the actual reaction mechanism and the formation of relevant intermediates and byproducts have been provided by theoretical, ab initio, DFT computations in addition to more traditional experimental works. Wang et al. [75] accounted for ethoxide formation followed by dehydration to ethylene on Ni, addressing the importance of C-H and O-H abstraction. A similar evolution of the adsorbed ethanol was confirmed by Christiansen et al. [76] in the framework of competitive ethylene and diethylether production. In both these works, a qualitative distinction was made between Ni, Rh, Co, Ir on one side and Au, Ag, Cu on the other. Similar studies on Pt by Sutton et al. [77], while giving different results for ethoxide stability, also established the importance of acetaldehyde as a key intermediate (by itself or via its direct dehydrogenation product CH_3-C=0). They reported similar activation barriers for C-C breaking and confirmed the importance of C-H cleavage as the likely rate determining steps.

It clearly appears that fundamental studies on the reaction mechanism firmly deal with the fate of C2 intermediates, which also exploit a great practical relevance as byproducts. However, kinetic studies usually do not provide experimental data on the evolution of these intermediates/byproducts as a function of experimental conditions. For this reason, this part of the PhD project was focused on a systematic kinetic investigation on one of the best performing catalysts tested in the previous section, *i.e.* 10 wt.% Ni/ZrO_2, promoted with 9 wt.% K_2O. Its performance was tested by varying operating temperature, space velocity (contact time) and water/ethanol molar ratio. Particularly stressing conditions were selected, so to limit ethanol conversion and favoring the formation of critical byproducts, such as ethylene, acetaldehyde and methane. The variables space was investigated according to a central composite experimental design. Besides producing a full set of experimental data for further kinetic modelling, the parametric dependence of catalyst performance on single and

multiple parameters has been addressed both qualitatively and quantitatively through statistical analysis.

1.2.1. Kinetic testing

All the experimental testing plan was conducted over the same catalyst batch by varying 3 parameters: temperature (T), gas hourly space velocity (GHSV) and the water/ethanol feeding ratio, according to the scheme in Table 1.3 and Figure 1.16.

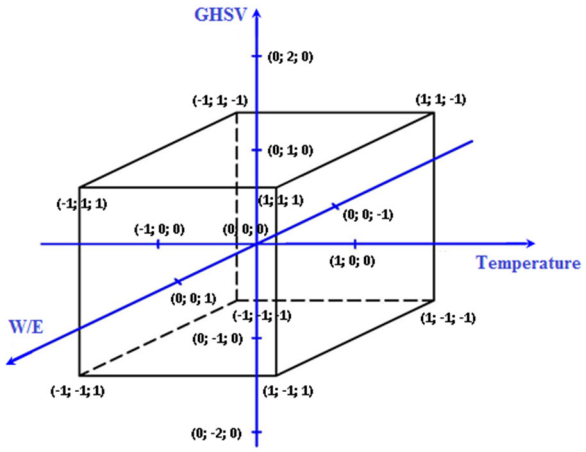

Figure 1.16. Scheme of the experimental testing plan

Table 1.3. Scheme of the kinetic testing experimental plan. W/E = water/ethanol ratio.

Code	*T (°C)*	*GHSV (h^{-1})*	*W/E (mol/mol)*	*Catalyst mass (mg)*
-2	550	25000	3.0	132
-1	575	50000	3.5	66
0	600	75000	4.0	44
+1	625	100000	4.5	33
+2	650	125000	5.0	26

At first, some explorative tests were carried out to identify the optimal conditions for the kinetic testing and to identify the central point of the plan. Testing was carried out at temperature higher than 550°C to avoid possible coking (especially at low water/ethanol ratio). The maximum catalyst amount was 132 mg in order to achieve sufficiently high GHSV according to the calibration range of the HPLC pump. The flow rate of liquid feed has been fixed at 0.038 mL/min. The dilution with SiC was done in different ratio in order to keep the same bed length for every test. The minimum dilution (higher catalyst amount) was selected in order to keep the cold spot controlled within 1.5 °C, whereas the maximum dilution was selected in order to avoid bypass effects [78]. The absence of external mass transfer limitations was checked by comparing two tests carried out at the same GHSV but

different catalyst amount. The effect of particle size on the catalyst effectiveness factor was also checked by comparing the results obtained with different particle size (0.05-0.125 mm). The results were equal within the experimental error.

After every change of experimental condition the system was equilibrated for 1 h. The tests were carried out according to the list in Table 1.3. Testing was performed on the same sample, except for the variation of GHSV, which was done by changing catalyst loading in the reactor. Repeated analyses were carried out to average the results. The central point (code 0/0/0, Table 1.3) was repeated randomly to check for repeatability.

1.2.2. Results and discussion of the kinetic investigation

The results were expressed in terms of ethanol conversion and selectivity to products. Hydrogen productivity is also reported, normalized per catalyst mass. The CO/CO_2 ratio was used as an indicator of the contribution of the WGS reaction. The variables were tuned in the selected operating range in order to limit ethanol conversion and to highlight the formation of interesting byproducts, to make hypotheses on the reaction mechanism. However, due to the very high activity of the selected sample, in order to operate in a coke free region (T>550°C), the GHSV was increased. This induced some experimental problems when operating at fixed catalyst amount. Indeed, at very high liquid feeding rate, especially at high W/E ratio, water condensation at reactor outlet was observed. In order to avoid this problem a fixed liquid flow rate was maintained, with the additional advantage of a constant fluid dynamic regime in the reactor. GHSV was therefore varied by loading different catalysts amount. No significant coke accumulation over the catalyst was observed in the selected temperature range and W/E ratio.

Effect of W/E ratio - The W/E feeding ratio was varied starting from the lowest boundary corresponding to the stoichiometric value. This parameter was not deeply investigated in literature although its role is crucial. Overstoichiometric mixtures are commonly used in demonstrative steam reforming units in order to push forward the WGS reaction by shifting the equilibrium conversion. Moreover, this enhances the coke gasification by water and consequently the catalyst stability. However, the higher is the W/E ratio the higher are the operating costs due to a less energy-efficient plant as a result of increased utility costs to vaporize the feed if internal energy recovery is not allowed.

Poorly concentrated bioethanol has been recently proposed as a less expensive feedstock for steam reforming [60,79]. Indeed, *ca.* 50 vol% ethanol can be obtained with relatively inexpensive purification strategies and may be conveniently used for this application without further purification. Experimental data showed that the increase of W/E ratio induced an increase of ethanol conversion. However, the conversion parameter is worthless without considering selectivity to by-products. Selectivity to C_2 byproducts decreased with the increasing of W/E ratio, suggesting the promotion of the reforming reaction for all the C_2 compounds. By contrast, a less remarkable effect was observed on methane selectivity, which was mainly affected by the other parameters. This point is very interesting and suggests that ethanol and acetaldehyde decomposition routes (eq. 3 and 5) are the main methane production paths rather than the methanation reactions starting from CO and CO_2 (eq. 4, reversed, and 8). This is reasonable being these reactions exothermic and not favored thermodynamically at temperature higher than 500°C, and is also in line with the findings of Wang et al. [80] about the prevalence of reforming over dehydrogenation at higher water ratios.

The CO/CO_2 ratio, decreasing with increasing the W/E feeding ratio, confirmed as expected the beneficial effect of this parameter on the WGS reaction. As a consequence of all these considerations, H_2 selectivity and productivity increased with W/E (Figure 1.17). Therefore, the use of diluted ethanol (high W/E ratios) is an effective way to enhance the hydrogen yield.

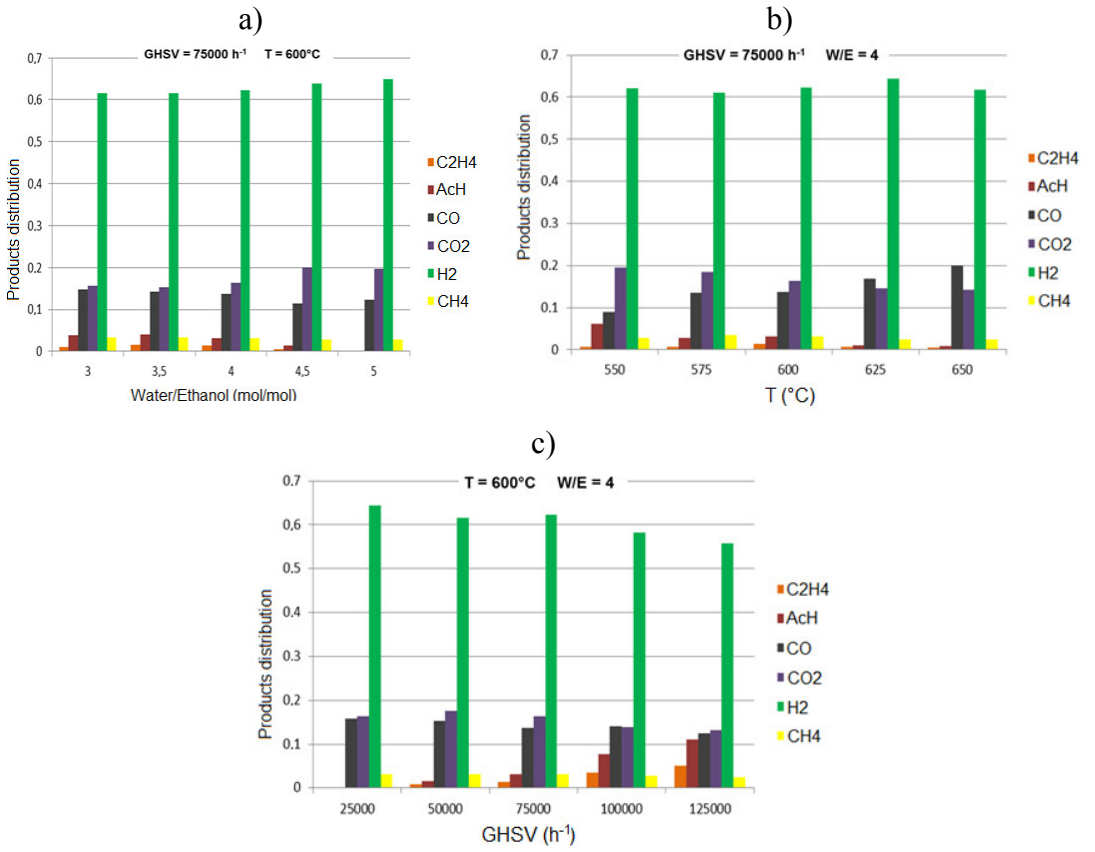

Figure 1.17. Products distribution as mole fraction vs. a) W/E ratio; b) temperature; c) GHSV.

Considering the possible pathways leading to the formation and conversion of all the byproducts, it can be observed that all the conversion paths for methane, ethylene and acetaldehyde can be favored by water addition, whereas only the formation of ethylene can be inhibited by the increase of water partial pressure, consistently with reaction 1.

$CH_3CH_2OH \rightarrow CH_2CH_2 + H_2O$ (1)
$CH_2CH_2 + 2H_2O \rightarrow 2CO + 3H_2$ (2)
$CH_3CH_2OH \rightarrow CO + H_2 + CH_4$ (3)
$CH_4 + H_2O \leftrightarrows CO + 3H_2$ (4)
$CH_3CH_2OH \rightarrow CH_3CHO + H_2$ (5)
$CH_3CHO \rightarrow CH_4 + CO$ (6)
$CH_3CHO + H_2O \rightarrow 2CO + 3H_2$ (7)
$CO_2 + 4H_2 \leftrightarrows CH_4 + 2H_2O$ (8)
$CO + H_2O \leftrightarrows CO_2 + H_2$ (9)

From a mechanistic point of view, the overall reforming process is based on a carbon-carbon splitting stage followed by the reversible processes (4)-(8) and water-gas shift (9). Moreover, the fact that the metal can activate C-C and C-H bonds, while –OH and –H transfers require the acid/basic sites of the supporting oxide, explains the coexistence of ethylene and acetaldehyde paths (selected by the support rather than by the metal) and the high conversion rates obtained with bare oxides [81], which are still able to dehydrogenate ethanol: the final state of the products depends then on the relative rate of C-C scission compared to that of the water-assisted CO and CH_4 reforming. Though it has been pointed out that high water fractions can decrease the *instantaneous* conversion rate due to competitive adsorption [82], this does not modify the *steady state balance* of the above reactions at sufficient catalyst loads.

Effect of reaction temperature - Temperature was changed from 550°C to 650°C. These conditions were milder with respect to those to be applied for the MSR (700-900°C) because of the easier reformation of an oxygenated substrate such as ethanol. The increase of temperature as expected induced an increase of ethanol conversion because of the endothermic nature of the reaction and for kinetic reasons. Also, the reforming reactions of ethylene and acetaldehyde were favored, but the MSR reaction was still insufficiently promoted, so that methane remained the primary H-containing by-product (Figure 1.17b). The exothermal WGS reaction was instead unflavored, leading to higher CO concentration with increasing temperature (Figure 1.18a). As a consequence, an increase of temperature led to decreasing selectivity to CO_2 and increasing to CO due to unfavorable WGS equilibrium. This would depress H_2 selectivity. However, increasing temperature favored the

conversion of the C_2 byproducts, which increased H_2 production. As a sum, the H_2 selectivity remained rather constant with increasing temperature due to the influence of these contradictory factors.

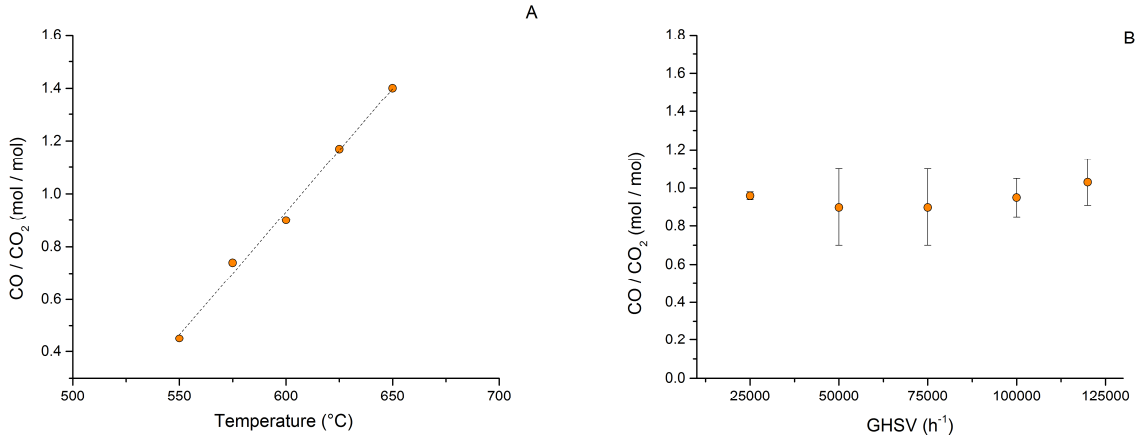

Figure 1.18. Trend of CO/CO_2 ratio considering: a) different temperatures at the same space velocity (GHSV = 75000 h^{-1}) and water/ethanol ratio (W/E = 4); b) different space velocity at the same temperature (T = 600°C) and water/ethanol ratio (W/E = 4).

Song and co-workers studied the temperature effect on the reaction network using temperature-programmed reaction and isotopic labelling techniques [83]. W/E ratio equal to 8 and GHSV of 5000 h^{-1} were used, obtaining similar product distribution trend using different catalysts (Co/ZrO_2 and Co/CeO_2). The significant discrepancy with this work was the presence of acetone, observed in a range between 450°C-550°C, considering moreover only the acetaldehyde as starting substrate with a water/acetaldehyde ratio equal to 10. This path was confirmed by the formation mechanism of acetone, which is mainly due to acetaldehyde condensation [84] or by reaction of acetaldehyde with adsorbed methyl groups [85].

A very straightforward combination of DFT, microkinetic modelling and experimental results has been reported [86], accounting for methane and acetaldehyde formation at low temperature on a Pt-based catalyst. In particular, the initial dehydrogenation of ethanol (α C-H abstraction) was found to be the rate determining step because of the much lower concentration of adsorbed ethanol relative to CH_x species. The explanation given for the positive effect of high temperature was related to the increase of efficiency of this dehydrogenation step instead of the OH-involving ones (water-gas shift and methane reforming were not taken into account), but the overall prediction was still in clear accordance with our results where the concentration of these compounds decrease drastically with increasing temperature.

Effect of GHSV - Correlation between reaction network and space velocity is a fundamental point for reactor sizing and for a clear explanation of the product profiles through the length of the reactor. As aforementioned, the change of GHSV was here accomplished by varying the catalyst mass. The increase of space velocity (decreasing contact time) lead as expected to a decrease of ethanol conversion, accompanied by less effective reforming of all the C_2 byproducts except methane. Consequently, H_2 productivity decreased of about 15% with respect to its highest value with increasing GHSV (Figure 1.17c), while a concomitant increase of acetaldehyde and ethylene selectivity was detected (up to 29% and 13%, respectively), witnessing the progressive lack of metallic sites referred to the ethanol mole fed. This aspect was confirmed by Frusteri et al. [87] by varying the GHSV (5000-40000 h^{-1} referred to the ethanol flow rate) on a Ni/CeO_2 catalyst.
Furthermore, the increase of selectivity to acetaldehyde and ethylene with increasing space velocity confirmed them as intermediates of a consecutive reaction network. Among the byproducts, methane showed a completely different behavior (its concentration remained roughly constant or even mildly increasing with increasing catalyst loading), and the prevailing role of reversible equilibrium reactions once ethanol and acetaldehyde were cracked was confirmed, together with the fact that the complete elimination of CH_4 and CO cannot just rely on a simple "conversion boost" however achieved.

The selectivity trend to CO and CO_2 is more complex: both concentrations decreased with increasing GHSV due to increased concentration of C_2 byproducts, from whose reforming CO and CO_2 are produced. Nevertheless, when looking at the CO/CO_2 ratio (Figure 1.18b) a substantially independent value with GHSV was achieved. This indicates that under the selected reaction conditions the WGS reaction reached a steady state condition. Thus, in order to promote WGS temperature should be decreased and W/E ratio increased, independently of the value of space velocity adopted. This point is crucial from a mechanistic point of view and not well argued in literature. Reaction quotients of WGS far from the equilibrium are often ascribed to a poor activity of nickel based materials, neglecting the role played by the oxide supports.

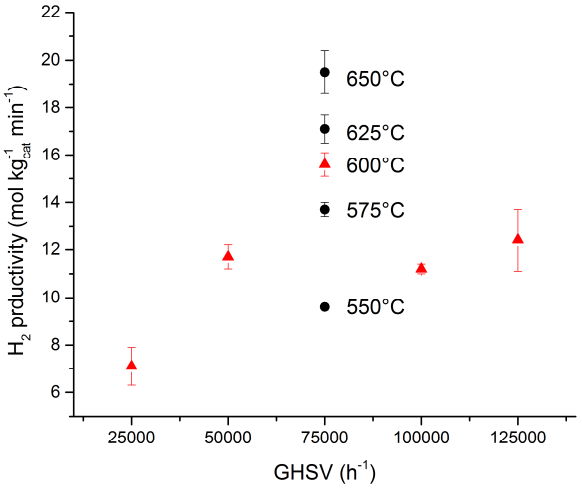

Figure 1.19. Parametric dependence of H_2 productivity from operating conditions at the same W/E (equal to 4). Red triangles refer to the same operating temperature (600°C), black dots refer to the same GHSV (75000 h^{-1}).

Overall comments and conclusion - The steam reforming reaction was confirmed to be the sum of different reaction pathways. The reaction was less demanding that the steam reforming of methane, with increasing ethanol conversion at increasing temperature, W/E ratio and contact time. Therefore, the use of diluted ethanol solutions seems favorable for this application. Full ethanol conversion can be easily reached over this catalyst under mild conditions and GHSV. Thus, to evidence the different intermediates and their dependence on the operating parameters, very high GHSV should be adopted. Ethanol can be dehydrated to ethylene, which is consequently reformed. The selectivity to ethylene was effectively decreased by raising the W/E ratio and lowering GHSV, while it showed less sensitive to an increase of the operating temperature.

Acetaldehyde was produced through dehydrogenation of ethanol and further reformed or decomposed to methane and CO. All the operating parameters deeply affected its selectivity, which decreased with increasing temperature, W/E ratio and contact time.

Methane selectivity remained rather limited (always well below 10%) and showed much lower dependence on the operating conditions. This byproduct can be effectively suppressed only by adopting much higher reaction temperature and longer contact time. Furthermore, its concentration decreased rather proportionally to the increase of acetaldehyde, suggesting that methane was predominantly formed from acetaldehyde decomposition (reaction 6). This is in accordance with the experimental results obtained by Karim et al. [65] using 10 wt.% Co/ZnO at 450°C and GHSV of 18000 h^{-1} although they attribute the methane formation to the direct ethanol decomposition (reaction 3). The data obtained in this chapter, show the presence of two consequent reforming processes

(ethanol followed by methane) and this can be explained considering: i) the relative stability of methane, ii) the kinetic relevance of the C-H breaking even respect to the C-C breaking and iii) the connection of different kinds of coke with both ethylene and methane [82]. The rather constant selectivity to CH_4 in the conditions adopted allowed to conclude that this compound is, as expected, harsher to convert in this temperature range.

Finally, in order to decrease the amount of CO in the products mixture, the WGS reaction should be promoted. This reaction was substantially independent from GHSV, and the CO/CO_2 ratio varied only with temperature and W/E ratio just in parallel with the relative variation of the reaction equilibrium constant. Therefore, it can be concluded that the reaction rapidly brings the reforming products in equilibrium conditions, although not simply defined by thermodynamic calculations on simple gas phase reactions.

Overall, the parametric dependence of H_2 productivity on the operating conditions is not trivially predictable, being based on different reactions. The H_2 productivity can be effectively enhanced by increasing contact time, temperature and W/E ratio. The latter aspect is practically very important, opening the way to the use of very diluted bioethanol mixtures, obtainable with rather inexpensive purification methods.

In this part of the PhD project, very stressing conditions for the catalyst were selected in order to highlight the formation of possibly critical byproducts, such as ethylene and acetaldehyde, which are not accounted for in most kinetic investigations found in the literature, obtaining a full dataset available for kinetic modelling.

1.3. Effect of substrate concentration (crude 2nd generation bio-ethanol)

Today, 1st generation bio-ethanol is the most available commercially, used as fuel and gasoline additive, mainly thanks to Brazil and USA. Nevertheless, 2nd generation bio-ethanol acquired increasing importance in the recent past [88]. A sustainable, scalable and simplified technology for the transformation of lignocellulosic feedstock into cost-effective, fermentable sugars for the production of bioethanol or biochemicals is nowadays available. The Mossi Ghisolfi Group (M&G) [89] developed a demonstrative plant for the fermentation of lignocellulosic materials in Crescentino, Italy, since June 2009 with a capacity of 40 kton/year of bioethanol. Generally, the biomass to ethanol technology is based on four main steps: pre-treatment, hydrolysis, fermentation and purification. The first three steps were constantly improved by research and development of new enzymes and fermentation conditions [90]. Although the plants are always designed with energy efficient processes, the last step of purification remains critical, because the main sector for commercialization of bioethanol is the fuel market, in which the composition of the substrate is crucial [8]. The purification line after the fermentation reactor is constituted mainly by distillation steps for the complete removal of impurities, especially water. Too high water content makes bioethanol unsuitable for blending with gasoline due to possible phase separation in the tank. Furthermore, a multistage separation based on vapor-liquid equilibria is required, due to the non ideal behavior of the water/ethanol mixture, which leads to the formation of an azeotrope. The anhydrification stages consume up to 50-80% of the total energy required for the whole production process [91], therefore the possibility to use directly bio-ethanol without purification looks very intriguing.

Steam Reforming processes as broadly explained in Chapter 1.1. Reactions involved are favored at high steam-to-carbon ratio due to the beneficial role of water in terms of coke gasification and hydrogen yield [8]. As a consequence, ESR owns a huge potential. However, although mainly composed of water and ethanol, bio-ethanol typically contains other oxygenated and sulphur-containing compounds [8], which represent a not negligible issue for the process. In this view, the acronym BESR (bio-ethanol steam reforming) is more appropriate for studies concerning real crude bio-ethanol [92], especially in the case of this work where differently purified solutions were used. The importance of impurities is not specifically addressed in the literature, since the scientific papers are mainly focused on ESR rather than BESR. This lack in the literature about the use of real crude bioethanol, especially the 2nd generation one, with the analysis of its contaminants with respect to sugar or starch derived ethanol [93], drove this part of the PhD project.

Organic and inorganic impurities play an essential role in the deactivation phenomena of the catalyst [94]. At low temperature deactivation by coking becomes relevant and several organic impurities, possibly present in raw bioethanol, have been reported to enhance the rate of carbon formation. For instance long chain alcohols, which are the main impurities in bio-ethanol obtained by fermentation of sugar cane [95], can more easy dehydrate leading to unsaturated molecules. The latter show higher tendency to polymerize over the acid sites of the catalyst [68]. In addition, the adsorption of higher alcohols may compete with the adsorption of water and ethanol and affect the hydrophilic surface properties [84].

The presence of organo-sulphur compounds, such as dimethyl-sulphide or dimethyl-sulphoxide, is another possible source of catalyst deactivation. The amount of sulphur impurities in the broth formed after the fermentation stage depends on the biomass used and the operating conditions adopted in the biological transformation process [93]. The poisoning role of sulphurs is well known for the industrial SR processes, especially when nickel is used as active phase. Indeed, the formation of bulk Ni_xS_y is critical [97]. For higher concentration of these contaminants, desulphurization of bioethanol is mandatory [96].

On the other hand inorganic anions (Cl^-, NO^{3-}, SO_4^{2-}) hardly deactivate the active phase by chemical interaction as in the case of sulphurs. Nevertheless their presence could be a problem because of their adsorption or reaction on the oxidic catalyst surface. This issue is shared in general with all the impurities able to adsorb on the surface, including carbonates, for the partial hindering of the active sites [98]. Chloride ions have an additional role because they may increase surface acidity of catalysts depending on the support used [99].

Le Valant and co-workers studied the effect of various impurities, such as long-chain alcohols, amines, ethers and organic acids [95,100]. They focused the attention on the main contaminants in 1st generation bio-ethanol obtained from sugar beet. The investigation was performed at high temperature (650°C). The work confirmed the key role of the contaminant concentrations.

In the present chapter the influence of bio-ethanol purity at high and low reaction temperature was studied considering catalyst formulations already tested for the ESR.
The use of crude 2nd generation bio-ethanol obtained mainly from Arundo Donax, a widely spread wild cane, growing on marginal lands, with minimum water input, integrated with wheat straw available locally, has never been explored up to now. The effect of substrate compositions in BESR was studied at different temperature. The study bio-ethanol purity over a broad region of operating conditions helps also to understand its contribution to catalyst deactivation. In absence of impurity, at higher temperature (>500°C) the deactivation of the Ni based catalyst is usually due to metal

sintering and solid state transformation. On the contrary at low temperature (<500°C) sintering is negligible with respect to the coke formation issues. Ni/La_2O_3, Ni/ZrO_2 and $Ni/CaO\text{-}ZrO_2$ catalysts prepared by flame pyrolysis were used for the investigation.

1.3.1. Catalyst Synthesis, activity tests, bioethanol composition

Catalyst Synthesis and activity tests - The preparation of Ni/ZrO_2 and $Ni/CaO\text{-}ZrO_2$ by flame pyrolysis was already discussed in Chapter 1.1. Preparation of Ni/La_2O_3 was carried out diluting lanthanum acetate and Nickel (II) acetate tetrahydrate in a mixture 1:1 (vol/vol) of o-xylene and propionic acid. The solution was fed to the burner using a 50 ml glass syringe with a flow rate of 2.2 ml/min and cofed with 5 l/min of O_2. The pressure drop across the nozzle was set to 0.7 bar for the sample supported on La_2O_3, to be used for testing at high temperature (750°C). Plant scheme and activity test procedure were the same reported in Chapter 1.1.

Crude bio-ethanol composition - Two samples of crude bio-ethanol investigated were kindly supplied by Mossi&Ghisolfi. In the fermentative reactor the biomass is mixed with enzymes and fermented, resulting in a broth with an ethanol concentration of approximately 8-10 vol% in the presence of residual carbohydrates. This broth is first roughly separated by a single stage distillation (flash) to obtain a bioethanol concentration ca. 50 vol%. Flash distillation is the simplest and cheapest method for the removing of these high boiling contaminants such as different sugars and higher alcohols [101]. Then, after several continuous rectification steps, pure ethanol is produced and commercialized for the fuel sector. A concentration stage to ca. 90 vol% bioethanol is followed by further anhydrification. The two different bio-ethanol solutions, i.e. 50 and 90 vol% were here tested as substrates for BESR, and labelled in the following as BE50 and BE90, respectively. The black broth before flash was not tested due to the suspended aggregates and high content of sugars. Poisoning effects are of course correlated with the poison concentration and nature in the feed steam, therefore knowing the analytical compositions is a practical necessary requirement. In addition lignocellulosic ethanol contains higher concentration and variety of impurities compared to sugar- or starch-derived bioethanol (almost two times higher) [93].

Composition analysis of the two samples here considered are listed in Table 1.4. The samples reveals common amount of oxygenated organic compounds combined with a progressive decrease of total acidity and conductivity passing from BE50 to BE90. A detailed discrimination of the single compounds was not possible due to experimental limitations, anyway acidity in this kind of bio-

ethanol is mainly due to acetic acid formed during the steam explosion step, in particular from the acetic groups present in the hemicellulosic fraction [102]. Oxygenated compounds are mainly alcohols such as propanol, isobutanol and various acetates [99]. The high conductivity values confirmed the presence of salts, mainly nitrates and phosphates [93]. The samples were here used as such, without any filtration or further treatment.

Table 1.4. Analytical composition of differently purified 2nd generation bio-ethanol solutions (certificate of analysis from quality control laboratory).

Parameters	***Unit***	***BE90***	***BE50***
Ethanol + alcohol saturated content	%(m/m)	89.7	50.2
Other oxygenated compounds	%(m/m)	-	0.15
Mono-alcohol saturated (C3-C5)	%(m/m)	0.37	-
Methanol	%(m/m)	0.27	0.1
Water	%(m/m)	9.66	49.6
Total Acidity	%(m/m)	0.0014	0.059
Conductivity	µS/m	159	2180
Optic Appearance	-	Clear and colorless	Opalescent
Inorganic Chlorides	mg/kg	0.14	0.1
Copper	mg/kg	0.02	0.02
Phosphorous	mg/l	0.02	0.02
Non-volatile materials	mg/100ml	1	5
Sulphates	mg/kg	0.86	1.0
Sulphurs	mg/kg	0.3	0.7

1.3.2. Activity tests: results and discussion

High Temperature activity tests - At first, high temperature reaction conditions (750 and 625°C) were explored. Generally these high operating temperatures (600-800°C) are chosen during the SR process in order to limit coke formation and promote the complete conversion of possible byproducts [8]. However, sintering became relevant and deactivation phenomena due to the sulphur impurities still remains. Generally the sulphur issue is eliminated by the hydrodesulphurization of the inlet gas stream before the reformer, whereas for sintering phenomena proper catalyst formulation has to be used.

Testing at high temperature brought to full conversion, no C_2 byproducts and limited or even nil methane selectivity irrespectively of the ethanol or bioethanol feed (Table 1.5). Systematically, slightly worse performance was achieved when decreasing the purity of the feed. However, stable and satisfactory performance was obtained at 750 and 625°C, selecting this latter value as preferable to decrease the heat input to the reformer in view of process intensification. Absence of CH_4 production at 750°C using pure ethanol (AE) witnessed a higher steam reforming activity without the

impurities. The present results demonstrate the possibility to exploit diluted bioethanol solutions, characterized by much lower production cost, in spite of their lower purity. Indeed, no significant deactivation or dramatically worse catalytic performance was observed. At 625 °C negligible selectivity to acetaldehyde and ethylene and low methane yield were achieved. 100% carbon balance was obtained at 750 °C and 625 °C thanks to the negligible formation of carbon deposits coupled with very efficient C gasification. Decreasing temperature led to a decrease of the CO/CO_2 ratio due to improvement of the WGS reaction. No dramatic change of these results was detected changing the bio-ethanol solution.

Table 1.5. Results of activity testing for BESR at high temperature using Ni/La_2O_3, 8 h-on-stream, data averaged out over 4-8 h, GHSV = 2700 h^{-1}, Water/Ethanol = 3 (mol/mol). AE = Absolute Ethanol.

Catalyst	***Ni/La_2O_3***								
Temperature (°C)	500			625			750		
Ethanol purity	AE	Bio90	Bio50	AE	Bio90	Bio50	AE	Bio90	Bio50
H_2 productivity (mol min^{-1} kg_{cat}^{-1})	1.18 ± 0.05	1.23 ± 0.12	0.46 ± 0.01	1.97 ± 0.05	1.30 ± 0.04	1.18 ± 0.07	2.05 ± 0.03	1.29 ± 0.06	1.08 ± 0.08
Sel. CH_2CH_2 (%)	0	0	0	0	0	0	0	0	0
Sel. CH_3CHO (%)	0	0	11.4 ± 1.4	0	0	0	0	0	0
Sel. CH_4 (%)	6.58 ± 0.04	12.6 ± 1.3	5.9 ± 0.6	2.2 ± 0.1	2.7 ± 0.3	2.8 ± 0.3	0	2.8 ± 0.3	2.5 ± 1.2
CO/CO_2	0.68 ± 0.01	1.0 ± 0.3	0.53 ± 0.02	1.7 ± 0.1	1.7 ± 0.2	1.4 ± 0.2	2.60 ± 0.12	2.3 ± 0.3	2.7 ± 0.3

Low Temperature activity tests - Ni/ZrO_2 and $Ni/CaO\text{-}ZrO_2$ were activated and tested at 500 °C. Low temperature SR tests was carried out in order to investigate how the impurities influence the process at critical conditions for coking formation. Moreover, these tests can help to check the contribution of sulphur and other compounds as poisons at low temperature.

Comparison between activity tests using pure ethanol (99.9 vol%) in the feed or BE90 is shown in Table 1.6. The steam-to-ethanol ratio of the feed was maintained equal to 3 (stoichiometric molar ratio) for all the tests, in order to operate under critical conditions for carbon formation, without changing this key parameter. In particular, the higher the amount of water in the feed, the higher H_2 productivity because of the thermodynamic promotion of the WGS reaction and the gasification rate of coke [8]. By contrast, drawbacks are the lower thermal efficiency of the process due to the higher evaporation enthalpy of more diluted liquid mixtures [60].

Table 1.6. Results of activity testing for BESR at low temperature using Ni/ZrO_2, 8 h-on-stream, Data Averaged out 4-8 h, GHSV = 2700 h-1, Water/Ethanol = 3 mol/mol. AE= absolute ethanol, 99.9 vol%.

Catalyst	***Ni/ZrO_2***			
Temperature (°C)	500		400	
Ethanol purity	AE	Bio90	AE	Bio90
H_2 productivity (mol min^{-1} kg_{cat}^{-1})	1.04±0.03	0.99±0.11	0.65±0.04	0.66±0.04
EtOH conversion (%)	100	100	100	100
Sel. CH_2CH_2 (%)	0	2±2	0	0
Sel. CH_3CHO (%)	0	0	0	0
Sel. CH_4 (%)	10.7±1.5	11.7±1.1	16±2	20±2
CO/CO_2	0.82±0.14	0.9±0.2	1.2±0.2	1.29±0.07

At 500°C a slight decrease of H_2 productivity and increase of methane selectivity was observed when using BE90 instead of absolute ethanol (99.9 vol%), which means that the few impurities have a marginal role at this conditions. The CO/CO_2 ratio slightly increased, showing a limited influence also on the WGS reaction. The same trend was obtained for the results at 400 °C, without significant variation. Traces of ethylene were sporadically detected when using BE90. Negligible ethanol conversions were attained at 300 °C for all the solutions used, whereas full ethanol conversion was reached at higher temperature.

However, in order to consolidate the possibility to operate at low temperature, $Ni/CaO\text{-}ZrO_2$ was used considering the better activity using pure ethanol (Chapter 1.1). In addition, different catalyst composition may induce a different response to poisoning agents in the feed.

Activity did not change appreciably when comparing BE90 and AE for catalyst $Ni/CaO\text{-}ZrO_2$ (Table 1.7): at 500 °C and 400 °C hydrogen productivity remained almost equal and only a small increase of methane selectivity was observed when using BE90. Full ethanol conversion was always obtained, whereas at 300 °C ethanol conversion decreased, combined with a suppression of methane and hydrogen formation. At 300 °C the main product was acetaldehyde, meaning insufficient activity for C-C bond cleavage.

Table 1.7. Results of activity testing for BESR at low temperature using Ni/CaO-ZrO_2, 8 h-on-stream, Data Averaged out 4-8 h, GHSV = 2700 h^{-1}, Water/Ethanol = 3 mol/mol. AE= absolute ethanol, 99.9 vol%.

Catalyst	***Ni/CaO-ZrO_2***								
Temperature (°C)	500			400			300°C		
Ethanol purity	AE	BE90	BE50	AE	BE90	BE50	AE	BE90	BE50
H_2 productivity (mol min^{-1} kg_{cat}^{-1})	1.07± 0.10	1.13± 0.07	1.08± 0.09	0.752± 0.006	0.80± 0.02	0.80± 0.04	0	0	0
EtOH Conv (%)	100	100	100	100	100	100	34±4	29±3	22.5±1.4
Sel. CH_2CH_2 (%)	0	0	0	0	0	0	0	0	0
Sel. CH_3CHO (%)	0	0	0	0	0	0	76±5	73±1	83±6
Sel. CH_4 (%)	19±2	20±3	16±2	37±3	34±3	26±2	10±2	11.2± 0.9	3±5
CO/CO_2	0.64±0. 10	0.65±0. 10	0.52±0. 10	0.20± 0.02	0.24± 0.04	0.42± 0.04	/	/	/

This catalyst revealed the most promising results, therefore BE50 was also tested. At 500 °C and 400 °C H_2 productivity was equal than that obtained with high purity feed and no decrease of catalytic activity was ever detected. The absence of acetaldehyde and the stable performance with time-on-stream suggested that no strong deactivation occurred due to the impurities contained in the feed. The slightly lower carbon balance can be attributed to higher carbon formation, due to the presence of longer chain alcohols. The CO/CO_2 ratio remained constant or even lower during the test at 500 °C, meaning that the impurities did not influence the degree of the WGS reaction. The values of C-balance relative to the tests using Ni/CaO-ZrO_2 are summarized in Figure 1.20 at different temperature.

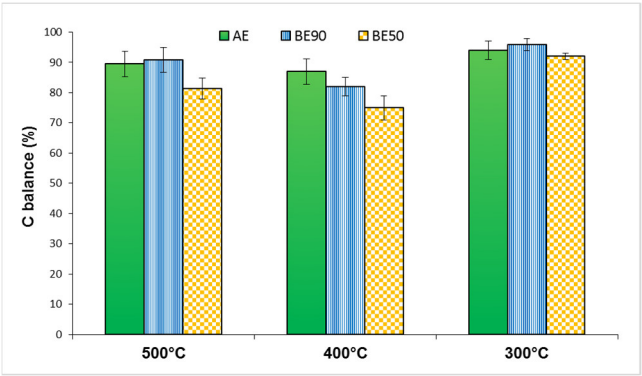

Figure 1.20. Carbon balance for Ni/CaO-ZrO_2, data averaged out on 4-8 h-on-stream, GHSV = 2700 h^{-1}, Water/Ethanol = 3 (mol/mol). Reference for C balance in a blank test (without catalyst) at 500°C: 91 ± 4.

The C-balance, used as indicator for coke accumulation over the sample, was comparable with that of the blank test (i.e. without catalyst) at every temperature. Slightly lower C balance was systematically achieved with BE50 with respect to purer feeds, indicating possibly higher coking rate over the sample. The increase of carbon formation could be ascribable mainly to the inorganic and

organic contaminants. The contribution of inorganic compounds may be related to sulphur containing species, partially deactivating Ni. However, a decreasing catalyst performance with time-on-stream would be expected in such a case and this can be ruled out (Figure 1.21) [103].

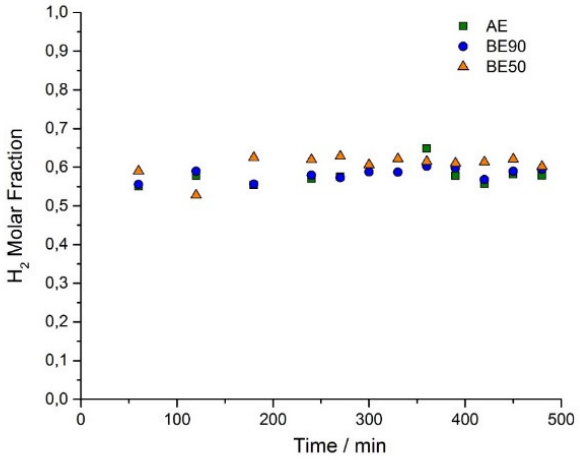

Figure 1.21. H_2 molar fraction at 400°C for sample Ni/CaO-ZrO_2 with different feed.

Another reason can be the deposition of salts on the catalyst. However, feed evaporation occurs in the initial hot part of the reactor, which is filled with inert quartz beads, excluding significant fouling of the catalyst. Therefore, volatile organic contaminants, in particular organic acids and higher alcohols are expected to be responsible of this slightly higher carbon formation. In general coking phenomena are due to three main routes: i) hydrocarbons decomposition; ii) Boudouard reaction; iii) olefins formation and polymerization [8]. However, at low temperature (≤500 °C) the former route is unlikely from a thermodynamic point of view [104]. The oligomerization of olefins generated by substrate dehydration (ethylene in the case of ethanol), is well known process, and occurs over the acidic sites of the support [26]. The presence of higher organic alcohols and oxygenated compounds increase the coke formation because of the easier dehydration and polymerization of the higher homologues, thus this route has been considered the predominant here. Therefore, by considering the stable behavior with time-on-stream and the absence of C_2 byproducts (often appearing when Ni is progressively covered by encapsulating carbon) exclude significant Ni deactivation. Therefore, the slightly higher coking contribution observed with BE50 can be mainly ascribed to the residual acidic sites over support surface.

The comparison between catalytic activity of Ni/ZrO_2 and Ni/CaO-ZrO_2 revealed a different behaviour toward the water gas shift reaction. This point is critical for Ni-based catalyst, which are less active toward this reaction with respect other metals like Fe, Cu and Co [84]. The decrease of temperature from 500°C to 400°C led to lower activity for this reaction for the undoped sample, as

witnessed by the increase of CO/CO_2 ratio. The opposite behavior was achieved for the CaO-doped sample. The same behavior was obtained using both bio-ethanol solutions, therefore a different mechanism characterized the two catalysts. The explanation of the lower performance of Ni/ZrO_2 for WGS was detailed in Chapter 1.1. Using $Ni/CaO\text{-}ZrO_2$ the WGS reaction was enhanced decreasing the temperature to 400 °C due to its exothermicity. However, a slight increase of the CO/CO_2 ratio was observed using feeds with decreasing purity (from 0.20 to 0.24 and 0.42, Table 1.7). This behavior can be better studied looking the time-on-stream results in Figure 1.21, where a progressive increase of CO formation is combined with a decrease of CO_2 and CH_4 concentration. We can tentatively explain this behavior considering that the higher concentration of higher alcohols when passing from AE to BE90 to BE50 can lead to slightly higher carbon deposition over support surface, especially at the lowest temperature, for which the coke gasification activity is more limited. This effect is not correlated to a decrease of catalytic activity of the Ni particles, which remain substantially unaltered. However, the support plays its own role by activating steam and supplying activated oxidising species to the C-based intermediates which are forming on the Ni particles. If the surface of the support changes its composition, support activity in activating water and surface mobility of activated oxydrils change, leading to unsteady products distribution with time-on-stream. Looking specifically to Figure 1.22, a further consideration can arise. The rate of disappearance of CH_4 and CO_2 is the same and corresponds to roughly half that of formation of CO. This can be correlated to a dry reforming reaction ($CO_2 + CH_4 \rightarrow 2\ CO + 2\ H_2$) occurring over the catalyst at low temperature. Likely, the reverse Boudouard reaction can also contribute to CO formation at expenses of CO_2. Thus, in general we may conclude that at low temperature CO_2 can partly act as oxidising agent, activated on the same Ni particle, if sufficient oxidising species are not transported through the support surface.

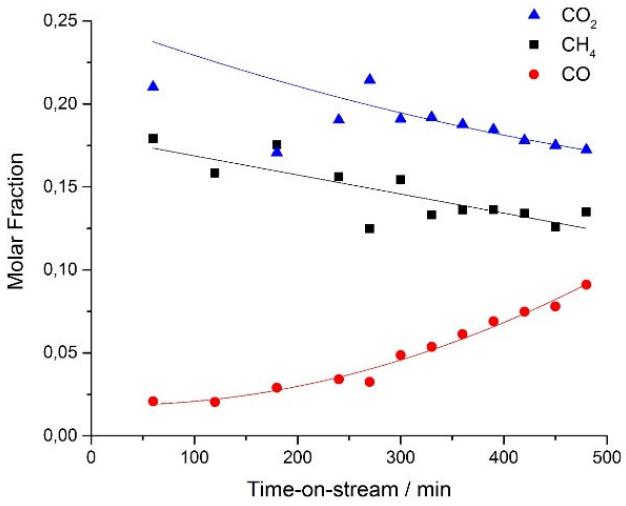

Figure 1.22. Product distribution vs. time-on-stream for BE50 tests using $Ni/CaO\text{-}ZrO_2$, GHSV = 2700 h^{-1}, Steam/Ethanol = 3 mol/mol, T = 400 °C.

Comparison between different supports - A comparison between the two different support (La_2O_3 and $CaO\text{-}ZrO_2$) was carried out at 500 °C. Results at 500 °C using Ni/La_2O_3 were largely unsatisfactory. This result was not unexpected. Indeed, lantana was found more suitable for higher operating temperature, as reported in previous investigations [23]. $Ni/CaO\text{-}ZrO_2$ samples proved more effective at lower temperature (Figure 1.23), although some criticisms may arise due to coking issues, which are instead not significant when using a basic support at high temperature.

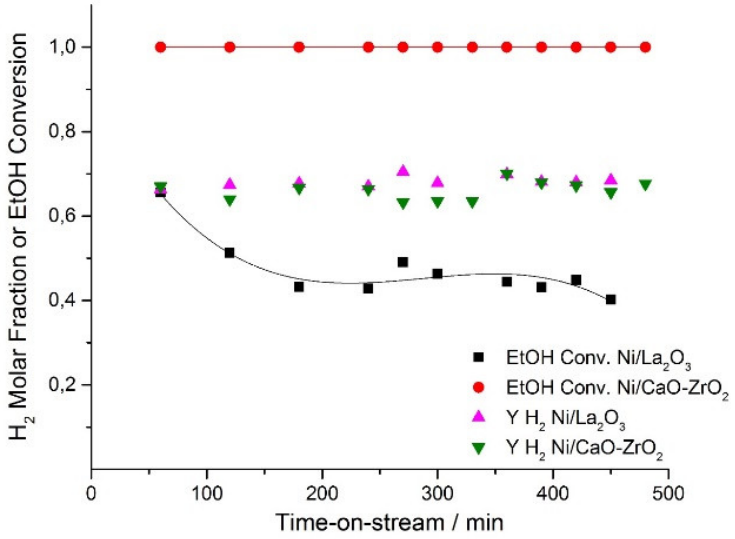

Figure 1.23. Comparison of H_2 molar fraction and ethanol conversion using BE50 for bio-ethanol SR tests using $Ni/CaO\text{-}ZrO_2$ and Ni/La_2O_3 at 500°C.

The better results at lower temperature of zirconia based sample with respect to Ni/La_2O_3 confirmed the best behavior toward coking of these materials.

1.4. Reformer-PEMFC energy generator ($5kW_e + 5kW_t$): demonstrative project

Being H_2 mostly produced from fossil sources, it is more expensive than traditional fuels, and therefore its use in internal combustion engines is often economically unfeasible. However, the introduction of a specific market for fuel cells has witnessed a growth of interest as energy vector. In this context, the use of renewable resources for the production of H_2 should be carefully analyzed to assess not only its environmental sustainability through life-cycle analysis (LCA), but also its economical feasibility.

In this perspective, a device for the co-generation of thermal and electric energy was installed c/o the Dept. of Chemistry of Università degli Studi di Milano, on the basis of a collaboration with Helbio S.A. Hydrogen and Energy Production Systems (supplier of the unit) and some sponsors (Linea Energia S.p.A., Parco Tecnologico Padano and Provincia di Lodi). This device is composed of a semicommercial GH2-BE-5000 unit connected to a polymer electrolyte membrane fuel-cell (PEM). This system is designed to produce energy for civilian de-localized uses or for small industrial applications. GH2-BE-500 unit layout is shown in Figure 1.24.

Figure 1.24. GH2-BE-5000 unit installed c/o the Dept. of Chemistry of Università degli Studi di Milano, for heat and power cogeneration.

The PEMFC connected was a prototype in a semi-commercial stage, operating at low temperature (80 °C). Although requiring short start-up periods, resulting adapt also for emergency devices, CO poisoning of the Pt-based electrodes is a serious drawback when H_2 is derived from organic feed-stocks. The fuel processor here adopted is designed to decrease CO concentration below 20 ppm in the reformate. The scale of the process is 5kW electric and 5kW thermal power as peak output. The

goal of the testing campaign was to demonstrate the feasibility of this technology and to propose improvements.

1.4.1. GH2-BE-500 unit

The GH2-BE-500 unit consists of a series of six reactors connected in series, as show in Figure 1.25.

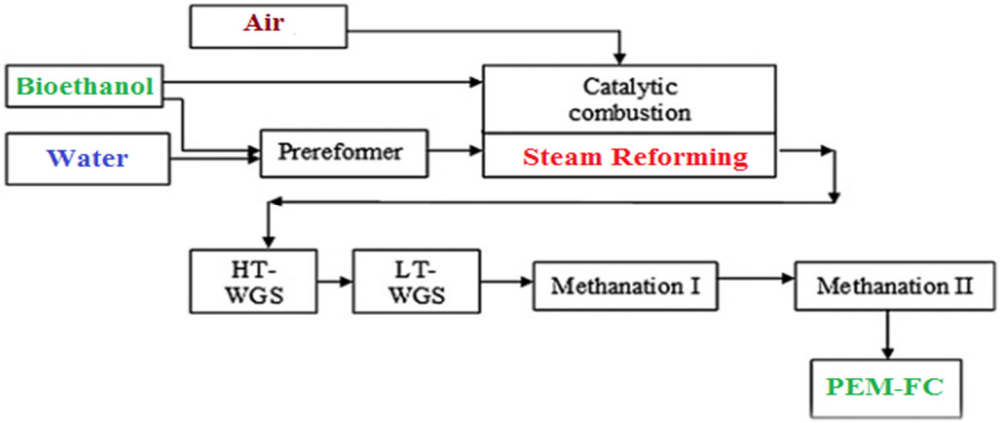

Figure 1.25. Schematic flowsheet of the fuel processor.

Bioethanol from grapes (Alcoplus, 99.0 vol%) was diluted to 96.0 vol% with deionized water before feeding the unit. Ethanol with 96 vol% concentration was not directly purchased from the supplier due to purity reasons. The alcohol was fed to a heat exchange reactor (shell and tubes) containing both the steam reforming and commercial combustions catalysts. After evaporation in an electrically drive heater, ethanol was mixed with air for feeding the combustion side (shell) and with water vapor to feed the hydrogen production line (tubes). The latter reacting mixture was first fed to a pre-reformer, then to the main reforming reactor. Two reactors for water gas shift and two for methanation downstream are connected in series to the reformer to purify the reformate gases from CO. Heat exchange with air blowers is provided between each of them to progressively lower the reaction temperature. Excess water is condensed at the outlet of the last reactor by cooling at ca. 80 °C. A pressure relief valve allows to set the reformate discharge pressure depending on the FC requirement. A gas sampling point is available after each reactor. Products analysis were carried out by means of an Agilent 7890 GC equipped with TCD detector, PoraplotQ and Molecular Sieves columns. The analytical method allows the quantification of ethanol, water, H_2, CO, CO_2 and CH_4, acetaldehyde, ethylene, ethane and acetic acid. Reactor heating is accomplished by combustion of part of the ethanol over a commercial combustion catalyst, which is hosted in the tube side. The water/ethanol ratio in this case has been set to ca. 5.5 mol/mol, to prevent extensive coking and to

drive the WGS equilibrium towards CO removal. Pressure at the outlet of the processor has been at first adjusted to 0.8 barg. An example of gas composition after each reactor is reported in Figure 1.26.

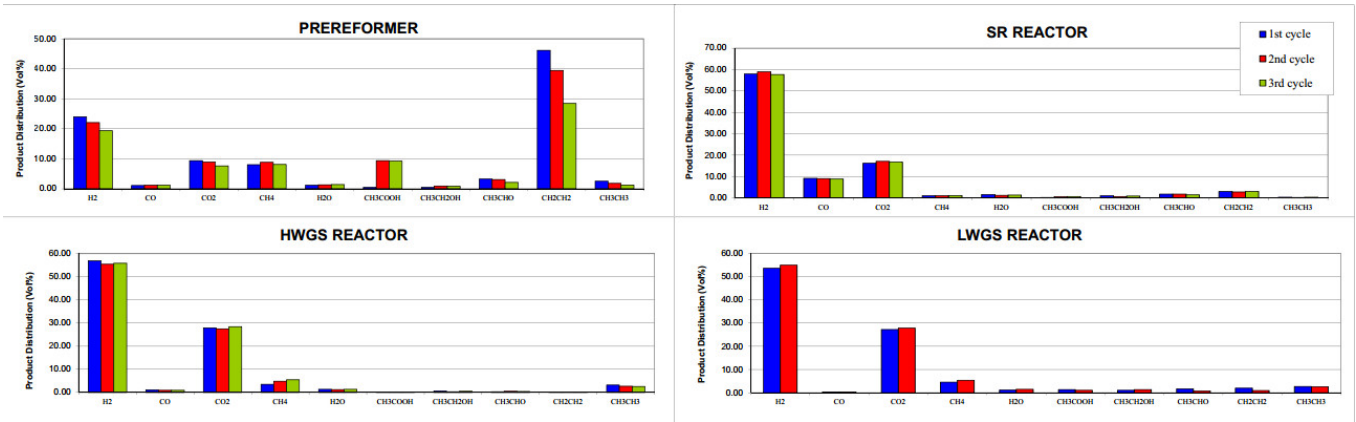

Figure 1.26. Products distribution (vol%) for every reactor. No significant trace of other by-products was detected. CO concentration lower than 0.04 vol% after the LWGS stage.

H_2 concentration was ca. 20% after the first pre-reforming stage. The prereformer was the unit more instable considering the variation of the product distribution for very cycle, although this fact didn't influence the performance of the next steps. After the reforming reactor, almost all CH_4 was converted. However, the CO/CO_2 ratio increased due to the thermodynamically unfavorable conditions for the WGS reaction.

Hydrogen purification was first accomplished by water gas shift (WGS), divided in two reactors, one at high-temperature (HT) and one at low temperature (LT). The former is operated around 350 °C for kinetic reasons and it converts ca. 90% of CO, the remaining portion being abated in a LTWGS stage at 280 °C to shift the equilibrium towards ca. 0.3-1% CO.

Several tests were performed, but unfortunately the technology was not enough robust in our perspective. The unforeseen byproducts detected after the last methanation reactor before the fuel cell, such as ethane, methane and acetaldehyde followed by ethanol not completely converted (5%), was not expected. The start-up period of the fuel processor for the catalyst activation and the achievement of the operating conditions, was too long (almost 2h), making it suitable for stationary, steady state, continuous operation only. The maximum power generated by the fuel cell was 2.1 kWel for 4 hours, far from the nominal output of 5 kW_{el}. The experimental results showed that the reformate quality is suitable to feed low-temperature PEMFC, but if a high temperature fuel cell stack is used, a much more compact and simpler layout may be foreseen, avoiding the methanation steps.

1.5. Techno-economic analysis of a bioethanol to hydrogen centralized plant

Although many scientific articles were published on BESR process for hydrogen and syngas production, only few studies on the cost-benefit analysis can be found in the open literature, which represents a limit to attract investments. The operating pressure of BESR represents a first critical factor. The steam reforming reaction leads to an increase in the total number of moles; therefore, the higher is the pressure the lower is the advancement of the reaction at equilibrium (Le Chatelier principle). However, industrial natural gas steam reforming units conventionally operate at relatively high pressure (15-30 bar), because they supply hydrogen or syngas to ammonia, methanol, hydroformilation, Fischer-Tropsch synthesis, and it is more convenient to operate the steam reformer at a higher pressure than compressing the resulting syngas. Higher reformer pressure decreases the capital costs due to smaller reformer size and to limits the compression costs needed to meet the specifications of the downstream processes [106]. Also, when the process aims at centralized hydrogen production as fuel, the end user will need tank refill at high pressure, so that operating BESR at high pressure is advantageous. Thus, in this project a high-pressure reactor was designed, at difference with most literature on the topic.

Another critical point is the choice of the fuel for the furnace that supplies the energy to the reformer. In traditional MSR the fuel is natural gas itself. Different options can be available for BESR, since bioethanol or part of the produced hydrogen/reformate can be used as fuels as well [59].
Several research groups investigated hydrogen combustion. Gallucci et al. studied the application of a dual fluidized-bed membrane reactor for hydrogen production via autothermal reforming of methane [108]. Part of the ultrapure hydrogen produced was sent to a burner to supply the energy required. Unfortunately, no economic assessment was proposed by the authors in order to establish the profitability of such a choice. On the other hand, also the use of ethanol as fuel is feasible from the technical point of view [109]. The latter two approaches allow to avoid the carbon tax, because burning carbon-neutral bioethanol or green-hydrogen is considered neutral from the point of view of CO_2 emissions. Nevertheless, the economic assessment of renewable hydrogen production units is insufficiently addressed in the literature. Indeed, even if some papers propose scale up and technical assessment of H_2 production units from renewables [108,111], solely one paper was focused on a techno-economic analysis of the simulated process [113] and none of them is related to the use of 2nd generation bioethanol. For instance, Oakley et al. technically discussed the feasibility BESR, but no economic analysis or process optimization were reported [114].

Therefore, the aim of this PhD project section was the techno-economic evaluation of a large scale BESR plant for the production of pure hydrogen. The latter is intended for whichever use as fuel or chemical. This step is a milestone to assess the feasibility of hydrogen production from bio-ethanol on a large scale, targeting the petroleum industry customers and large producers of bioethanol in the world.

This part of the PhD project was carried out at the Chemical and Petroleum Engineering Department of the University of Calgary (Canada) under the supervision of Professor Nader Mahinpey and Dr. Ehsan Mostafavi (from January/2017 to April/2017).

1.5.1. Process Design and modelling

The feasibility of power cogeneration through fuel cells using bioethanol was studied for distributed energy generation as reported in the previous Chapter. In other papers of our group [59,60], the process efficiency and the use of diluted bioethanol feeds were evaluated, considering different process configurations. However, the size of the fuel processor studied was suitable for a small-scale hydrogen production (6.5 Nm^3/h), needing proper upscaling in the present case where centralized production is the goal. The same process layout was used, except that the fuel cells are not included here because not available commercially for large power output. The big scale power generation using a gas-turbine or other types of fuel cells were not considered here in order to avoid limitations and *vincula* in the economic assessment. Indeed, the use of sustainable hydrogen for other chemical processes can be also an intriguing alternative, such as hydro-treating processes.

The fuel processor here proposed is constituted by a BESR, a HT-WGS, a LT-WGS and a Methanator. Although in the literature CO-purification reactors are commonly simulated as Gibbs or equilibrium reactors, in this work we simulated them as fixed bed reactors, by selecting and implementing kinetic expressions based on commercial catalysts, whereas for the BESR reactor a home developed kinetic model was used, relying on a proprietary catalyst. This allows the correct sizing of each reactor and, consequently, appropriate costing.

The scheme of the process is sketched in Figure 1.26. The feed for the steam reforming line is considered as a parallel alternative to the production of ethanol 99.5 Vol.% (fuel grade, in gray in the Figure).

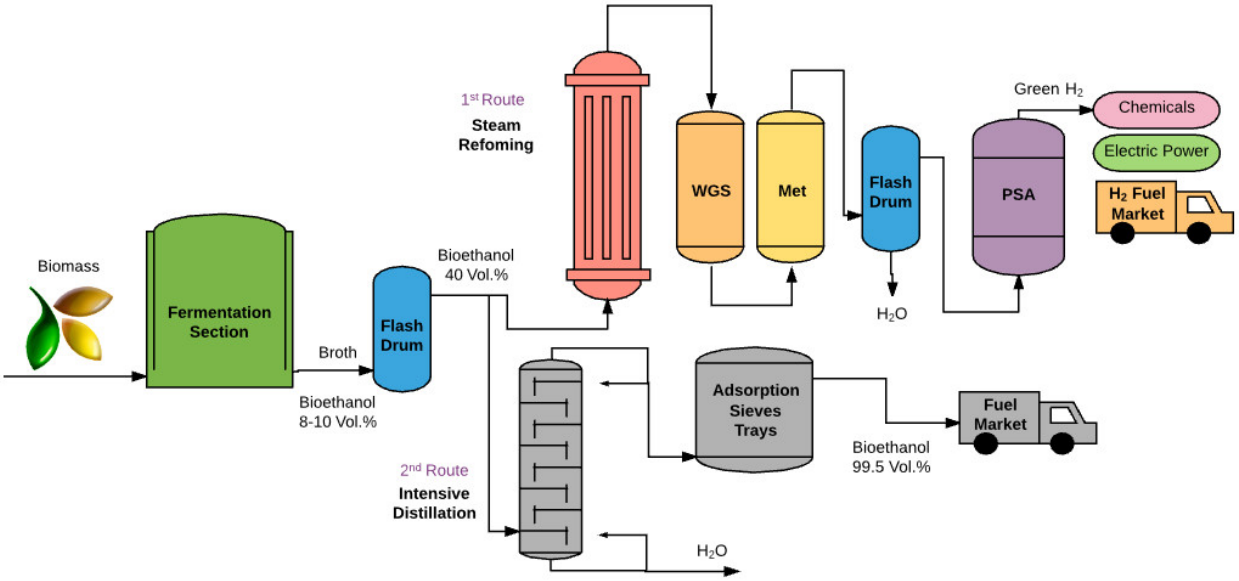

Figure 1.26. Scheme of two parallel routes to exploit bioethanol produced by fermentation. 1st route: centralized hydrogen production; 2nd route: production of 99.5 Vol.% ethanol for the liquid fuel market. WGS = Water Gas Shift; Met = Methanation; PSA = Pressure Swing Adsorption.

The process was assessed using the AspenONE Engineering Suite® (v. 8.6), in particular the flowsheet has been designed and optimized using the Aspen Plus® process simulator, whereas the economic analysis was carried out using the Aspen Process Economic Analysis module. The chemical process design was performed using the traditional hierarchical method (onion model) [115]. The reactor was the starting point of the design, followed sequentially by the separation and purification units. The kinetic expression for the steam reforming reaction was implemented considering previous papers of our group [59]. For the HT-WGS step the kinetics proposed by Hla et al. [116] was selected. The power-law reaction rate expression was proposed for a commercial $Fe_2O_3/Cr_2O_3/CuO$ catalyst.

Table 1.8. Kinetic expressions implemented in the Fixed Bed reactors.

Process	*Reaction*	*Kinetic model type*	*Ref.*
Steam Reforming	$CH_3CH_2OH \rightarrow CH_4 + CO + H_2$ $CH_3CH_2OH + H_2O \rightarrow CO_2 + CH_4 + 2H_2$ $CH_4 + H_2O \leftrightarrows CO + 3H_2$ $CO + H_2O \leftrightarrows CO_2 + H_2$	LHHW	[59,60]
HT-WGS	$CO + H_2O \leftrightarrows CO_2 + H_2$	Power-law	[116]
LT-WGS	$CO + H_2O \leftrightarrows CO_2 + H_2$	Power-law	[117]
Methanation	$CO + 3H_2 \leftrightarrows CH_4 + H_2O$	LHHW	[118]

The catalytic Fixed Bed reactor for the LT-WGS step was simulated selecting the work of Choi et al. [117]. A Commercial $Cu/ZnO/Al_2O_3$ catalyst was employed and, also in this case, the authors applied a power-law reaction rate expression. For the CO methanator, the article of Zhang et al. [119] reported

the use of a commercial Ni/Al_2O_3 catalyst, following a Langmuir-Hinshelwood-Hougen-Watson kinetic expression (LHHW). The reactions considered, model adopted and references are summarised in Table 1.8. The parameters to calculate the equilibrium constants were obtained following Bartholomew and Farrauto [120].

The experimental steam reformer was configured as a shell and tubes heat-exchanger, where the steam reforming catalyst was located in the tube side and a commercial combustion catalyst in the shell side. The reactor was sized based on the industrial terrace wall steam reforming reactor [121], using particle catalyst for the fixed bed. The sizing parameters are reported in Table 1.9. For the main steam reforming unit the particle size and pressure drop were simulated in detail considering the shape factor (0.58), Sauter particle diameter (12.5 mm) and an overdesign factor of 20%. The same number of tubes and length/internal diameter ratio of the experimental configuration use in Chapter 1.4 [122]. Particle shape was simulated as a single-channel cylinder (ring shape). The pressure profile along the catalyst bed has been calculated according to the Ergun equation. The water gas shift reactors and methanator were simulated considering their typical commercial features [123,124], in adiabatic configuration which is the more acceptable for industrial applications compared to the isothermal one [120]. A scale-up ratio of 1800 based on the ethanol stream was used assuming a capacity of 40,000 ton/y of bioethanol. This productivity has been chosen based on a commercial examples of second generation bioethanol production plant currently commercialized by the Biochemtex group [125]. The vaporized feed was simulated by feeding high pressure liquid ethanol and water mixture into a vaporizer.

Table 1.9. Design parameters of the reactors.

Parameter	*SR*	*HT-WGS*	*LT-WGS*	*MET*
Catalyst	Ni/Al_2O_3	$Fe_2O_3/Cr_2O_3/CuO$	$Cu/ZnO/Al_2O_3$	Ni/Al_2O_3
GHSV (h^{-1})	7,700	10,600	6,800	3,900
Mass of catalyst (kg)	4,078	3,197	4,984	5,406
Particle density (kg/m^3)	2,356	1,630	1,630	1,014
L/D	43	2.8	1.4	2.0
Number of tubes	109	1	1	1

Usually, hydrogen production by steam reforming of ethanol is experimentally investigated at pressures below 10 bar [85,124]. However, the implementation for large scale production must be explored in the pressure range at which steam reforming of natural gas for syngas generation is economically viable, which is higher than 10 bar [114]. Thus, a pressure of 20 bar was here chosen in order to match the balance between compression cost, equipment volume and thermodynamic conversion. In addition, further increasing pressure can lead to inconsistent results based on low

pressure kinetics. Thermal gradient through the catalytic bed was simulated as for the experimental unit.

The water/ethanol ratio was optimized in another work of Professor Ilenia Rossetti [122], and for this work an optimal steam-to-ethanol ratio equal to 5 was selected (40 wt.% Ethanol, 60 wt.% Water). This composition is easily achievable either by partially purifying the bioethanol raw beer by flash or by using a feed split approach as extensively described in Chapter 1.3. Finally, the present results were compared with those reported by Oakley et al., who simulated the process on an industrial scale, but without implementing kinetic expressions [114].

The flowsheet is reported in Figure 1.26. Heaters and coolers were simulated by setting the utilities and surface area reported in Table 1.10.

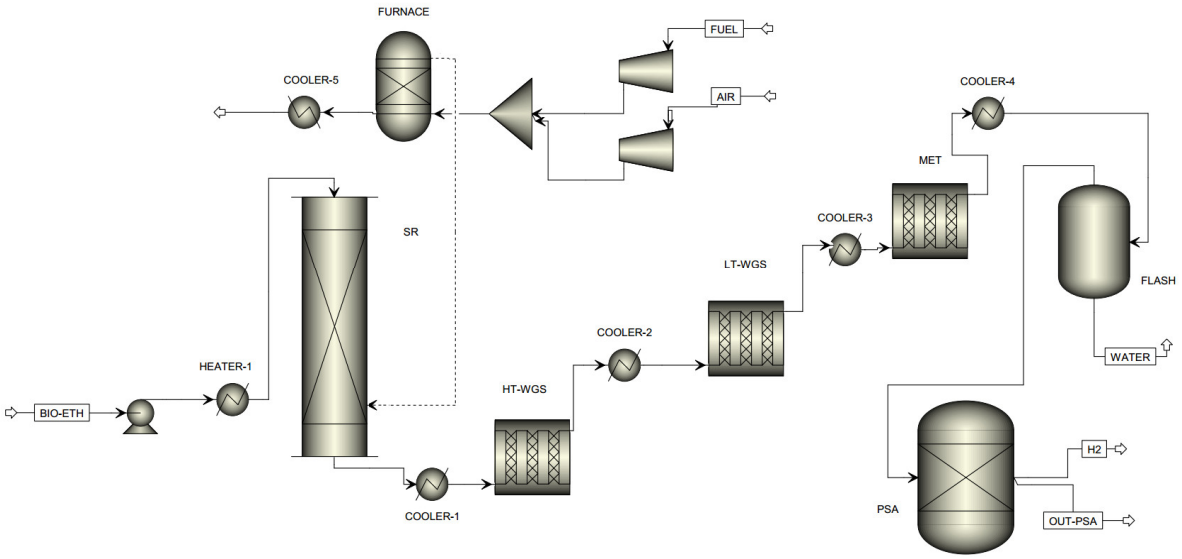

Figure 1.26. Bioethanol-to-hydrogen process flowsheet.

Table 1.10. Specifications of heat exchangers used for process before heat-integration (base case).

Item	Heater-1	Cooler-1	Cooler-2	Cooler-3	Cooler-4	Cooler-5
Utility	Fired Heater	High Pressure Steam Generation	Cooling Water	Cooling Water	Cooling Water	Cooling Water
Heat Duty (MW)	12.89	-4.54	-1.35	-0.82	-4.88	-5.96
Area (m^2)	1533.0	46.6	72.6	9.4	66.3	21.0

The furnace coupled to the steam reformer, was simulated in Aspen Plus® using a Gibbs reactor. The mass flowrates of air and fuel where adjusted so to generate the heat duty needed by the reactor with

an air flowrate leading to 2% excess oxygen with respect to the stoichiometric [128]. A firebox reformer heater (rectangular shape) without catalyst was selected for the economic evaluation, with walls externally lined by refractory material.

The compressors for air and fuel were simulated in accordance with the Gas Processors Suppliers Association (GPSA) standards. The reciprocating configuration coupled with gas engine was chosen. The pumps were simulated using centrifugal configuration.

The Pressure Swing Adsorption (PSA) unit was simulated in accordance with a traditional H_2 recovery unit typically used for refinery off-gas streams [129]. This reference work was chosen based on the similar pressure range (20 bar) and temperature (35°C), although a higher steam molar flow was used in our case. The amount of zeolite was scaled up accordingly. The four units of PSA were considered operating in parallel as detailed by Mivechian et al. [129]. The storage tanks and other offsite equipment were not included in the assessment. The plant flowsheet was established based on experiments in a 13.9 kg/d pilot plant, including purification steps of WGS and methanation, but without a PSA unit.

The heat integration was implemented using the Aspen Energy Analyzer® tool using the pinch analysis methodology. This technique analyses all the thermal flows within the process boundaries, identifying the most economical ways to maximize the heat recovery and minimize the demand for external utilities. Heat exchangers were sized calculating the heat exchange surface area using conventional industrial considerations in order to properly choose the location of the fluids (shell or tube side) and the other critical parameters such as fouling, phase change, erosion and corrosion. The flowsheet after the heat integration is detailed in Figure 1.27, whereas the specifications of the heat exchangers used for process is shown in Table 1.11.

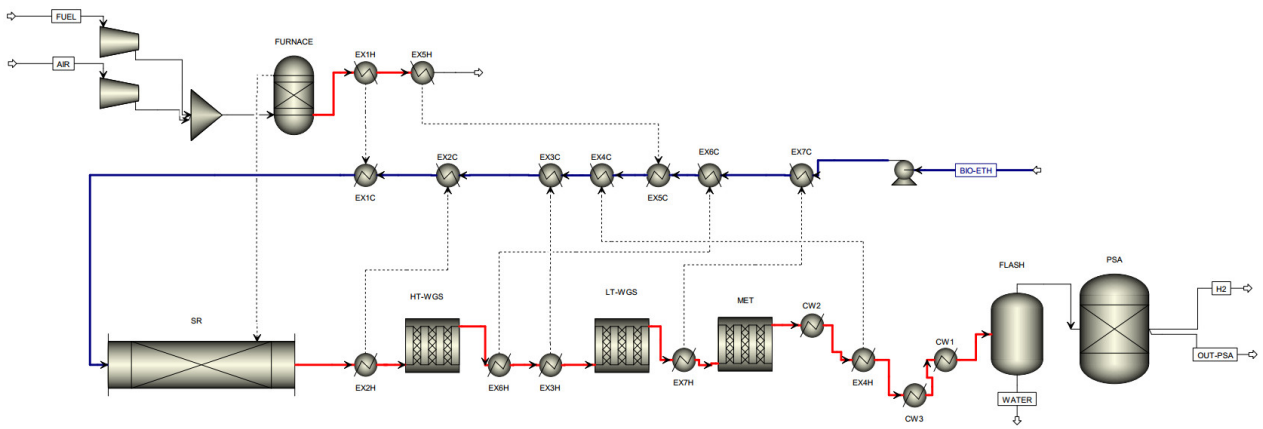

Figure 1.27. Hydrogen production from bioethanol steam reforming flowsheet after heat integration (C and H after a given label identify the cold or hot side of the heat-exchanger)

Table 1.11. Specifications of heat exchangers after pinch analysis and thermal integration

Heat-Exchanger	*EX1*	*EX2*	*EX3*	*EX4*	*EX5*	*EX6*	*EX7*	*CW1*	*CW2*	*CW3*
Area (m^2)	24.0	4.6	481.8	165.0	36.8	92.9	1511.7	28.4	11.5	3.4
Shells	1	1	2	2	1	1	5	2	1	1
Heat Duty (MW)	0.82	0.16	0.92	1.06	1.19	4.55	3.77	1.99	1.72	0.11

1.5.2. Economic Performance Analysis

The simulated process flowsheet was used to estimate the Total Capital Investment (TCI) and the OPerating EXpenditures (OPEX) of the hydrogen production and purification sections. Different scenarios and price sensitivity analyses were defined to highlight the dependence of CAPEX and OPEX on different economic parameters. The economic assumptions are listed in Table 1.12. A rate of return of 10 was chosen as profitability factor. A 30 year plant life was assumed, based on similar steam reforming technologies [113,130]. The working capital was assumed as 15% of the TCI as conventionally used for traditional chemical plants [115]. The salvage value was evaluated as a fraction of the initial capital cost. The straight-line method was adopted as depreciation method (the difference between the salvage value and the initial capital was divided by the economic life of the project, so that the project depreciates evenly through all its economic life).

For both the product and the raw materials we considered the same escalation value (= 5), as reasonable because these compounds pertain to the commodity market. The stream factor was set to 96% (8406 operating hours per year).

Table 1.12. Investment Parameters.

Parameter	*Unit of measure*	*Value*
Corporate tax rate	%	30
Interest rate / Desired rate of return	%	10
Economic life of the project	year	30
Salvage Value (fraction of initial capital cost)	%	20
Capital escalation (e)	%	2
Products escalation	%	5
Raw Materials escalation	%	5
Operating and maintenance labor escalation	%	3
Utilities escalation	%	3
Working Capital (WC)	%	15
Start-up period	week	20
G&A expenses	%	8
Operating hours per year	hour	8406

The choice of raw materials costs, utility cost and product selling price is always a critical point for the economic evaluation of a project, because it heavily influences the outputs of the analysis. This point is a minor issue when the scope is the internal comparison of different scenarios under the same assumptions. On the contrary, it is important for the comparison with literature data or with existing plants. The price of bioethanol was estimated considering a commercial selling price of pure bioethanol [125] diminished by 50% due to savings in the purification by flash or feed split with respect to the azeotropic distillation [59,79,122]. Indeed, the purification of bioethanol can affect up to 50-80 % its production price, at least for the first generation biofuel [79,91].
The ASME Boiler & Pressure Vessel Code (BPVC) were chosen as the standard for the design of pressure vessels. Feedstock, utility and product costs are summarized in Table 1.13.
Catalysts were considered in CAPEX and not in OPEX because the reactors considered to have fixed bed configuration, therefore there is no need of continuous make up of fresh catalyst to the reactor. Catalyst deactivation issues were also computed and mainly ascribed to sintering and coking, with lower impact of the latter because of the high temperature of reaction [126]. Planned shutdowns of the plant were predicted for regeneration.

Table 1.13. Feedstock, utility and product costs.

Parameter	***Unit***	***Price***
Bioethanol (40 wt.%)	USD/kg	0.211
Methane	USD/m^3	0.177
Water	USD/kg	0.118
Electricity	USD/kWh	0.0775
Hydrogen	USD/kg	2.69

The investment calculation criteria and methodology were evaluated considering conventional economic indexes. The following equations have been used for calculations:

$$NPV = \sum_{k=1}^{n} \frac{CF}{(1+i)^n}$$

NPV = Net Present Value, where *n* is the project lifetime (or economic life of the project), CF is the annual cash flow and *i* is the interest rate (also called desired rate of return or return on investment, ROI). The IRR (Internal Rate of Return) was then evaluated as the interest rate at which the present value in the last year of the project is zero, obtained by solving the following implicit equation.

$$NPV = \sum_{k=1}^{n} \frac{CF}{(1+IRR)^n} = 0$$

The total capital cost (C_T) was evaluated using the Aspen Process Energy Analyzer (APEA) library at the system cost base date, adjusted to the present date using the capital escalation values reported in Table 1.12, according to the following equation.

$$C_{AT} = C_T * \left(1 + t_D * \left(\frac{e}{100}\right)\right)$$

C_{AT} = Adjusted Total Capital cost; t_D = Time difference between system cost base date and start date for engineering; e = Project capital escalation. The project capital escalation was chosen considering the chemical engineering plant cost indices during the last years.

The economic analysis was carried out at first considering a fixed H_2 selling price and a fixed ROI. The operating costs were evaluated including the following items: raw materials, G&A expenses (general and administrative costs), operating labor costs, plant overheads, charges during production for services (facilities, payroll overhead, etc.), utilities, maintenance.

The starting date for the calculation of operating costs was the day after the end of the Engineering-Procurement-Construction (EPC) phase. The starting date for the calculation of product sales was the day after the end of the EPC + start-up phases. The final cash flow at the end of plant life was calculated based on the salvage value and the working capital in addition to the total earnings. Aspen Process Economic Analyzer was used to identify a window of economic viability of the process considered. This tool enables to focus the engineering process on business priorities, integrating business considerations and sophisticated engineering analysis. All the results were checked, re-evaluated and compared with the literature [115] and industrial case histories.

1.5.3. Results and Discussion of the economic analysis

Economic analysis of different scenarios - A first economic assessment was carried out using methane as fuel for the furnace and excluding any heat-integration (base case). Figure 1.28 shows the CAPEX evaluation for this scenario, considering the capital fraction relative to the equipment. The highest issues is related to the heater for the vaporization of the feed, followed by the compressors and the steam reforming units (coupled tubes and furnace). OPEX are shown in the same Figure 1.28 and evidence that bio-ethanol, even if diluted and less expensive than the azeotrope, still represents the major cost, followed by methane (fuel for the furnace). The flowrate of pure hydrogen at the outlet of PSA is 889 kg h^{-1}. This value was obtained by feeding 4567 kg h^{-1} (40,000 ton $year^{-1}$) of ethanol.

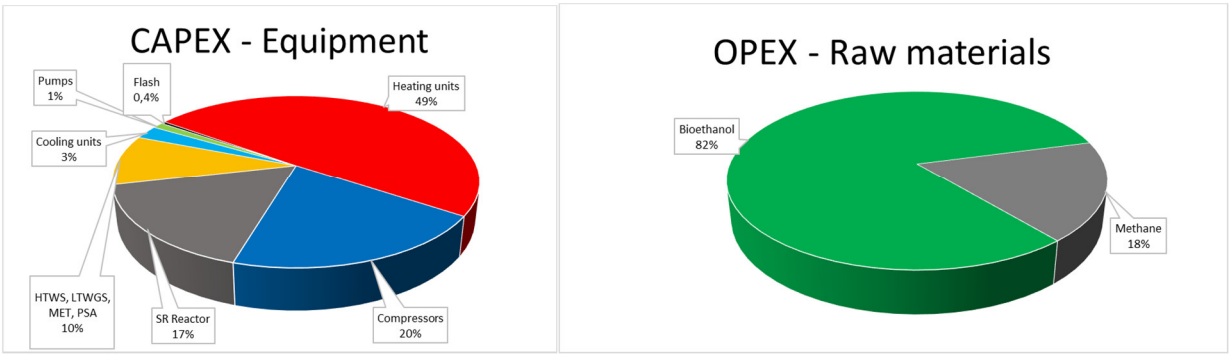

Figure 1.28. Equipment purchase costs as base for capital expenditure calculation (left) and Operating (right) costs summary relative to raw materials and utilities, for the bioethanol steam reforming process without heat-integration using methane as fuel for the furnace. Utilities not shown are negligible.

Three different scenarios (A, B, C) where then compared: the base case relies on methane as fuel for the furnace (case A), while pure ethanol (case B) and a portion of the produced hydrogen-rich stream (case C) were considered as alternatives. The comparison of total CAPEX (considering working capital, direct costs and equipment costs) and total OPEX (considering raw materials, operating labor costs, utilities, G&A expenses) for the three scenarios is reported in Figure 1.29.

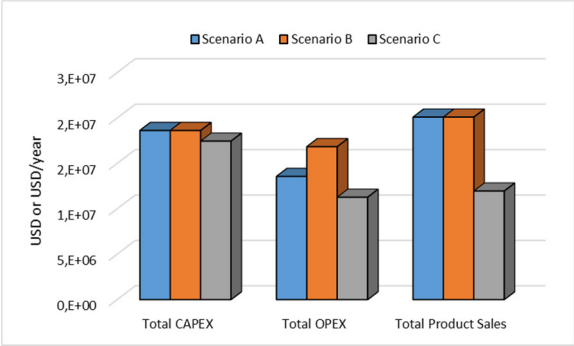

Figure 1.29. Comparison of CAPEX and OPEX for the different scenarios. Values of CAPEX are reported as USD while OPEX and product sales as USD/year

Capital costs were slightly lower in the scenario C because no compressor was needed for the already pressurized hydrogen when used as fuel. By contrast, OPEX assume different values for every scenario. Scenario B has the highest OPEX, because the furnace is fed with pure ethanol (azeotrope), which is assumed as much more expensive than the diluted bioethanol used as feed. However, the use of the diluted bioethanol to feed the burner is precluded by its insufficient heating value. On the other hand, the lowest value for OPEX is achieved for the scenario C, because no additional fuel is

used. However, it considerably shortens product sales (i.e. part of the product is internally used for heating) and, thus, total plant revenues.

The Internal Rate of Return (IRR) measures efficiently how the capital is being used, although it gives no indication on the profits. In this comparison, the IRR is 24.9%, 14.9% and 0% for the scenarios A, B and C, respectively. The possibility to use part of the hydrogen produced as fuel for the thermal supply of the endothermal process was investigated in a thermodynamic study by Giunta et al. [111]. However, the null value of IRR here obtained means that the investment is not profitable on a large industrial scale to get revenues. Nevertheless, scenario C may keep its interest on a small scale for independent residential cogeneration, where the exploitation of other fuels may be excluded for different reasons. Additionally, scenario B was less remunerative than A, due to the higher price of ethanol than methane and higher energy needed to vaporize of the fuel. Moreover, in this case complications arise with furnace optimization when using ethanol instead of the very well assessed methane-based technology.

Thermal integration of the process - The energy integration of the best scenario (A) was performed, at first by categorizing the hot and cold streams and then making a pinch analysis to design the heat exchangers network. A first, rather conventional solution for heat integration is to thermally couple the reactor feed and product stream. A preheater train of heat exchangers was then designed, taking advantage of the fact that the whole separation unit operations operates in decreasing cascade temperature with respect to the reactor. The pinch point was found and several scenarios of integration were compared. The heat exchanger network was then designed accordingly.
The optimal integration scenario in terms of both minimum exchanger cost and utility consumption was implemented in the final simulation. Nevertheless, this part of the utilities design can be further optimized case by case considering the context of the site, with possibly coexisting processes that can be connected to a common utility system. After the heat integration, the new partition of CAPEX is reported in Figure 1.30. The comparison of CAPEX and OPEX before and after heat integration is reported as well.

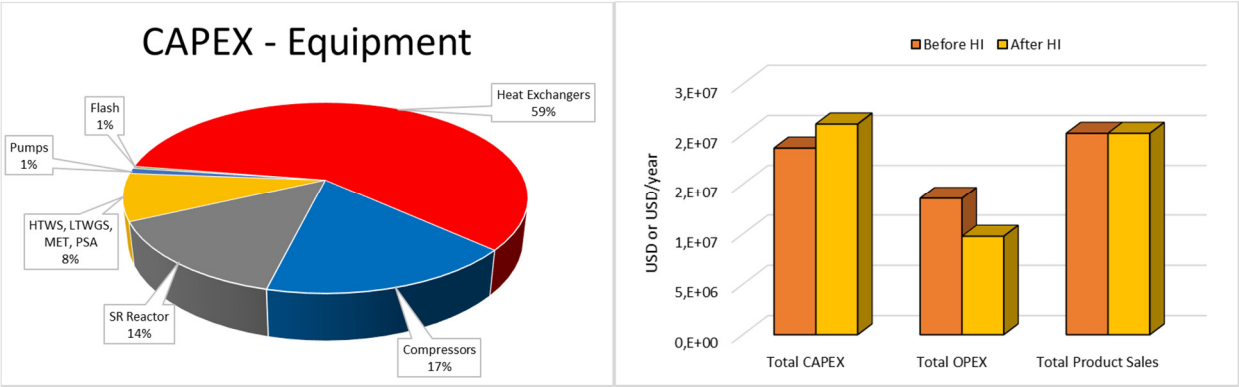

Figure 1.30. Left image: Capital cost summary for the bioethanol steam reforming process after heat-integration using methane as fuel for the furnace. Right image: Comparison of CAPEX and OPEX for the scenario A, before and after heat integration (HI) Values of CAPEX are reported as USD while OPEX and product sales as USD/year.

CAPEX increased upon heat integration, due to additional equipment and higher system complexity. By contrast, OPEX were of course lower in the heat integrated case, due to lower external utilities. The real advantages in terms of economic expenditure after the heat integration were deepened by evaluating again NPV, IRR and the Pay-out period (Table 1.14).

Table 1.14. Economic evaluation of the scenario A before and after heat integration (HI).

Index	***NPV after 30 years***	***Pay-out period***	***IRR after taxes***
Unit	10^6 USD	Year	%
Before HI	50.8	7.3	24.9
After HI	62.2	6.6	27.1

Both the NPV (absolute profit) and the IRR (efficiency of capital return) increased after heat integration. Of course, these two parameters alone have limits, for example they do not consider the time value of money and are based on average operations during time, excluding important issues such as the variation of maintenance costs over the project life, changing sales volume and so on. In spite of this, they work very well for a general comparison among different projects. Overall, the advantage of reducing OPEX was predominant over the disadvantage of higher capital costs.

The further conversion of CO to CO_2 after the HTWGS stage could be considered apparently worthless, because the remaining small amount of CO is feasible for the separation with the PSA unit. However, this plant design choice was maintained because the integration of CO_2 capture technologies in the process require the larger concentration possible of CO_2 to enhance the efficiency [131,132].

Finally, it should be underlined that no CO_2 selling option has been here included, that would add revenues, but also installation and operation costs. In case, a CO_2 capture unit can be easily implemented because the outlet stream from the PSA unit has the 92% in mass of CO_2 and just the 8% of methane, but it is off-topic for this work.

Sensitivity analysis - A sensitivity analysis was performed to quantify the dependence on changes in market price of raw materials and products (Figure 1.31).

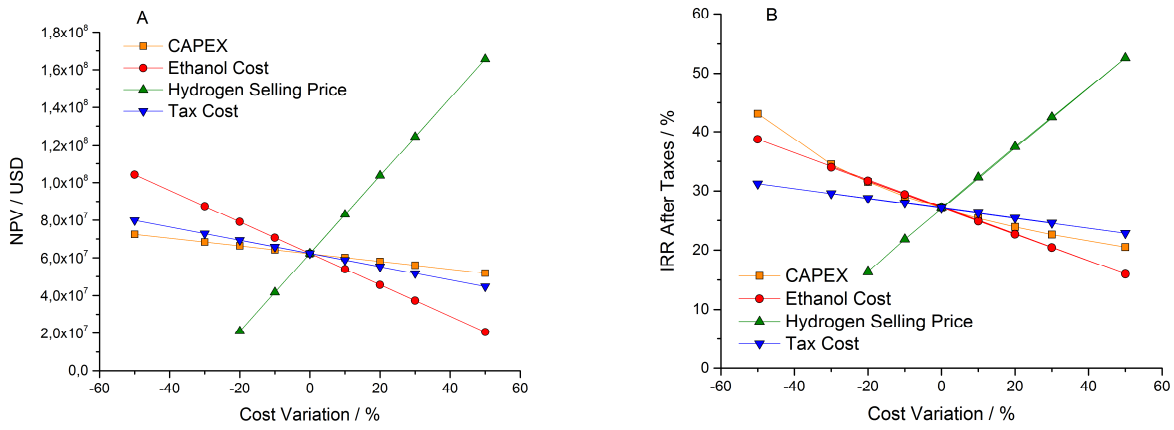

Figure 1.31. Economic sensitivity analysis of the scenario A after heat integration. A) NPV and B) IRR after taxes dependence on cost variation of the various terms listed in the legend.

The process revealed poorly sensitive to taxes and CAPEX variation, whereas changing the ethanol cost was very critical. Its cost strictly depends on the starting biomass and on the purification strategy (use of more or less diluted bioethanol). For this reason bioethanol, as emerging source for energy production, may show higher price volatility than other chemicals. This point further stresses the need to propose poorly expensive routes to bioethanol.

In our hypothesis, we used the cost of commercial 2nd generation ethanol, assuming a 50% reduction of the diluted ethanol price with respect to the pure one. This choice can be considered one of the worst scenarios possible because of two main reasons: i) 2nd generation bioethanol (obtained by lignocellulosic biomass, agricultural residues or waste) is more expensive and more difficult to obtain than 1st generation bioethanol (mainly produced from corn and sugar cane) [133]; ii) the purification of bioethanol may affect up to 50-80% the ethanol production price [91,134]. The upstream biochemical processes (*e.g.* enzymatic hydrolysis, microbial fermentation, biomass pretreatments) were not investigated in this work, making reference to existing papers on the topic [135,136]. We

are basing this analysis on the existing selling costs of 2nd generation bioethanol, but it can be easily adapted to 1st generation feedstock, with consistent savings. However, even if no significant cost saving would derive from the use of diluted ethanol (Figure 1.31b, case with ethanol cost +50%), the system remains profitable, with IRR after taxes still sufficiently higher than 15%.

At last, by selecting the optimized heat integrated process, using methane as fuel utility and selecting an internal rate of return of 10% (which results in a NPV of zero at the end of the project life), the calculated minimum hydrogen selling price would be 1.91 USD/kg, to be compared with a present standard value from methane steam reforming of 1.80 USD/kg [137]. This calculation was made for a system capable of producing 7793 ton/y of H_2 (9886 Nm^3 h^{-1}) starting from 40,000 ton/y of bioethanol.

Conclusion - The process studied is totally carbon free if fuels at the furnace are ethanol or hydrogen, instead in the case of methane the CO_2 produced by the combustion must be taken into account. The influence of this amount on the total OPEX was evaluated considering the worst scenario found in literature (carbon tax equal to 10 USD/tonCO_2) and revealed an influence of the 1.55% on the total operative expenditure (19.4 kton/y of CO_2 produced by the furnace). The further sensitivity analysis considering the variability of this tax due to the different values case by case related to the country policy and regulations, were avoided due to the low impact on the total cost.

The economic sensitivity analysis revealed the OPEX sensitive nature of the process, in particular considering the feedstock cost (ethanol) and hydrogen selling price.

This study was aimed to fill the gap in the literature about the economic assessment of real bioethanol steam reforming implementation on already existing industrial fermentative plants. The study fixes the fundaments for future development in order to compare from an economic point of view other technologies for bioethanol valorization in biorefineries. For example, the ethylene production by dehydration and subsequent polymerization, the use of green hydrogen for the reduction of lignin to produce aromatic compounds or the use of hydrogen for side hydrogenation processes.

2. Ethylene Production

Introduction - At present, a large part of petrochemical products are produced from ethylene, in addition to its large usage as monomer for the production of important compounds such as polyethylene, polyvinyl chloride and polystyrene. For this reason, ethylene production has been considered as one of the indicators to measure the petrochemical development level of countries all over the world. The main way to obtain ethylene is by hydrocarbons cracking [138].

Biomass-derived ethanol can be catalytically dehydrated as a sustainable alternative route in an integrated biorefinery concept, in order to exploit new renewable sources for ethylene production [143]. The bio-polymers market is continuosusly growing and the demand for renewable polyethylene corresponds to 10% of the global market whereas the present supply is less than one tenth. Therefore, routes to ethylene starting from inexpensive and renewable feedstocks should be explored. A commercial application for ethylene production starting from sugar has already been applied in Brazil.

Ethylene production from ethanol dehydration is catalyzed by acid materials. The reaction is endothermal and usually the thermal input is obtained by co-feeding steam, which also allows to prevent catalyst deactivation by coking, unfortunately strongly promoted by acidic sites. Therefore, the use of diluted bioethanol mixtures would be suitable. In this part of the project, the use of a diluted ethanol solution (50 wt.%) for ethylene production was investigated. In particular, operating conditions and catalyst stability/activity toward deactivation phenomena were explored.

Different pathways have been proposed, according to which ethanol is directly dehydrated to ethylene (monomolecular reaction) or etherified to diethyl ether (bi-molecular path) [146]. The latter is considered a reaction intermediate leading to ethylene at relatively high temperature (150 - 300°C) [143]. Ethylene selectivity decays at temperature higher than 400 - 500°C due to formation of higher hydrocarbons and aromatics [149]. Carbon formation by surface polymerization of ethylene is another cause, therefore selectivity and stability issues are predominant over activity for this reaction.

Alumina is the most used catalyst for this application, although significant drawbacks is the deactivation by carbon and the competitive adsorption between ethanol and H_2O. However, zeolites represents a valuable and intriguing alternative of Al_2O_3 [149], but also for them, stability due to carbon formation and H_2O must be taken into account.

BEA zeolite samples with tailored acidity, synthesized in the laboratories of Prof. Stanislaw Dzwigaj (Pierre and Marie Curie University), were studied and tested in this part of the PhD project. The BEA

microporous structure is constituted by channels *ca.* 6.7 Å in size, allowing the ethanol diffusion without tough resistance, considering the molecular size of ethanol (*ca.* 3.8 Å) [150]. The effect of both acidity of zeolite catalysts and reaction conditions has been considered in order to optimize the ethylene selectivity. Metal addition (nickel) has been also investigated as a way to tune process selectivity towards ethylene or syngas, according to the production scope.

2.1. Catalyst preparation and characterization

The catalyst synthesis of the materials with different acidity and Ni loading was carried out in the laboratories of Prof. Stanislaw Dzwigaj (Pierre and Marie Curie University). Briefly, Tetraethylammonium BEA (TEABEA) zeolites with Si/Al ratio of 12.5 and 17 (mol/mol) provided by RIPP (China) were calcined in air (100 °C/h) at 550°C for 15 h under static conditions to remove the organic template. Both the organic-free BEA zeolites were then treated two times with 400 mL of 0.1 mol/L NH_4NO_3 solution during 3 h in order to exchange K^+ and Na^+ ions present in industrial BEA zeolite with NH_4^+ ion. Then, the solids were washed with distilled water and dried overnight at 90 °C. The NH_4AlBEA samples were calcined in air (100 °C/h) for 3 h at 500 °C under static conditions to remove NH_3 and obtain the acidic form of the zeolite BEA, HAlBEA (I) and HAlBEA(II), with Si/Al ratio of 12.5 and 17 (mol/mol), respectively.

The treatment of the TEABEA zeolites with Si/Al ratio of 12.5 and 17 (mol/mol) with nitric acid (13 mol/L) at 80 °C under stirring in air lead to removing of the organic template (TEA) and Al atoms. The treatment has been carried out for short (0.08 h, *partial dealumination,* HAlSiBEA(x)) or prolonged time (4 h, *deep dealumination*, SiBEA(x)).

Ni was added by wet impregnation from a $Ni(NO_3)_2 \cdot 6H_2O$ solution. Proper amount of Ni precursor was dissolved in 200 mL water and the solid suspension was stirred for 24 h at room temperature at pH of 3.3. Then, the suspension was stirred in evaporator under vacuum of a water pump for 2 h in air at 60°C until the water was evaporated.

FT-IR spectra have been recorded in static conditions by a Nicolet Nexus Fourier transform instrument, using conventional IR cells connected to a gas manipulation apparatus. Weighted pressed disks of pure catalyst powders (30 mg) were activated by prolonged outgassing at 500 °C. Pyridine (py, Aldrich, pur. 98%) adsorption experiments have been performed over the activated samples using a standard, reproducible procedure: the sample was contacted with 5 torr of py, then outgassed at first for 30 minutes at room temperature, and further stepwise at increasing temperature (150, 200, 300, 400 and 500 °C). For details about the other characterization techniques adopted see Chapter 1.1.

2.2. Activity tests

The catalysts (*ca*. 0.5 g, 0.15-0.25 mm particle size) were diluted 1:3 (vol/vol) with SiC of the same size. The samples were activated in 50 cm^3/min of a 20% H_2/N_2 gas mixture, while heating by 10 °C/min up to 800 °C for 1 h. For details about the microplant adopted see Chapter 1.1. During the activity tests, the water/ethanol flow rate was 0.017 cm^3/min, added with 56 cm^3/min of N_2, used as internal standard, and 174 cm^3/min of He. The tests were carried out at atmospheric pressure, GHSV = 2500 h^{-1} referred to the ethanol + water gaseous mixture (76500 h^{-1} including the inert gases flow rate). Repeated analyses of the effluent gas were carried out every hour and the whole duration of every test at each temperature was 8 h.

2.2.1. Results and discussion: characterization of fresh samples

The list of samples prepared is reported in Table 2.1.

Table 2.1. Nomenclature, preparation parameters and main physical-chemical properties of the samples prepared.

Sample	Code	Initial Si/Al (atom/atom)	Post-treatment	Ni content (wt.%)	Si/Al (mol/mol) EDX
1	$Ni_{1.5}$HAlBEA(I)	12.5	Calcination	1.5	13.6 ± 0.9
2	$Ni_{1.5}$HAlSiBEA(II)	17	Partial dealumination	1.5	86 ± 16
3	$Ni_{0.6}$SiBEA(II)	17	Deep dealumination	0.6	83 ± 15
4	$Ni_{3.0}$SiBEA(II)	17	Deep dealumination	3.0	73 ± 40
5	$Ni_{4.0}$SiBEA(I)	12.5	Deep dealumination	4.0	92 ± 21
6	$Ni_{0.7}$SiBEA(I)	12.5	Deep dealumination	0.7	150 ± 46
7	$Ni_{1.0}$SiBEA(I)	12.5	Deep dealumination	1.0	96 ± 15
8	$Ni_{1.5}$HAlBEA(II)	17	Calcination	1.5	14.5 ± 1.3
9	$Ni_{1.5}$SiBEA(II)	17	Deep dealumination	1.5	111 ± 14

N_2 adsorption-desorption evidenced the typical isotherms of microporous materials with an evident hysteresis. BET surface area ranged between 320 and 360 m^2/g for every catalyst, with a main contribution of micropores, independently of Ni loading and Al content.

XRD analysis coupled with Rietveld refinement evidenced the contemporaneous presence of the A, B and C polymorphs of BEA zeolite. The A-phase was always the most abundant (46-56 wt.%), followed by the B and C polymorphs (25-30% and 20-25%, respectively) [151]. No correlation between phase composition and sample treatment, dealumination and Ni loading was evidenced. The Ni loading was too low to give rise to reflections in the XRD patterns.

Temperature programmed reduction-oxidation-reduction (TPR-TPO-TPR) cycles have been performed on every sample. Higher reduction temperature usually is ascribed to more dispersed Ni and to metal species more strongly interacting with the support. This can be a key point to prevent the formation of C filaments over metal particles [18]. Indeed, it is known that large size Ni particles are more prone to the formation of carbon nanotubes than smaller ones [3] due to easier subsurface accumulation of carbide species in the case of big metal aisles. Thus, in order to obtain more stable catalysts towards coking, Ni should be dispersed as much as possible during preparation. Sintering should be also avoided by metal stabilization by the support and this can be effectively favored by enhancing the metal-support interaction strength. Therefore, the comparison of TPR cycles can suggest not only the dispersion of Ni and its weak or strong interaction with the support, but also its possible modifications upon activation. An example of the results for samples 5, 6 and 7, characterized by variable Ni loading, is reported in Figure 2.1.

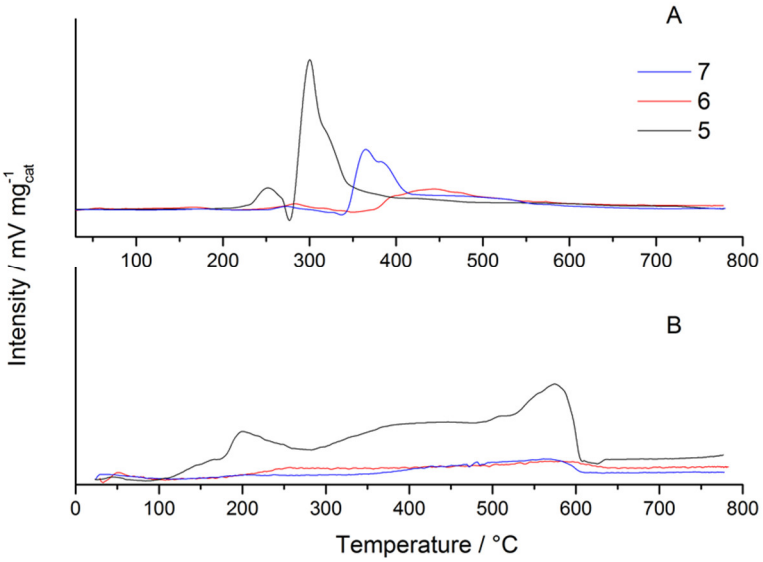

Figure 2.1. TPR pattern of selected samples: a) TPR pattern collected on the fresh sample; b) after the first TPR run and further oxidation at 800°C for 1 h.

The fresh samples (TPR1, Fig. 2.1*a*) evidenced markedly different peak profiles depending on Ni loading. Peak intensity as expected increased with Ni content, but a marked shift towards lower reduction temperature was also observed. Therefore, Ni dispersion and metal support interaction strength progressively decreased with increasing Ni loading in this samples set.

The second TPR cycle collected after oxidation of the reduced sample evidenced a very different behavior. A high temperature reduction peak appeared at 550-600°C, which was attributed to the re-

dispersion of Ni during the previous thermal treatments (simulating catalyst activation before testing). The formation of Ni-silicates can be supposed, ending in Ni species more dispersed and strongly interacting with the support. The same results were observed for samples 3,4,9.

When increasing the Al content, *i.e.* sample acidity, the reduction pattern was generally shifted to lower temperature, indicating a lower Ni dispersion. This means that increasing the Al content induced a weakening of the metal-support interaction. Furthermore, the redispersion phenomenon upon activation above outlined was favored at high Si/Al ratio (deep dealumination), as expected due to the formation of silicates, being much less evident for the calcined, more acidic, samples.

FT-IR analysis were carried out in collaboration with Professor Gianguido Ramis at the Università degli studi di Genova, in order to investigate the acidic character of the prepared catalysts. Detailed attribution of the peaks is reported in the reference [158]. Below the summary of the key results.

In the hydroxyl region of the spectra, recorded after outgassing at 500°C (spectra not reported) several common features appear for samples 1 and 8 (calcined samples): terminal Si-OH groups, bridging Al-OH-Si groups responsible of strong Brønsted acidity, Al-OH groups with Al partially connected to the BEA framework Isolated Al-OH groups. The latter family is due to extra-framework (EF) Al, were detected for sample 1, having the highest Al content.

After dealumination, the disappearance of bridging Al-OH-Si groups confirmed the progressive disappearance of Brønsted acidity. The dealumination leads to the creation of vacant sites without modifying significantly the zeolite structure as testified by XRD data [166]. On the contrary, different dealumination methods, such as the solid state one proposed by Müller et al. [161] for this application, consisting in isomorphic substitution of aluminum with silicon, predominantly removed extra-framework Al, leaving the framework Al sites substantially unaffected.

Pyridine, whose kinetic diameter is reported to be 0.533 nm, can actually enter the main channels of the BEA structure therefore accessing the strongly acidic bridging OHs located within the channels, whose characteristic band indeed disappears after pyridine adsorption, confirming their full titration. The characterization of BEA catalysts is indeed broadly addressed in the literature using Py, used even with smaller size pores, such as those characteristic of MFI zeolites [164] and even if diffusional limitations can occur for the smallest pores, operating under static conditions with sufficient equilibration time should avoid this problem.

Pyridine adsorption at room temperature over sample 1 (Figure 2.1) led to the detection of strongly adsorbed pyridine species coordinated over Lewis acidic sites, together with pyridinium ion, due to the interaction with Brønsted acidic centers.

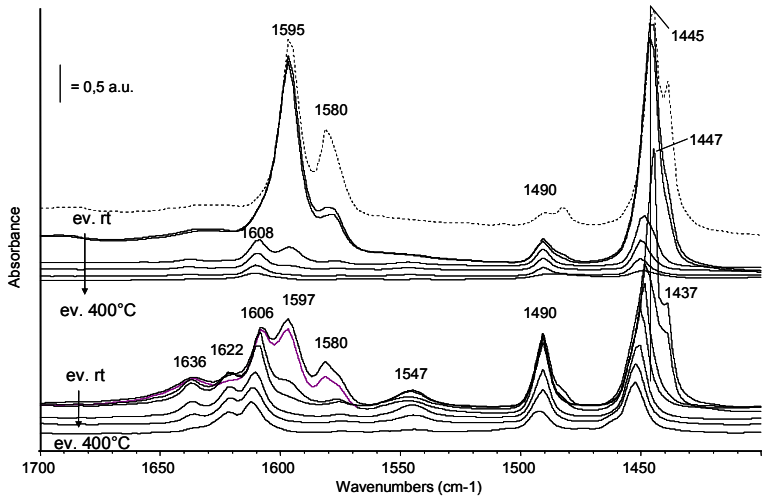

Figure 2.2. FT IR subtraction spectra of the surface species arising from pyridine adsorption and desorption at increasing temperatures over samples 1 (bottom) and 2 (top). Spectrum of pyridine adsorption and desorption following prolonged outgassing at room temperature over sample 3 (broken line).

The thermal evolution of these species has been reported in the same Figure 2.2 from room temperature up to 500 °C, leading to the disappearance of the bands due to H-bound pyridine and better evidencing the components assigned to Py coordinated over Lewis acidic Al^{3+} ions. Features due to adsorbed pyridine, although reduced in intensity and slightly shifted towards higher frequencies, can be detected up to 500 °C pointing out the strength of the pyridine coordination over both Lewis and Brønsted surface sites.

In Figure 2.3 (bottom) the spectra related to pyridine adsorption and outgassing over sample 8 are reported from room temperature to 500 °C. Spectra are completely consistent with those reported for sample 1, for instance bands due to Brønsted acidic sites are detected together with bands due to pyridine coordinated over Lewis acidic sites having different strength.

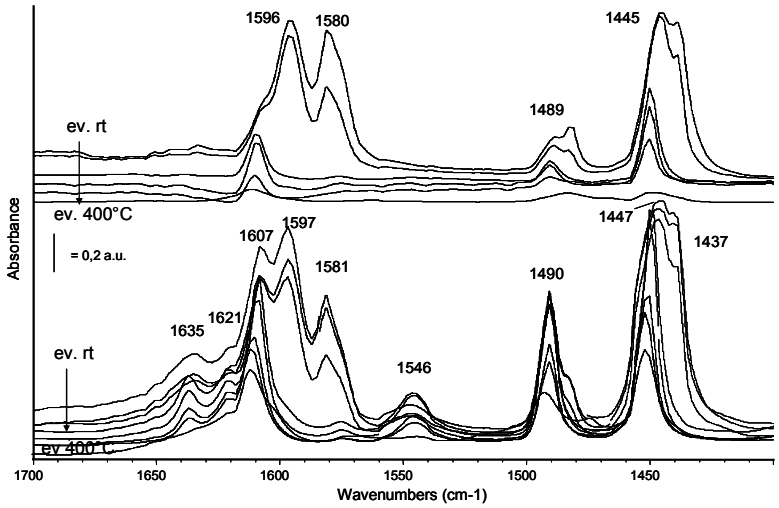

Figure 2.3. FT IR subtraction spectra of the surface species arising from pyridine adsorption and desorption at increasing temperatures over samples 8 (bottom) and 9 (top).

On the other side, the overall intensity of the pyridine bands, compared for all samples in the subtraction spectra recorded after outgassing at 200 °C is slightly reduced for sample 8 in comparison with spectra of catalyst 1, because of the absence of EF Al sites. Moreover, the relative intensities of bands typical of pyridinium ion and molecular coordinated pyridine, which is a rough indication of the acidic character of these zeolites, is slightly higher for sample 8 than sample 1.

Pyridine adsorption and desorption by outgassing at increasing temperatures has also been performed over the partially and deeply dealuminated samples 2, 3 and 9, whose spectra are reported in Figure 2.2 and 2.3 (top). As for samples 2 and 3 (Figure 2.2 top, and Figure 2.3 broken line), the main bands attributed to weakly bound pyridine, possibly H-bound to silanol, readily disappearing after outgassing.

The comparison with the spectrum of pyridine adsorbed over samples 1-3 evidenced that from sample 1 to sample 2 and 3 there is a decrease in the relative intensity of bands due to pyridinium ions, which completely disappear in sample 3. From sample 1 to sample 2, the overall intensity of the pyridine bands (Lewis and Brønsted acidic sites) appears significantly reduced, suggesting the reduced acidity of zeolites.

Pyridine adsorption over sample 9 (Figure 2.3, top) shows a very similar behavior and no residual Brønsted acidity can be detected anymore.

In conclusion, FT IR experiments provide evidence of the extensive dealumination of samples 2,3 and 9, resulting in the removal of most of framework and extra-framework Al ions and indeed in changes of the amount and the nature of acidic sites. In fact, over these samples Brønsted acidity disappears as well as the strongest Lewis sites.

2.2.2.Results and Discussion: activity tests

The results of activity testing for samples with the same Ni loading (1.5 wt.%) and variable acidity is reported in Table 2.2.

Table 2.2. Results of activity testing at 500 °C after activation at 800 °C, water/ethanol = 3:1 mol/mol, GHSV = 2500 h^{-1}. Effect of catalyst acidity.

Sample	*1*	*8*	*2*	*9*
Si/Al	13.6	14.5	86	111
Ni (wt.%)	1.5	1.5	1.5	1.5
Ethanol conversion (%)	100 ± 0.00	100 ± 0.00	100 ± 0.00	100 ± 0.00
C balance (%)	93 ± 3	98 ± 3	102 ± 3	98 ± 4
S CH_2CH_2 (%)	93 ± 3	99 ± 3	91 ± 1	66 ± 3
S CH_3CHO (%)	0.00 ± 0.00	2 ± 2	3 ± 2	18 ± 1
S CH_4 (%)	0.00 ± 0.00	0.00 ± 0.00	0.00 ± 0.00	0.00 ± 0.00
CO/CO_2 (mol/mol)	-	-	1.22 ± 0.09	2.7 ± 0.2

Full ethanol conversion was attained for every catalyst. As expected, the most acidic catalysts were more active for ethanol dehydration, leading to > 90% selectivity to ethylene. Decreasing catalyst acidity imparted higher activity for ethanol dehydrogenation to acetaldehyde and to steam reforming. The activity for the water gas shift reaction was also depressed by decreasing acidity, as testified by the higher CO/CO_2 molar ratio of sample 9. Carbon balance also increased with decreasing acidity due to lower coking rate.

Dealumination has been proposed as a mean to decrease not only acidity, but also hydrofilicity [161]. More hydrophobic samples were presented as more active for ethanol dehydration, since Al sites may competitively adsorb water and ethanol, so limiting activity. In the present case we did not observe any correlation of this kind. The effect of Ni loading is presented in Table 2.3.

Table 2.3. Results of activity testing at 500 °C after activation at 800 °C, water/ethanol = 3:1 mol/mol, GHSV = 2500 h^{-1}. Effect of Ni loading.

Sample	*3*	*9*	*4*	*6*	*7*	*5*
Si/Al	83	111	73	150	96	92
Ni (wt.%)	0.6	1.5	3.0	0.7	1.0	4.0
Ethanol conversion (%)	100 ± 0.00	100 ± 0.00	100 ± 0.00	100 ± 0.00	100 ± 0.00	100 ± 0.00
C balance (%)	103 ± 3	98 ± 4	95 ± 3	97 ± 3	98 ± 3	92 ± 4
S CH_2CH_2 (%)	66 ± 7	66 ± 3	0.00 ± 0.00	77 ± 10	33 ± 4	0.00 ± 0.00
S CH_3CHO (%)	31 ± 4	18 ± 1	20 ± 5	16 ± 3	33 ± 4	15 ± 2
S CH_4 (%)	0.00 ± 0.00	0.00 ± 0.00	15.8 ± 0.5	0.00 ± 0.00	0.00 ± 0.00	17 ± 1
CO/CO_2 (mol/mol)	-	2.7 ± 0.2	0.9 ± 0.1	-	2.0 ± 0.2	1.45 ± 0.09

The choice to add a metal phase is based on previous studies on products distribution at variable temperature. Increasing the operating temperature, together with water addition may improve catalyst life, although Phung et al. [146] observed decreasing ethylene selectivity at increasing temperature due to the formation of higher alkanes and olefins. Ni addition is helpful to prevent the formation of such compounds by favoring their reforming, so leading to a more interesting gaseous mixture, which is much easier to fractionate and purify than hydrocarbon/olefin mixtures. Indeed, in the present work no trace of higher hydrocarbons, nor of diethyl ether, has been observed. On the other hand, such a limited Ni loading prevents extensive reforming of the produced ethylene. A comparison with the bare zeolite HAlBEA(II) is also presented in Table 2.4, showing a higher selectivity to ethylene and higher carbon balance for the Ni-loaded sample than for the bare acidic catalyst.

Table 2.4. Results of activity testing at 500 °C after activation at 800 °C, water/ethanol = 3:1 mol/mol, GHSV = 2500 h^{-1}. Comparison with reference catalysts and different conditions.

Sample	*8*	*8 (GHSV = 570000 h^{-1})*	*HAlBEA(II)*	*γ-Al_2O_3*
Si/Al	14.5	14.5	14.5	-
Ni (wt.%)	1.5	1.5	0	-
Ethanol conversion (%)	100 ± 0.00	19 ± 2	100 ± 0.00	100 ± 0.00
C balance (%)	98 ± 3	98 ± 3	96 ± 8	88 ± 7
S CH_2CH_2 (%)	99 ± 3	64 ± 6	89 ± 5	80 ± 7
S CH_3CHO (%)	2 ± 2	36 ± 5	2.96 ± 0.17	3.7 ± 0.3
S CH_4 (%)	0.00 ± 0.00	-	0.00 ± 0.00	0.87 ± 0.15
CO/CO_2 (mol/mol)	-	-	0.31 ± 0.09	-

Therefore, the increase of selectivity here achieved by adding very low metal loading is able to decrease sensitively the ethylene separation/purification costs.

The two catalysts series prepared from different BEA native samples at variable Ni loading presented the same features. After deep dealumination the Si/Al ratio did not result exactly the same. However, from a practical point of view, the acidity of the samples did not change appreciably when passing from Si/Al=86 to 111 (quantitative comparison of bands relative to acidity for samples 2 and 9 are identical), so that the performance variation can be essentially ascribed to the variation of Ni loading. When increasing Ni amount, a decreasing activity for ethanol dehydration was observed, with the contemporaneous increase of activity for steam reforming, ethanol decomposition (increasing selectivity to methane) and water gas shift (decreasing CO/CO_2). Carbon balance also decreased with increasing Ni loading. Therefore, if the goal is ethylene production deep dealumination and high Ni loading should be avoided.

FT-IR analysis showed that the dealumination treatment induced a depression of both Brønsted and Lewis acidity, with consequent drop of selectivity to ethylene and decreased coking activity. A difference was noticed in selectivity to ethylene also between the two calcined, more acidic samples: sample 8 exhibited more stable and higher selectivity to ethylene than sample 1 (Figure 2.4).

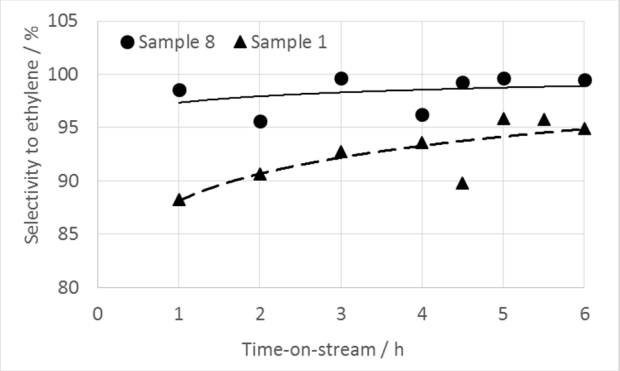

Figure 2.4. Selectivity to ethylene vs. time-on-stream at 100% ethanol conversion, 500°C for sample 1 and 8.

Sample 8 was characterized by similar Brønsted acidity, but lower Lewis contribution than catalyst 1 and no EF Al sites. This confirms the effect of Lewis acidity for ethylene formation and for catalyst deactivation by coking [165]. Lewis acidity is needed to form ethylene, but excessively strong (likely EF) Lewis acidic sites should be avoided to protect from coking. Indeed, sample 1 showed lower selectivity to ethylene during the first h-on-stream with respect to sample 8, likely due to coking on the Lewis most acidic sites. Selectivity to ethylene on sample 1 increased with time-on-stream due to rapid rule out of strongly acidic sites, however keeping lower plateau selectivity to ethylene with respect to sample 8 during the whole duration of the test. These results also imply much more limited role of Brønsted acidic sites on activity with respect to recent literature reports on similar materials, very likely due to the different reaction conditions [146].

A comparison with γ-Al_2O_3 has been also carried out (Table 2.4). The Ni/BEA samples here tested were characterized by the same full ethanol conversion, but higher selectivity and carbon balance with respect to the bare alumina catalyst. A progressive decrease of selectivity has been also observed at high time on stream (4-8 h).

The effect of water is still under debate. Using raw bioethanol (*ca*. 10 wt.% ethanol in H_2O) was detrimental both in terms of conversion and selectivity for alumina and titania-based catalysts [149]. Therefore, also the effect of temperature seems contradictory, depending of the selected feed. In the absence of water, temperature higher than 200 °C depress ethylene selectivity due to the formation of byproducts, whereas by co-feeding water temperature should be increased to avoid the decrease of

activity and selectivity. The effect of acidity was as expected pivotal [167,168] and water co-feeding was reported to effectively tune acidity towards Brønsted type. The latter is reported as particularly effective for the present application [154], whereas the present data and the mechanism proposed below deal with both types of acidity, i.e. Brønsted (likely formed in excess water and relatively low temperature) and Lewis sites (if dehydration occurs at equilibrium at high temperature even in the presence of excess water).

A recent work by Xin et al. [166] reported the stable geometries or ethoxy species, ethylene and dietyil ether, when adsorbed in the vicinity of Al Lewis sites in ZSM-5. The reaction mechanism relies on Brønsted acidic sites, which are also involved in dimer formation. The same sites are also at the basis of the mechanism proposed by Chiang et al. [141]. In the present work diethyl ether was never observed, so a dimolecular reaction mechanism, introduced for ethanol dehydration on other materials can be excluded. We can interpret the mechanism of ethanol dehydration based on Al Lewis acidic sites as follows (Figure 2.4).

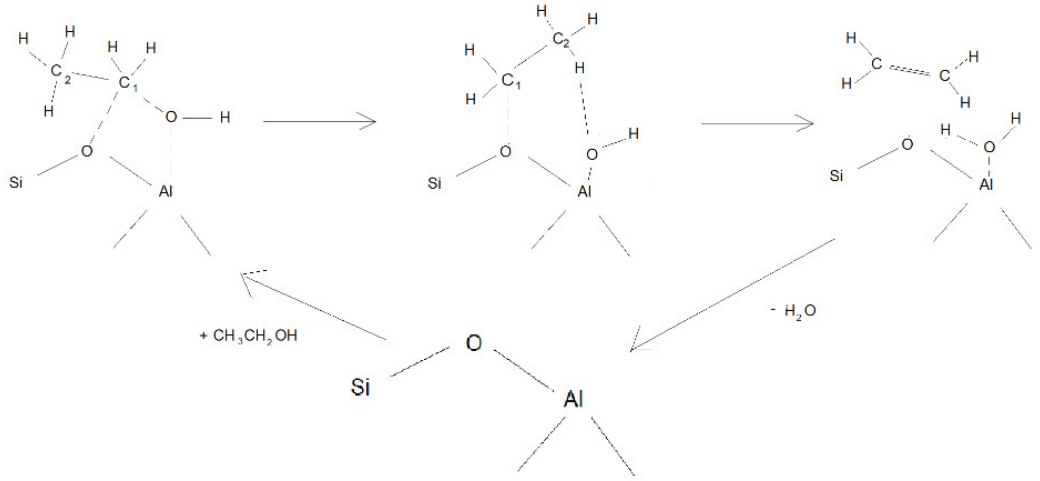

Figure 2.4. Possible path for ethanol dehydration through interaction with an Al Lewis acidic site.

The Al Lewis acidic site can coordinate ethanol forming an ethoxy intermediate, which then evolves to ethylene and water that desorb. Water can compete with ethanol for adsorption on the Lewis acidic site, but in such case a Brønsted acidic site forms, which is involved in the mechanisms already very well detailed in the literature [146,149]. It should be mentioned that in such papers the attention is focused on the conditions that drive the possible parallel or consecutive steps towards diethyl ether. The latter forms when two adjacent sites are occupied by two adsorbed molecules of ethanol. In the present case, co-feeding water helps preventing significant selectivity to the dimer and higher alcohols by diluting the feed and thus competing with ethanol for adsorption.

The addition of small amounts of Ni allowed to keep under control undesired heavier olefins without depressing selectivity to ethylene. Furthermore, Chiang et al. [141] discussed the ethanol dehydration

mechanism over MFI, ferrierite and mordenite zeolites. The bimolecular pathway for ethylene formation through ethanol dimerization is allowed by bigger channel size in the case of mordenite, whereas it is forbidden for smallest pores. BEA catalysts have somehow bigger pores than mordenites, so the two reaction pathways (mono and bi-molecular dehydration) are expected to coexist. In the present case, selectivity to diethyl ether can be effectively suppressed in the presence of Ni and by operating at sufficiently high temperature while cofeeding water.

Based on the interesting performance of sample 8 we tested it for 80 h-on-stream at 500°C, water/ethanol = 3:1 mol/mol after activation at 800°C. Full ethanol conversion was maintained for the whole test, with average selectivity to ethylene = 99 ± 3. No evidence of by-products was observed, except some traces of CO, hardly quantifiable. Carbon balance remained constantly 99 ± 3 without any evidence of catalyst deactivation during time-on-stream (Figure 2.5).

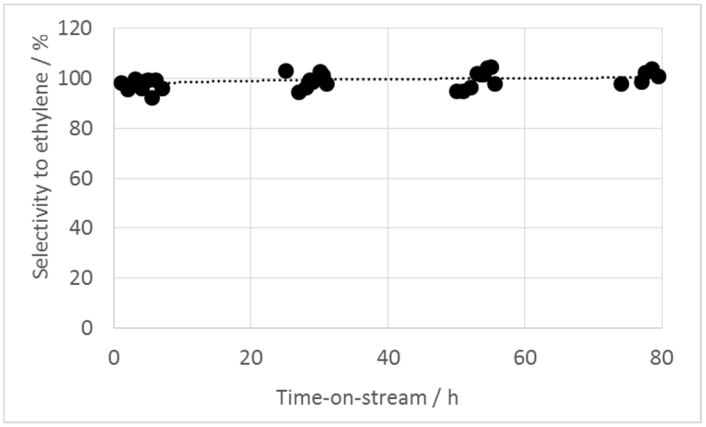

Figure 2.5. Durability test for sample 8, selectivity to ethylene vs. time-on-stream at 100 % ethanol conversion, 500 °C.

The present BEA catalyst proved effective for this application when properly tuning surface acidity. Ethanol dehydration has been mostly studied over ZSM5 and alumina [172,173]. Alumina did not reach the same high selectivity as the present catalyst 8 and led to lower carbon balance. Poor stability has been observed for ZSM5 due to the presence of strong acidic sites, leading to heavy coking. Attempts to stabilize the catalyst with alkali additives were not effective. By contrast, by increasing pore size the residence time in the pores can be decreased, so improving catalyst life, as in the case of the present BEA catalysts [184].

Additional testing at very high GHSV has been carried out on catalyst 8 (Table 2.4) in order to test selectivity below full conversion. This is not a trivial task when operating at high temperature due to the very high reactivity of ethanol. We tested the sample at 500 °C in order to avoid lower temperature ranges which would likely induce different resistance to coking. Ethanol conversion was decreased

by decreasing contact time (i.e. increasing the GHSV). In order to lower conversion below 60% we were forced to apply dramatically high GHSV = 570,000 h^{-1}, testifying the high activity of this sample. The initial conversion was 54%, stabilizing to ca. 18% after 4-8 h-on-stream. Selectivity to ethylene decreased to ca. 64%, the remaining products being acetaldehyde and hydrogen. Thus, at very low contact time, the dehydrogenation path becomes competitive with the dehydration one.
FE-SEM and TEM micrographs have been collected on every spent sample and the most representative ones are reported in Figure 2.6-2.8.

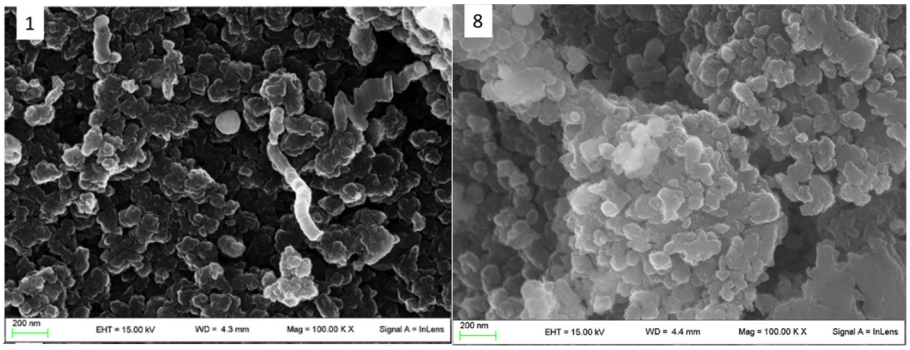

Figure 2.6. FE-SEM micrographs of selected spent samples. Sample codes are reported in the relative pictures. Marker size = 200 nm.

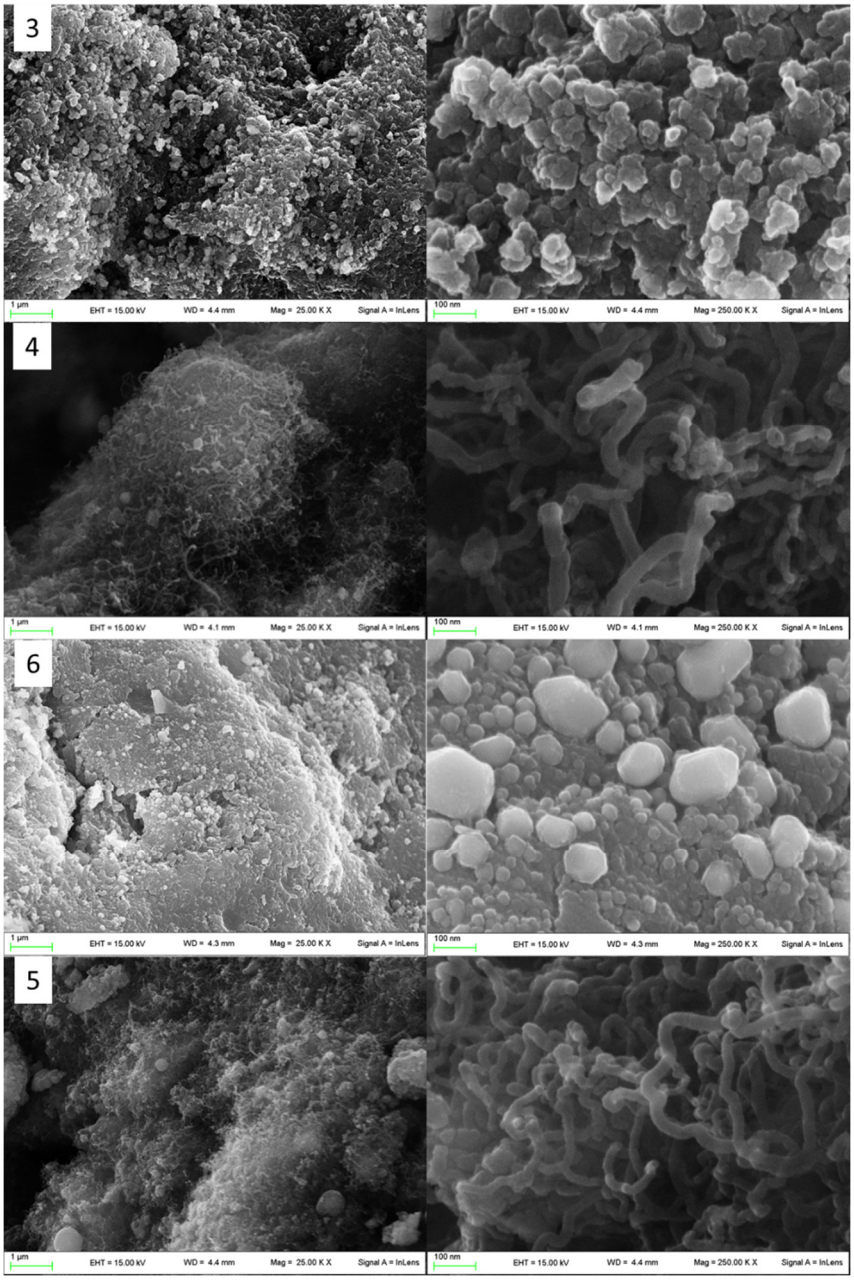

Fig. 13: TEM micrographs of selected spent samples. Sample codes are reported in the relative pictures. Marker size = 100 nm.

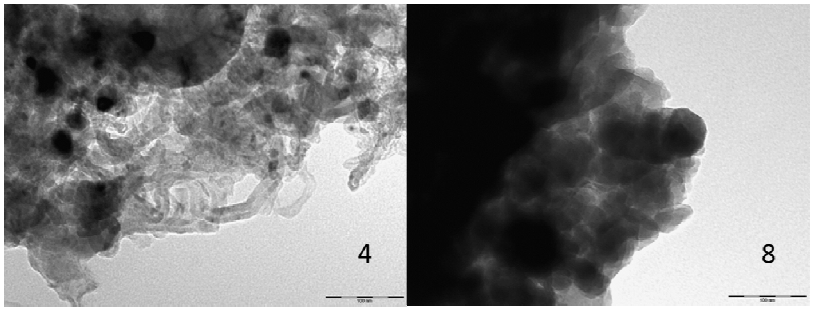

Figure 2.6. FE-SEM micrographs of selected spent samples. Sample codes are reported in the relative pictures. Marker size = 1 μm for the images in the left column, = 100 nm for the right column representing the same samples at higher magnification.

Different coking contributions may be present. Catalyst acidity may induce the polymerization of ethylene over the strongest acidic sites. Some C deposition can be also ascribed to the formation of C nanotubes over Ni. C balance was optimized by selecting proper operating conditions to avoid significant coke accumulation over the catalyst surface, also thanks to co-feeding water at relatively high temperature. Nevertheless, some samples exhibited non negligible deviation from 100% C balance: samples 1, 4 and 5. For sample 1, the main contribution is expected to be correlated to its high acidity. However, by looking at Figure 2.6 some carbon filaments may be noticed. Carbon nanotubes usually grow on large size Ni particles, which allow extensive subsurface carbide accumulation. TEM micrographs of the fresh catalyst 1 evidenced a lower Ni dispersion with respect to comparative samples with the same Ni loading. Furthermore, the TPR run carried out on the fresh sample 1 evidenced a weak metal-support interaction, thus indicating the presence of Ni species more prone to sintering. This may explain the formation of some C nanofilaments.
When considering samples 4 and 5, however, by far more extensive coking revealed, due to carbon nanotubes formation (Figure 2.7 and 2.8). Nanotubes were instead absent for catalysts with lower metal loading. Some Ni sintering was also evident for samples 4 and 5, with Ni particle size becoming poorly homogeneous up to 25 nm. Thus, catalysts characterized by higher Ni loading and lower metal-support interaction strength, as demonstrated by TPR, are more prone to sintering and to form C filaments. At last, no coking evidence was observed for sample 8 (Figure 2.6 and 2.8), in spite of its prolonged use for 80 h-on-stream.

Conclusion - The possibility to use diluted ethanol streams for ethylene production has been demonstrated and BEA zeolites have been proved interesting catalysts for the scope. The Si/Al ratio and consequently catalyst acidity was the main parameter influencing catalyst selectivity to ethylene and durability, followed by Ni loading. Dealumination of the native zeolite depressed the selectivity to ethylene due to poor catalyst acidity, but care should be also paid to excessive Lewis acidity. Ni proved an effective mean to limit the production of heavier olefins, diethyl ether and hydrocarbons with respect to literature reports, although increasing Ni loading decreased the selectivity to ethylene by favoring the ethanol decomposition and/or reforming paths.

3. CO conversion

Introduction - The carbon monoxide oxidation to CO_2 is a significant process in the H_2 purification sequence, as broadly explained in Chapter 1. Moreover, CO oxidation is one of the most studied processes [186] and allows the design of different kind of catalysts. One of the main examples is gold, which is catalytic active for the reaction but very sensitive to particle size and oxidation state [178]. Remarkable activity is showed when Au is highly dispersed on the oxidic supports, such as TiO_2 and Fe_2O_3 [179,180]. Supported gold nanoparticles (AuNPs) have a broad application in many heterogeneous catalytic processes. [191] Several parameters influence the catalytic performance of AuNPs such as the particle size, the oxidation state, the nature of the support, the synthetic method and the activation procedure for controlling the final morphology. The oxidation state of Au during CO oxidation is a crucial but controversial topic, largely debated in literature [183]. Several works reported higher activity of oxidized gold than of metallic gold [179,184]. However, the adsorption of CO on Au^{n+} is strongly inhibited by the presence of H_2O, so metallic states are needed for the adsorption of CO and, hence, for the whole oxidation process. On the other side, different studies pointed out the important contribution of negatively charged Au [162,198]. The preparation method is tightly related with dispersion, size and electronic state of AuNPs, which in turn affects catalytic activity [187]. Deposition-Precipitation (DP) method for the formation of highly dispersed gold nanoparticles on several oxidic supports is one of the most successful methods reported in literature [191,201]. Urea ($CO(NH_2)_2$) is considered one of the most common basic agents for the DP method [205] widely used also in other preparation procedures such as the co-precipitation synthesis [194]. Regarding the final reduction step, the use of sodium borohydride ($NaBH_4$) as chemical reductant is a promised method at room temperature to obtain metallic gold nanoparticles with very narrow size distribution [195]. Its potential is proved also for other metals, such as Pd [196], Pt and Sn [197]. However, the combination of these two steps is still relatively unexplored in the literature, especially for low metal loading. Recently Kumar and co-workers applied this synthetic route for the preparation of 1-4 wt.% Au-TiO_2 samples for the oxidation of benzyl alcohol in gas phase, with great success [198].

Therefore, in this part of the project several samples prepared by a new modified DP method with urea and chemical reduction (DP-UC), characterized by very low Au loading (0.1 wt.%, 0.2 wt.%, 0.5 wt.%) were tested for the CO oxidation. Degussa P25 TiO_2 was chosen as commercial support in order to eliminate any complications related to the support synthesis. I*n situ* IR spectroscopy was used to identify and characterize the surface metal sites of the catalysts synthesized by the DP-UC method. Infrared absorption spectroscopy is considered one of the most promising methods to study

catalysts surface. A multitude of different applications and experimental techniques are available [199], such as Transmission (TIR), Attenuated Total Reflection (ATR), Reflection-Absorption (RAIRS) or Diffuse Reflectance (DRIFTS) modes. In this work the latter technique was used, which allows to analyses fragile solids, not amenable to manipulation to produce self-standing samples with high intensities bands. The use of this technique to investigate the adsorption of several probe molecules permits to further extend the features of this method [200]. Surface characterization with various NO_x compounds was deeply studied by Hadjiivanov and co-workers,[214] and several basic probes are widely used for the determination of surface acidity [203,204]. One of most studied probes for metal nanoparticles is CO, providing useful information on metal surface exposure and on the nature of metal sites [203,205–207]. Moreover CO is an important reactant in several industrial processes such as the production of methanol [208], the Monsanto process and in many cases it is an undesirable pollutant or poison [209]. The ability of this molecule to adsorb on nanoparticles is well known in the case of Au by the formation of different surface carbonyls, depending on the charge of the gold site, Au-support interaction and particle size. This feature allows the discrimination of cationic, metallic and anionic sites because of a direct correlation with CO absorption frequencies [183].

The vibrational frequency of the C–O stretching is very sensitive to the strength and mode of bonding, but mainly it is related to the electronic state of the metal. In particular, the higher is the frequency (from 1900 cm^{-1} to 2200 cm^{-1}) the higher is the charge of the metal site (from M^{n-} to M^{n+}) [205]. Comparison of the bands position with other published reports suggest to emphasize that CO absorption frequencies are influenced: (i) by the partial pressure of CO in the gas flow [200,223], (ii) by the presence of other molecules like H_2O, O_2 or H_2 [197] and, mainly, (iii) by the adsorption temperature [214]. Therefore, bands attribution was carried out considering these key points not always followed in literature. Complementary techniques were used to shed light on dispersion and local charge of the AuNPs, such as HRTEM, STEM and XPS.

This part of the PhD project was carried out at the Cardiff Catalyst Institute of the Cardiff University (UK) under the supervision of Dr Nikolaos Dimitratos (from April/2015 to August/2015).

3.1. Catalyst preparation and characterization

Gold nanoparticles were prepared by a modified deposition-precipitation method using urea and a chemical reductant (DP-UC). This technique was carried out and optimized in the laboratories of Professor Laura Prati and Dr. Alberto Villa at Università degli Studi di Milano. 1g of TiO_2 (Degussa P25, 50 m^2 g^{-1}) was dispersed in distilled water (100ml) with 5g of urea (Aldrich, >99%). $NaAuCl_4 \cdot 2H_2O$ solution (Aldrich, 99.99%) was added to the support and let under vigorous stirring for 4h at 353K. The catalyst was filtered and washed several times with water. The material was then suspended in distilled water and a freshly prepared solution 0.1M of $NaBH_4$ (Fluka, >96%) was added ($NaBH_4$/Au = 4mol/mol) under vigorous stirring at room temperature. The sample was filtered, washed and dried at 373K for 4 h. The actual Au loading was checked by Atomic Absorption Spectroscopy (AAS) analysis of the filtrate, on a Perkin Elmer 3100 instrument. As expected using this method [215], all the gold present in the solution was deposited on the support. Au/TiO_2 catalysts with the following composition were prepared: 0.1 wt.%, 0.2 wt.%, 0.5 wt.% Au/TiO_2. Bare P25 was used as reference.

DRIFTS studies were carried out with a Bruker Tensor 27 spectrometer fitted with a HgCdTe (MCT) detector, a Harrick Praying Mantis HVC-DRP-4 cell equipped with two ZnSe windows, and operated with OPUS software. The DRIFTS cell included gas inlet and outlet ports as well as capabilities for heating and cooling. The required gas flow, 40 cm^3 min^{-1} of a 5% CO/N_2 gas mixture was controlled by mass-flow controllers. The data are reported in the form of absorbance. Each spectrum represents an average of 64 scans collected with a spectral resolution of 2 cm^{-1}. The ZnSe windows used cut off the spectrum below 650 cm^{-1} therefore this region was not included in the discussion. In the reported spectra, a positive increase of peak intensity indicates an increase of population of that species, whereas a negative deflection shows loss of moieties associated with that particular mode. All samples were ground before the analysis. Background subtraction and normalization of the spectra were performed by subtracting spectra recorded under N_2 flow after heating the sample at 393 K for 30 min, to eliminate physisorbed and chemisorbed moisture. The gas-phase CO signal was removed by subtracting a spectrum obtained on pure KBr in CO-containing atmosphere under the same analysis conditions.

X-ray photoelectron spectroscopy (XPS) was performed using a Kratos Axis Ultra-DLD photoelectron spectrometer that employed a monochromatic Al K_α X-ray source operating at 144 W power. High resolution and survey scans were performed at pass energies of 40 and 160 eV,

respectively. Spectra were calibrated to the C (1s) signal at 284.8 eV, and quantified using CasaXPS and a modified Wagner sensitivity factors supplied by the manufacturer.

The specimens for Transmission Electron Microscopy (TEM) were prepared by dispersing the catalyst powder on TEM grids coated with holey carbon film. They were examined by means of a FEI Titan 80–300 electron microscope equipped with CEOS image spherical aberration corrector, Fischione model 3000 high angle annular dark field (HAADF) scanning transmission electron microscopy (STEM) detector.

For specific surface area determination see Chapter 1.1.

3.1.1.DRIFTS Study on CO Adsorption

For all the Au/TiO_2 samples analyzed, the presence of CO gave rise to one or two IR bands in the C-O carbonyl spectral region (1950 – 2150 cm^{-1}) showed in Figure 3.1. The IR bands assignment are presented in Table 3.1.

Table 3.1. IR Bands Assignment for Au/TiO_2 DP-UC Samples.

Species	*ν_{CO} (cm^{-1})*	*Ref.*
Linearly adsorbed CO on Au^0	2106	[190,214,216–218]
Linearly adsorbed CO on $Au^{\delta-}$	2072	[209,219–224]
Multisites and bridged CO on $Au^{\delta-}$	2054-2043-2013	[185,205,213,225]

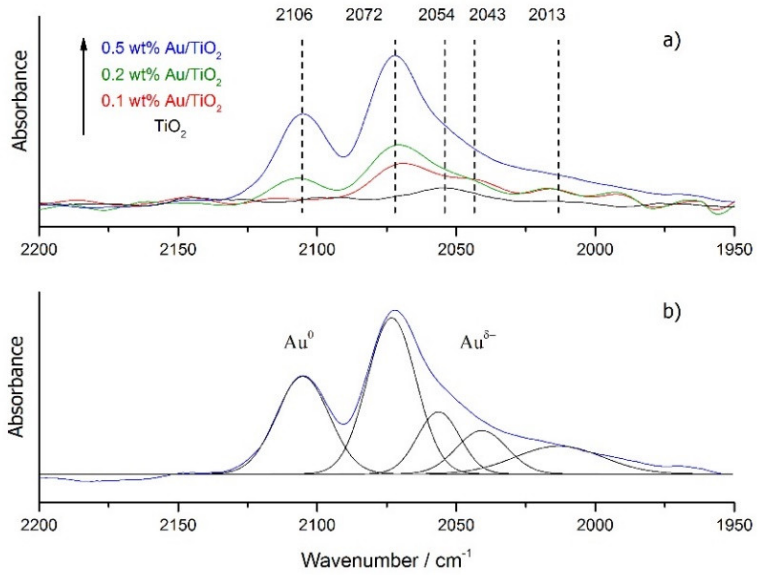

Figure 3.1. DRIFTS spectra of CO adsorbed at 298K on 0.1 wt.%, 0.2 wt.% and 0.5 wt.% Au/TiO_2 (a) and detailed deconvolution for 0.5 wt.% Au/TiO_2 (b)

The highest frequency band (2106 cm^{-1}) was attributed to linearly adsorbed CO on metallic gold, in agreement with the literature [190,210,214,216–218]. Another broad and asymmetric band was detected at lower frequencies (Figure 1*a*). The maximum was located at 2072 cm^{-1} and the band was composed by several overlapping peaks. CO stretching mode signals were deconvoluted on the basis of a Gaussian model using the Origin software. Results of this procedure are shown in Figure 1*b*. The presence of other bands at lower frequencies than 2100 cm^{-1} is not common like the linear adsorption of CO at 2100-2120 cm^{-1}. Some publications reported the formation of these bands at lower frequencies for catalyst where Au was strongly reduced [209,219–224,226]. Their origin is attributed to the linear and multisite adsorption (probably bridged-bond configuration) of CO on negatively charged gold ($Au^{\delta-}$ sites). A detailed approach is presented by Sterrer *et al.* [225], for Au-MgO film, where the position of the bands was directly correlated to the charge of the site with a strong red shift due to the π-back-donation of the negatively charged metal to the CO antibonding orbital. Also, the degree of coordination to the site, which is tightly correlated to shape and size of the nanoparticle, has an influence. Boronat *et al.,* confirmed this phenomenon underling that the shift in the ν_{CO} frequency depends not only on the charge of the particle, but also on the degree of coordination of gold atoms and the capability of CO to modify the particle shape [227]. The shift of the bands due to the adsorption conformation of CO on the metal particles is well known also for other elements, especially for Pt-based catalysts [228,229]. In a recent work Rogers *et al,* prepared several Au/TiO_2 catalysts using a standard sol-immobilization technique with $NaBH_4$ as final reductant. No peaks relative to Au^+ cations were detected, while band at 2115 cm^{-1} and at 2040 cm^{-1} were attributed to metallic and partially negative charged gold respectively [230].

Summarizing, it can be concluded that the lower is the frequency (i) the lower is the coordination to the metallic site and (ii) the smaller is the size of the gold particles. This is the explanation of the CO stretching bands observed in our Au/TiO_2 DP-UC catalysts and allows explaining the observed overlapping peaks. In particular, the peak at 2072 cm^{-1} can be attributed to a linear adsorption of CO on partially negative gold sites and peaks at lower frequencies (2054 cm^{-1}, 2043 cm^{-1}, 2013cm^{-1} for the sample with the highest metal loading) to multisite adsorption of CO in different bridged configuration, depending on the degree of back-donation of Au to CO [185,205,213,225]. The absence of carbonyl bands relative to oxidized gold Au^{n+} implies that Au was entirely reduced to zerovalent species as expected by using excess of $NaBH_4$ [221,231,232] and in agreement with the XPS data. The nature of the negative charge on gold is tightly related to the support [183], in particular regarding the charge transfer between gold particles and M^{3+} cations of the support lattice [233,234]. To further elucidate the nature of the IR-bands, DRIFTS spectra after various exposure times to CO were recorded (Figure 3.2).

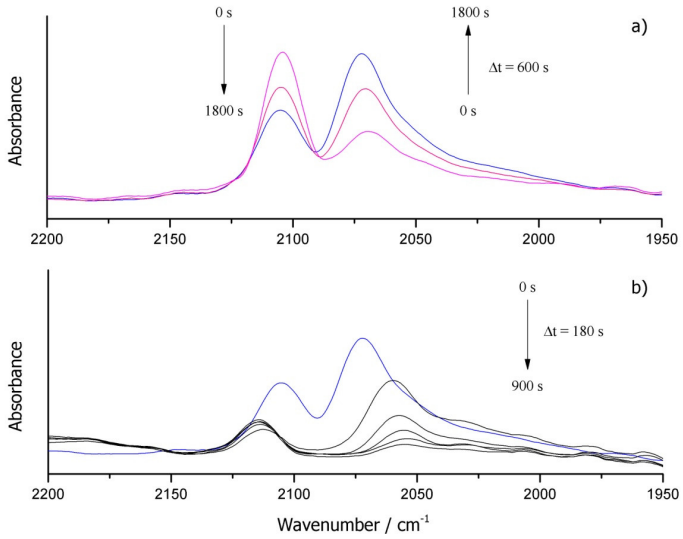

Figure 3.2. DRIFTS spectra of 0.5 wt.% Au/TiO_2 at different CO exposure time (a) and during the evacuation after saturation (b).

In clear accordance with Chakarova *et al.* [187] for Au/SiO_2 catalysts and Bollinger *et al.* [235], the increase of the exposure time involves a gradual reduction of Au^0 to $Au^{\delta-}$ because of the greater stability of the last species directly correlated with the greater π-back donation [236]. Similar behavior was reported for other supported gold catalysts, like Au/MgO [185,225] and Au/CeO_2 [222]. This effect allows to understand the absence of linear CO adsorption on Au^0, which probably derives from the complete reduction to the partially negative analogue. These results underline the importance of reporting the interaction time between the probe molecule and the substrates during this powerful common analysis, because CO modifies electronically the catalyst surface.

The CO desorption analysis (Figure 3.2*b*) showed as expected a progressive red shifting of the 2072 cm^{-1} band due to the higher stability of different carbonyls formed on Au. However, a low intensity band at 2114 cm^{-1}, blue shifted during the desorption with respect to the initial 2106 cm^{-1} due to the surface coverage effect [237], still remained after 900 s. The very small amount of low coverage CO bound to Au^0 derive probably to the residual CO in the gas feed, very hard to remove totally.
For bare TiO_2, only one very low intensity band appeared at 2054 cm^{-1}. This data ruled out any possibility to attribute a strong contribution of CO-Ti^{n+} interaction for the metal loaded samples, because only low temperature CO adsorption can allow to monitor this weak interaction [238]. This explanation was in accordance to the spectroscopic IR investigations carried out by our group at lower temperature on Ni and Cu supported on TiO_2 [13,152] and other groups with Au/TiO_2 samples.
A direct proportional correlation between the area of IR-CO stretching band and metal loading was obtained as presented in Figure 3.3.

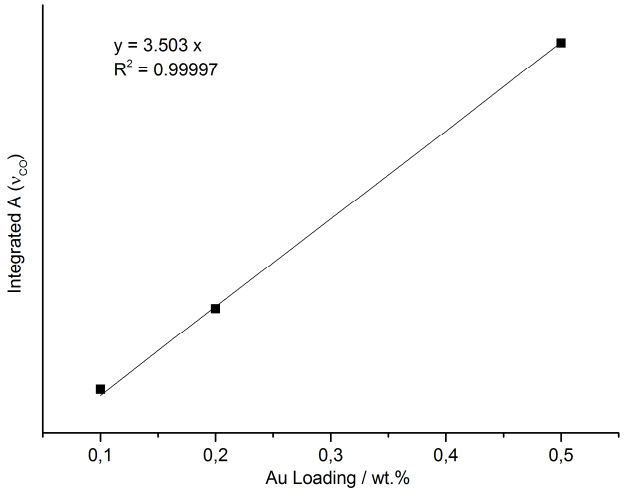

Figure 3.3. Integrated area of CO-stretching bands in DRIFTS spectra (2106cm^{-1} – 2013cm^{-1}) *vs.* Au loading (wt.%).

In general, the interpretation of intensities and the area of the DRIFT signals are difficult due to the several variables involved in the analysis such as cell geometry, sample loading procedure and deposition method used [199]. However, a strong direct correlation was observed here. This means that the variation of Au dispersion among the catalysts was too small to see variation in the position and intensity of the bands IR spectra. Moreover, it means that also the kind of metal sites formed can be considered similar because otherwise different CO adsorption, which can be linear or multisite, could not lead to such a direct correlation.

The attribution of the low frequency broad band to the multisite adsorption with different configuration on partially negative charged gold sites with a slightly different degree of back-donation between Au and CO is clearly in accordance with DFT calculation carried out by Rogers *et al.* for Au/TiO_2 DRIFT analysis [230]. The presence of these gold species could be related with the last chemical reduction step used during the synthesis. Indeed recently Rojas *et al.,* synthesized several Au/TiO_2 samples by a DP method using urea but with a final high temperature reduction step in H_2 and they didn't observe the negatively charged gold species by CO-IR spectroscopy [239]. On the contrary, Sandoval and co-workers obtained CO-stretching bands at lower frequencies although they used the DP-urea method with a final H_2 step so this point still remains unclear [240]. The assignment of the carbonyl stretching bands needed further investigation and combination of complementary techniques to shed light on metal nanoparticles properties. In this view, other complementary techniques were here employed.

3.1.2. Morphologic and Electronic Characterization

Gold particle size distribution was determined by HRTEM and STEM. The representative images and respective histograms are shown in Figure 3.4 and confirmed that DP-UC method led to very narrow gold particle size distribution fitted by a log-normal curve. Mean diameter of Au particle size and relative standard deviation are presented in Table 3.2.

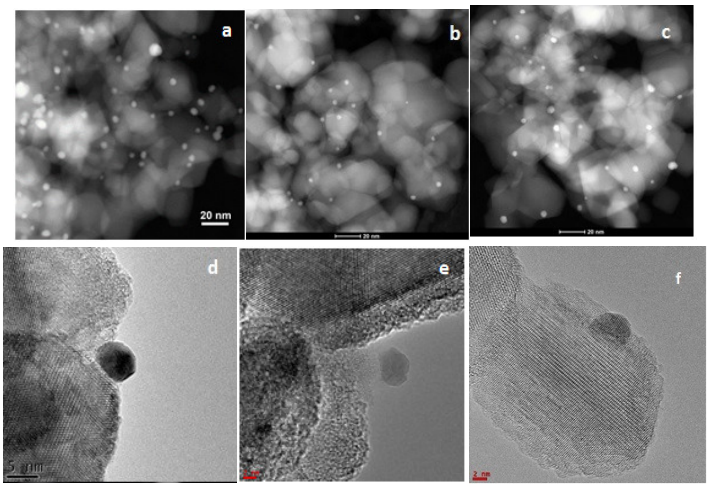

Figure 3.4. Representative STEM (a,b,c), HRTEM (d,e,f) and particle size distributions (g,h)

Table 3.2. Statistical Median of Particle Size Analysis, Specific Surface Area (SSA), XPS Au/Ti Ratio and Binding Energy of Au ($4f_{7/2}$) Region Data for Gold Based Catalysts.

Sample	*Statistical Median (nm)*	*Standard Deviation (nm)*	*SSA (m^2/g)*	*Au / Ti (mol/mol)*	*Au $4f_{7/2}$ BE (eV)*	*Au $4f_{7/2}$ BE After CO Ox (eV)*
0.1 wt.% Au/TiO_2	3.7	0.9	52	0.00226	83.6	83.6
0.2 wt.% Au/TiO_2	4.0	1.0	55	0.00260	83.6	83.7
0.5 wt.% Au/TiO_2	4.6	1.6	50	0.00482	83.6	83.6

These results allow to better explain the attribution of the broad band at low frequency observed in DRIFTS spectra. Indeed, the broadening could be due to a multisite adsorption with different configuration or to bridged CO on differently sized gold nanoparticles. The combination of these techniques confirms the former hypothesis.

To elucidate the nature of the gold species XPS was employed. The Au_{4f} XPS spectra of Au/TiO_2 samples are shown in Figure 3.5 where the characteristic doublet of the two spin–orbit components are visible ($4f_{7/2}$ and Au $4f_{5/2}$ transitions).

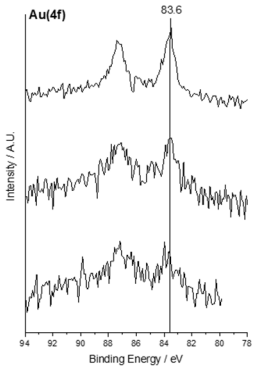

Figure 3.5. XPS spectra of Au (4f) region for 0.1 wt.%, 0.2wt.% and 0.5wt.% Au/TiO_2 samples (from the bottom to the top respectively).

The oxidation state of Au at the surface of the catalyst was evaluated by analysing the values of binding energy (BE) of the Au $4f_{7/2}$ peak. The BE of 83.6 ± 0.2 eV corroborates the results obtained by FT-IR and TEM that Au is in the metallic state (Au^0) and well dispersed without Au^{n+} species (BE = 85.5 and 86.3eV). [195,241–243] The slight decrease to lower BE than the typical values obtained for metallic gold could be attributable to the different charging of the metal particles or to the particle size effect [244]. HRTEM and STEM analysis ruled out any possible size effect (negative shift should be related to much larger particle size), therefore, in accordance to the DRIFTS results, lower values of BE were attributed to the contribution of gold with partially negative charge [245]. The contribution of $Au^{\delta-}$ was smaller with respect DRIFTS analysis because XPS was carried out without CO. As a final remark, the increase of the intensity in the XPS data fits well with the increase of metal loading.

3.2. Activity tests: results and discussion

Catalytic activity for CO oxidation was investigated using a fixed bed U-shape glass reactor with 3mm internal diameter placed in thermostatic controlled oil bath. Reactive flow (5000 ppm CO in synthetic air) was fed to the reactor through mass flow controllers and 50 mg of catalyst were used in order to obtain a Gas Hourly Space Velocity (GHSV) of 4000 h^{-1}. Analysis of oxidation products was performed using an online gas chromatograph, equipped with a carbosieve column (3m x 35mm) and a thermal conductivity detector. Before the test, all samples were dried in oven overnight at 353 K. Conversion data were calculated relative to the CO_2 production and the detector was calibrated using standard gas mixtures. Catalyst productivities are reported as TOF considering the number of surface exposed atoms. Calculations of this parameter was performed by assuming that all the nanoparticles

had cub-octahedral morphology with cubic close-packed structure in this size range using the model of full-shell nanoparticles: [246]

$$\text{TOF-B} = \frac{\text{mol CO}}{\text{mol Au x h}}$$

$$\text{TOF-N}_s = \frac{\text{TOF B}}{\text{A}}$$

$$\text{A} = \frac{\text{Ns}}{\text{Nt}}$$

Where TOF-B is TOF based on bulk Au using the weight measured by AAS, TOF-N_s based on Au surface exposed atoms, A is the fraction of Au atoms lying at the surface [247], N_s is the number of Au surface atoms and N_t is the total number of Au atoms.

3.2.1.Structure-Activity Correlation for CO Oxidation

To get a closer insight into the relation between the results obtained, CO oxidation activity tests were performed. For this process nanoparticles finely dispersed are very important because bulk gold proved chemically inactive [179,227]. Moreover, understanding the active electronic state is fundamental to explain the mechanisms involved in the oxidative process. Tests were carried out at room temperature without the addition of water in order to rule out the influence of its variation. Sample 0.5 wt.% Au/TiO_2 showed at room temperature a TOF-Ns = (6.1 ± 0.3) x 10^{-3} h^{-1} and steady state conditions were achieved after 20 minutes. A prolonged activity test under reaction conditions was carried out for more than 6 h without any decrease of conversion as it is shown in Figure 3.6.

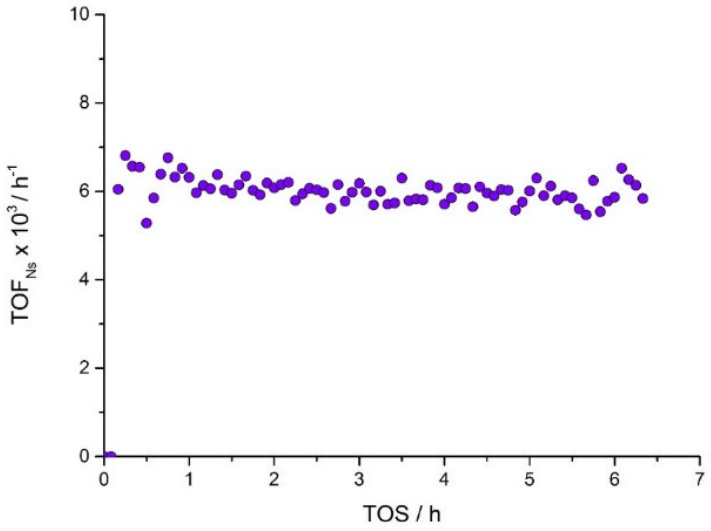

Figure 3.6. Time-on-stream (TOS) data expressed in TOF_{Ns} (h^{-1}) for 0.5 wt.% Au/TiO_2 (T = 298K, GHSV = 4094 h^{-1}, 5000 ppm CO in synthetic air).

This fact confirmed the stability under the operating conditions adopted, with no appreciable deactivation. The effect of temperature was studied for every catalyst and the relative Arrhenius plots are reported in Figure 3.7.

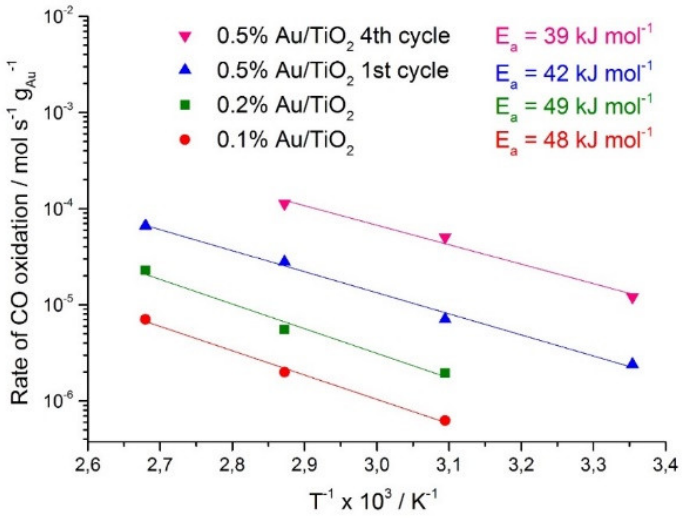

Figure 3.7. Arrhenius plots and relative apparent activation energies for the CO oxidation process for 0.1 wt.% (orange), 0.2 wt.% (green), 0.5% (blue), and 0.5 wt.% Au/TiO_2 after the 4th cycle (pink).

The apparent activation energy of the CO oxidation reaction in the 298-373 K range was estimated from the slope of the logarithm of the intrinsic kinetic rate (mol s^{-1} g_{cat}^{-1}) vs T^{-1} x10^3 (K^{-1}) plot. Similar values of activation energy were obtained for 0.1 wt.% Au and 0.2 wt.% Au, whilst a significantly lower value was calculated for the highest metal loaded sample. These values fall in the typical range reported in literature for CO oxidation under dry conditions [235,248] (Table 3.3) and for Au/TiO_2 prepared by DP-urea method [240], although in general a strict comparison should consider that the activation energy is directly correlated with the particle size, surface area, CO concentration and residence time.

Table 2.3. Comparison of Au/TiO_2 Catalysts Synthetized and Tested for CO Oxidation Processes.

Au Loading (wt.%)	*Au Particle Size (nm)*	*Preparation Method*	*Apparent E_a (kJ mol^{-1})*	*Refs.*
0.1-0.5	3.7 - 4.6	DP-UC	39-48	This work
0.1-1.0	2-10	DP-NaOH	35-39	[249]
0.1	-	PAMAM	82	[250]
4.0	3.2	DP-U	35	[240]

We achieved relatively low activation energy with lower Au loading and much more uniform Au particle size with respect to other literature reports. In order to ensure a kinetically controlled regime

with the operating conditions adopted, several tests at room temperature varying the space velocity in the range of 4000-16000 h^{-1} were carried out (Figure 3.8).

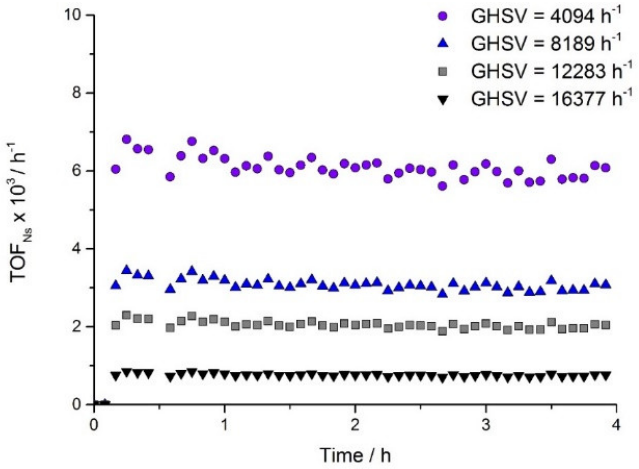

Figure 3.8. Influence of the space velocity in the range of 4094 h^{-1} - 16377 h^{-1} (2.44 h - 0.61 h in term of contact time) for 0.5 wt.% Au/TiO_2 (T = 298K, 5000 ppm CO in synthetic air).

The linear increase of the TOF with increasing the contact time (Figure 3.9) was a clear proof that under the given reaction conditions diffusional transport effects within were negligible.

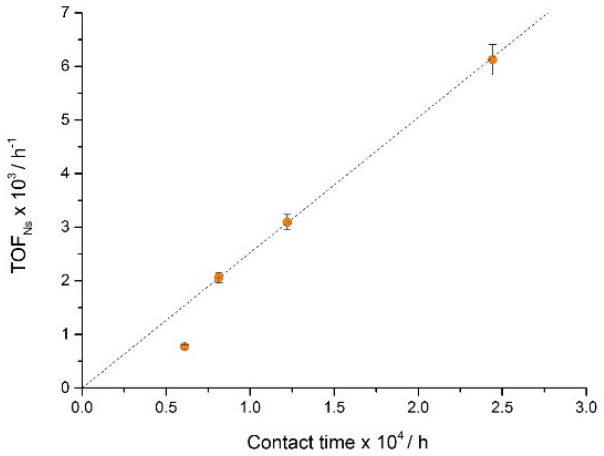

Figure 3.9. Linear plot TOF vs. contact time in the range of 2.44 h - 0.61 h (4094 - 16377 h^{-1} in term of gas hourly space velocity) for 0.5 wt.% Au/TiO_2 (T = 298 K, 5000 ppm CO in synthetic air).

The results demonstrated the activity of metallic and partially negative Au also at such very low loading. An important contribution was given by the presence of low coordinated Au sites in accordance with DFT calculations [251].

To better understand the role of metal loading at this very low concentration for samples prepared by this new modified in-situ deposition method (DP-UC), the Au % surface obtained by the Au/Ti ratio from the XPS atomic composition data and the Au % bulk were plotted versus the CO oxidation rate at 323 K (Figure 3.10).

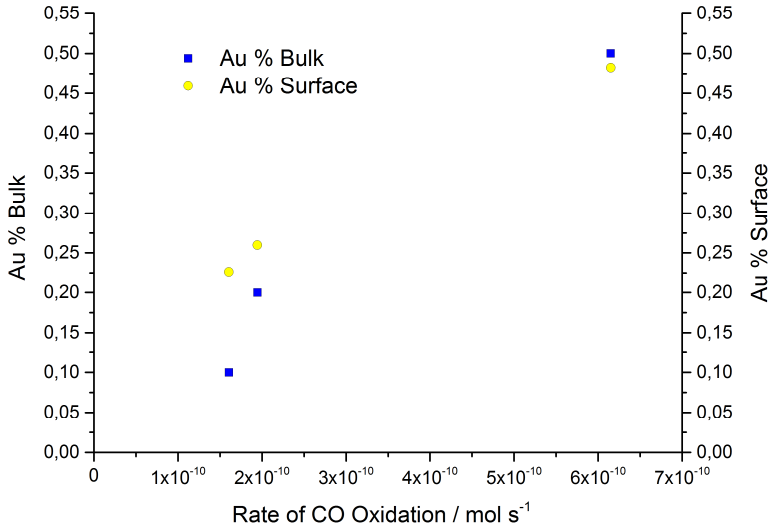

Figure 3.10. Au % surface and Au % bulk plotted vs. Rate of CO oxidation.

The trend observed confirms the direct relationship between the catalytic activity, the dispersion and the number of active sites exposed on the oxidic surface. This fact also means that all the metal deposited by this modified DP method remains on surface without penetrating inside the pore or in the material bulk.

The role of the support in the CO oxidation reaction is fundamental [183]. In this specific case, the primary function is the stabilisation of Au nanoparticles, which, else, would coalesce irreversibly. Furthermore, as confirmed by DRIFTS analysis the CO-Ti^{n+} interactions are very weak, and, indeed, they do not influence directly the process. However, the electronic density and distribution of the AuNPs are strongly perturbed by the interactions with the supports, with related consequences on the catalytic activity especially in the case of the oxides. In addition, surface hydroxyls promote the charge transfer between CO and AuNPs changing the activation energy of the process [252]. The state of TiO_2 in the samples was confirmed by XPS analysis and did not vary appreciably with Au loading. For the sample with the best activity, *i.e.* the one with 0.5 wt.% metal loading, repeated cycles were performed at different temperatures using a GHSV equal to 8200 h^{-1} (Figure 3.11).

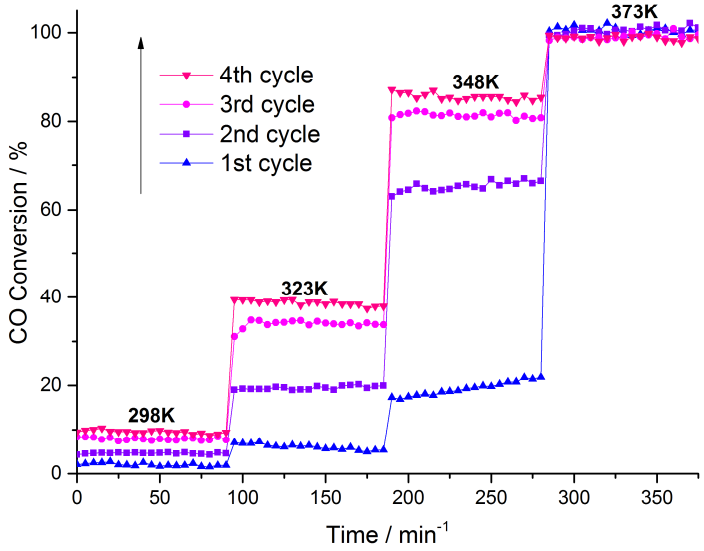

Figure 3.11. Repeated cycles of activity tests at different temperatures for 0.5 wt.% Au/TiO_2.

The results for subsequent cycles were substantially different, showing an increase of catalytic activity. Several factors could influence this phenomenon:

a) variation of particle size;
b) variation of the gold oxidation state;
c) alteration of the water content;
d) decrease of carbon layer formed during the synthesis from urea decomposition.

The low operating temperature (≥ 373 K) ruled out any sintering phenomena, and the increase of activity from the first to the last cycle further confirmed that no increase of particle size occurred. The comparison of the XPS data for the Au $4f_{7/2}$ peak of the fresh and used samples (Table 3.2) indicated that no change of oxidation state occurred during the reaction and the BE typical of zero valent gold was detected for the spent samples. Therefore, the variation of catalytic activity for subsequent runs cannot be attributed to the variation of the metal oxidation state, because BE of the Au after the first run showed *ca*. the same value after the fourth run. No change of water content was detected during the chromatographic analysis. Thus, subsequent investigation aimed at evaluating the presence of organic compounds on the surface, as common when preparing metal nanoparticles by using organic agents.

Lari *et al.,* reported the influence of the thermal treatment for 1 wt.% Au/TiO_2 samples prepared by sol-immobilization with stabilizing ligands like PVP and PVA and naked supported gold nanoparticles prepared by DP [237]. They observed higher activity for DP catalyst before any heat

treatment because lower amount of carbon was present on the surface. Comotti *et al,* drawn the same conclusions using a protecting agent and studying with repeated cycle testing the inhibitory effect of the organic protector on the surface for CO oxidation [237]. However, in those papers the DP method for the deposition of the gold did not make use of urea. In order to explain this last hypothesis, the fresh catalyst was investigated using DRIFTS without any probe molecule. In the beginning a comparison between IR spectra at room temperature for Au/TiO_2 samples and bare P25-TiO_2 was done but without the detection of any significant bands from their subtraction. However, differences between the bare P25 and samples with Au appeared during IR analyses at different temperature. Spectra of 0.5 wt.% Au/TiO_2 were collected in a range of temperature between 373 K and 420 K, investigating different exposure time at 420 K (30 min, 60 min, 90 min, 150 min). Spectra subtracted by the same analysis at room temperature are shown in Figure 3.12.

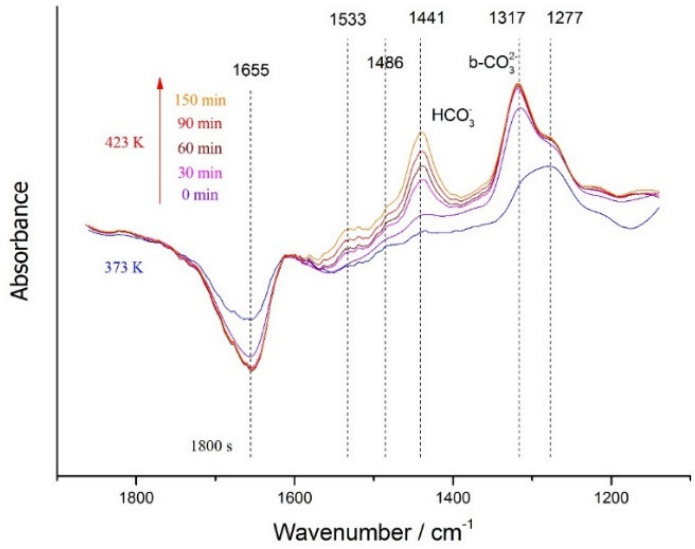

Figure 3.12. DRIFTS spectra of 0.5 wt.% Au/TiO_2 under N_2 flow at different temperature (373 K and 423 K) and exposure time at 423 K (0, 30, 60, 90, 150 min) subtracted from the spectrum collected at 298 K.

The same procedure was carried out for the bare P25, but only for the gold catalyst several bands appeared in the region between 1000 cm^{-1} and 2000 cm^{-1}. In particular, strong signals at 1441 cm^{-1} and 1317 cm^{-1} appeared, with shoulder and lower peaks at 1583 cm^{-1}, 1486 cm^{-1}, 1277 cm^{-1}, without any band at higher wavenumbers. Unfortunately, broad desorption of physisorbed water did not allow to reveal peaks around 1650 cm^{-1}, and its elimination was impossible because any pre-treatment was done for maintaining the same initial condition adopted before the CO oxidation test. These bands belong to the carbonate region and can be assigned to the N-compounds or carbonate species formed during the decomposition of urea. Larrubia *et al,* in a adsorption/decomposition study of several N-

compounds including urea on iron-titania catalysts, obtained several strong bands attributed to the NH–C=O stretching mode near 1565 cm^{-1}, 1490 cm^{-1} and in the region below 1300 cm^{-1} [253]. Fang *et al,* reported a similar attribution for the urea thermolysis for the urea-SCR process; in particular bands at 1500 cm^{-1} attributed to the imine group and at 1100 cm^{-1} attributed to C-O linkages derive from the keto-enol configuration exchange [254]. Recently, Bernhard *et al,* confirmed the presence of these lower frequencies bands and they attributed the band around 1560 cm^{-1} to the asymmetric Ti-OCN-Ti stretching mode of adsorbed urea on titania [255]. However, in contrast with these results, no peaks at higher wavenumbers were detected in our analysis and, moreover, no N 1s peak was revealed in XPS data in the BE region around 400 eV. This can be explained by the removal of carbamate and NH_3 in the washing procedure and heat treatments performed during the synthesis. Therefore, the attribution was carried out considering the carbonate formed during the urea decomposition step, because CO_2 formed can react in small part with lattice oxygen on the gold-support interface [220]. The strong peak at 1317 cm^{-1} was assigned to the bidentate carbonate (b-CO_3^{2-}) on titania surface [256], while peak at 1441 cm^{-1} to the bicarbonate (HCO_3^-) species. The other peaks at 1533cm^{-1}, 1486cm^{-1} and 1277 cm^{-1} can be attributed to weak signals relative to the presence of carbonate [257].

CO adsorption before and after thermal treatment didn't show any shift of the CO stretching bands, and this means that: i) the carbon layer present on the surface is very thin because it did not prevent the adsorption of CO on gold nanoparticles like in the case of synthesis which use protecting agents [237,258]; ii) the presence of this thin organic layer did not influence gold dispersion or the electronic state. The attribution of bands for the present samples was in accordance with the interpretation summarised above and it was confirmed by further characterization through XPS, which is a powerful tool to obtain quantitative and qualitative information on carbon amount over the surface of a catalyst [191,259]. A decrease of the organic content over the surface of the catalysts after the reaction was indeed confirmed, since a considerable loss of the amount of carbon was detected and monitored by decreasing intensity of the C 1s peak (from 23.5 wt.% to 19.0 wt.%).

Conclusion - CO oxidation was kinetically studied in order to correlate the physicochemical features of the AuNPs prepared with the catalytic activity. A deep characterization was carried out by means of DRIFT spectroscopy and CO as probe, to deepen the understanding of a modified gold deposition strategy, and demonstrating a good activity for CO oxidation at lower loading and without thermal treatment for the final reduction step of the synthesised Au nanoparticles.

4. CO_2 conversion to regenerated fuels

Introduction - Nowadays CO_2 emissions represent one of the most critical issues to the environment due to their considerable contribution to the increase of global warming in the last centuries. The correlation between CO_2 increasing emissions and the use of fossil fuels has been undoubtedly established, but new methods for its conversion and sequestration must be applied.

A very attracting strategy is the conversion of carbon dioxide into fuels which might lead to a real circular economy avoiding the use of net CO_2-producing energy sources: in this way, the product of hydrocarbons combustions, i.e. water and carbon dioxide, are converted in regenerated fuels in a sort of "artificial photosynthesis".

Over the years, CO_2 photocatalytic reduction attracted the attention since it is able to use light as primary energy input, that in a foreseeable future, might be obtained by the sun. The presence of a photocatalyst and its physicochemical properties are essential to the development of a robust and reliable process. At the moment, several semiconductors have been employed (such as ZnO, ZnS, WO_3, Fe_2O_3, ZrO_2) but titanium dioxide based materials are the most promising due to large availability, low cost and appropriate band-gap for this application [260].

Despite a great effort on the development of an efficient photocatalyst, the choice of the optimal reaction conditions is not a secondary issue. Due to the novelty of this technology and the flourishing of publications on this topic, different rigs configurations are reported in literature. Water use both as reagent and as solvent, has been deeply investigated in liquid phase conditions due to its great availability, inexpensiveness and environmental friendliness. However, drawbacks are the low carbon dioxide solubility, which hinders the possibility for CO_2 to interact with the catalyst dispersed in the reaction medium. To overcome this problem, several strategies have been pursued over the years. The substitution of water with organic solvents, such as methanol, isopropanol or acetonitrile, proved to be effective to increase carbon dioxide solubility and thus photoactivity, despite a negative effect on the economic and environmental sustainability of the process. Another possibility is the use of alkali solutions as reaction medium. In this case, carbon dioxide is dissolved as bicarbonates ions, which are more stable in the aqueous medium but, unfortunately, are characterized by a higher reduction potential, limiting process efficiency.

An alternative possible and most promising strategy is to boost reaction conditions. The increase in pressure allows to increase carbon dioxide uptake in reaction medium, so as to increase reduction products and the overall process productivity.

In this part of the project, an innovative photoreactor concept, which allows to improve CO_2 solubility in water by increasing the pressure, was adopted. Temperature, pressure and pH are very critical parameters for the CO_2 photo-reduction processes and their comprehensive study were carried out in previous investigations of our research group [261,262]. The mechanism of the photoreduction of CO_2 in liquid phase (H_2O was used as solvent), using a commercial TiO_2 (EvoniK P25) photocatalyst in the presence of Na_2SO_3 as hole scavenger and working at different pH, was deeply investigated in this part of the PhD project. Particular attention was devoted to the influence of operating parameters on the mechanism and kinetics of the reaction. Using the high-pressure photoreactor, we identified both liquid and gaseous products in variable amounts, depending on the reaction time and the operating parameters identified.

In addition, the loading of the bare titania by gold was further investigated. Indeed, the drawbacks of bare TiO_2 are the high electron–hole recombination rate and the limited absorption in the visible region. An attractive method to improve these limitations is the modification of TiO_2 by means of non-metal elements or surface metallic nanoparticles [263]. The influence of the dopant is very different in these two cases. Doping involves the incorporation of atoms or ions in the crystalline oxide lattice, although the real location of the hetero-atoms is not always clear [264].

On the other hand, deposition of metallic nanoparticles, such as Pt, Pd, Ag and Au, onto TiO_2 surface could enhance the photocatalytic activity by suppressing electron-hole recombination due to the formation of a Schottky barrier at the interface between the metal and support. Since the TiO_2 conduction band is essentially formed by the overlapping of Ti 3d orbitals, the presence of the metal introduces an empty *d* orbital below the conduction band edge, causing the effective band gap reduction and acting as trap for charge carriers.

The modified deposition-precipitation method used for CO oxidation in Chapter 3 was selected for the preparation of photocatalyst for the reduction of CO_2. The materials were tested for the CO_2 photo-reduction in liquid phase at high pressure (7 bar). The low metal loading (0.1-0.5 wt.%) was chosen to avoiding excessive surface coverage and relative inhibition of substrate adsorption but maintaining visible light absorption properties and enhanced electron-hole separation after the photo-generation.

4.1. Photo-activity tests

4.1.1. High pressure tests using TiO_2

Photocatalysts and reagents - Commercial nanometric titanium dioxide P25 by Evonik was suspended in water with a concentration of 0.5 gL^{-1}. NaOH (Sigma Aldrich, 99%) was used to increase the pH to 14 (11.0 g L^{-1}). Na_2SO_3 (Sigma Aldrich, 98%) was used as hole scavenger, with a concentration of 1.7 g L^{-1}. The gas phase was analyzed by gas chromatography (Agilent, mod. 7890). Liquid phase was analyzed by HPLC (Agilent, 1220 Infinity) using a column (Alltech, OA-10308) with UV and refractive index (Agilent, 1260 Infinity) detectors. Aqueous H_3PO_4 solution (0.1 wt.%) was used as the eluent. The consumption of Na_2SO_3 was evaluated by iodometric titration. This method is based on the oxidation of sulphites (SO_3^{2-}) into sulphates (SO_4^{2-}) by iodine produced from a solution with a known concentration of potassium iodate (KIO_3, Sigma Aldrich, 98%) and potassium iodide (KI, Sigma Aldrich, 99%) in acid environment and the subsequent titration of the iodine excess with sodium thiosulphate ($Na_2S_2O_3$, Sigma Aldrich, 98%), the end point of the titration was detected using starch solution as an indicator.

Photoreactor Setup - Photocatalytic reduction of CO_2 with H_2O was carried out at a constant pressure of 7 bar and at a constant temperature of 80 °C. A scheme of the experimental setup is reported in Figure 4.1. It is an innovative pressurized batch photo reactor. It allows to up to 20 bar of CO_2, regulated by a pressure reducer. The reactor is made of AISI 316 stainless with an internal capacity of 1.7 L; a magnetic stirrer is located at the bottom ensuring a proper liquid mixing, and the temperature is kept constant through a double-walled thermostatic system. As source of radiation, we used a 125 W medium-pressure Hg vapor lamp with a range of emission wavelengths from 254 nm to 364 nm, which was introduced vertically in the reactor axis. The emitted power was periodically measured by means of a photoradiometer and corresponded to 0.5 W m^{-2} in the middle and 104.2 W m^{-2} in the lower part. A pressure transducer and a thermocouple measured the pressure and the temperature inside the reactor respectively. At the end of each test, liquid and gas phase were sampled. A 27 cm long quartz candle, transparent to the UV radiation, was used to protect the lamp from the pressure. The harmful overheat of the lamp bulb was avoided by continuous heat removal by an air circulation system around the bulb, which also helped keeping the temperature of the solution constant within ± 0.5 °C. The thermocouple was in the central part of the quartz candle at a distance of 1 cm.

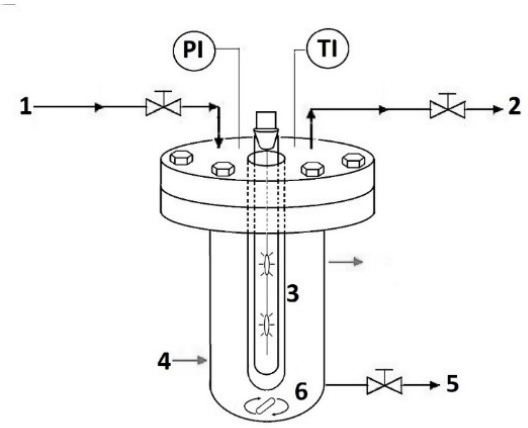

Figure 4.1. Sketch of the High Pressure Photoreactor. 1: Pressure Reducer, 2: Sample Valve for Gas Phase, 3: Lamp, 4: Double-walled Thermostatic System, 5: Sample Valve for Liquid Phase, 6: Magnetic Stirrer. PI: Pressure Indicator; TI: Temperature Indicator.

The photoreactor was filled with 1.2 L of solution, in a slurry configuration (catalyst suspended in the reaction solvent). Before starting the irradiation of the reaction mixture the system was outgassed at constant CO_2 flow of 15 mL min^{-1} at a pressure of 13 bar with the aim to eliminate air form the reactor head space. Then, in order to saturate water with CO_2, a static pressure of 7 bar of CO_2 was applied overnight. Tests were performed, predominantly exploring the effect of reaction time, pH and catalyst mass. The operating parameters of each test are summarized in Table 4.1.

Table 1: Summary of the Tests Performed

Test	*Time [h]*	*pH*	*Catalyst Mass [g]*
1	70	14	0.6
2	24	14	0.6
3	16	14	0.6
4	6	14	0.6
5	3	14	0.6
6	24	14	0.3
7	24	7	0.6

The amount of hole scavenger (sodium sulphite, 2.0 g) was kept constant, together with the temperature (80°C) and the CO_2 gas pressure (7 bar). These conditions were deeply explored in other previous theses and correspond to a good compromise between productivity in gas and liquid phase products [261,265]. Test 7 was carried out at a neutral pH value in order to understand the influence of this parameter on the product distribution and hydrogen productivity. The results were expressed either as total amount (mol) or as productivity (mmol/h kg_{cat}, which is equivalent to μmol/h g_{cat}). In the latter case the total amount of product was normalised by catalyst mass and by total irradiation time.

Results and discussion - Experimental results concerning tests 1-5 with details on liquid phase products and the concentration of Na_2SO_3 are reported in Figures 4.2 and 4.3 respectively.

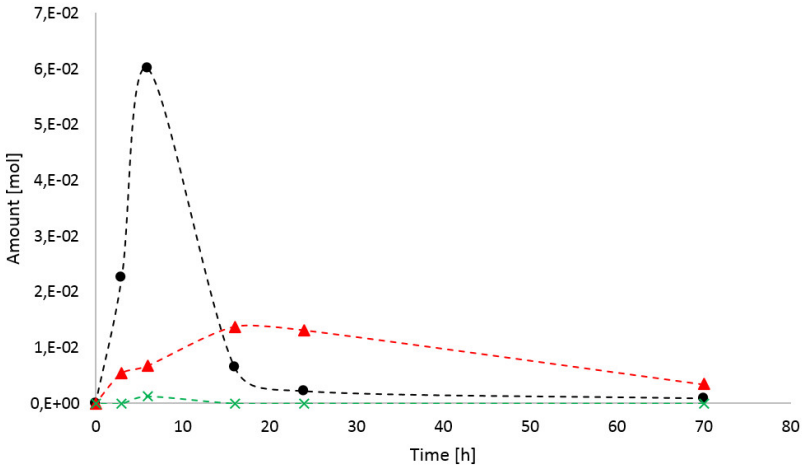

Figure 4.1. Amount of Liquid Phase Products, i.e. Formic Acid (▲), Formaldehyde (●) and Methanol (X), Obtained in Tests 1-5.

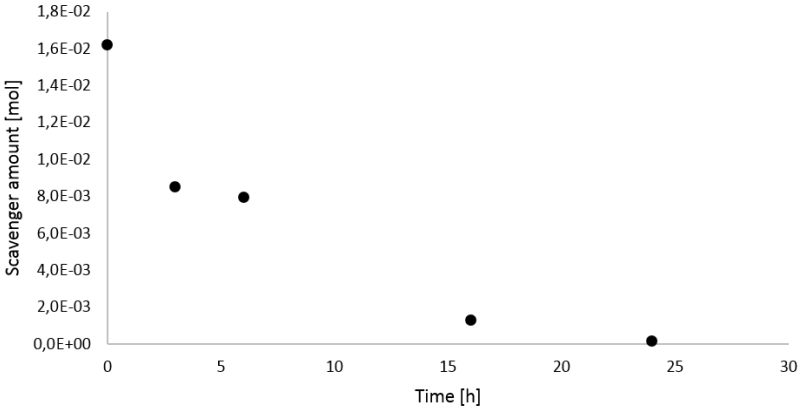

Figure 4.2. Amount of Scavenger at the End of Tests 1-5

Both formic acid and formaldehyde were detected, while only traces of methanol formed. As previously discussed in the introduction section, the mechanism of the CO_2 photoreduction has been previously studied and may lead to a broad spectrum of products depending on photocatalyst formulation and reaction conditions, as a result of many parallel and consecutive reaction steps. A strictly consecutive path were assumed at first (Scheme 4.1).

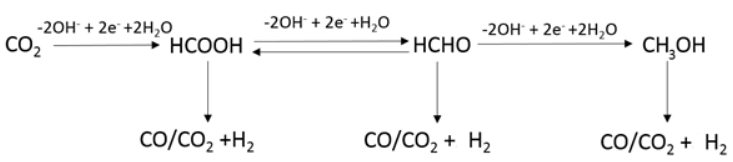

Scheme 4.1. Consecutive Pathway for CO_2 Photoreduction

According to this scheme, we would expect concentration maxima at increasing reaction time in the order: formic acid, formaldehyde and methanol. Gas phase product should start forming after accumulation of significant amounts of organic products in liquid phase through a photoreforming consecutive step. However, the higher formation rate of formaldehyde at the beginning of the reaction cannot be explained based on this mechanism.

The present reactions were operated at a basic pH, thus in the presence of dissolved CO_2 and carbonate anions. Chandrasekaran et al. [266] demonstrated that the direct reduction of carbonate to formaldehyde could be achieved, without the formation of formic acid. Compared to that reference, in which a 150 W Xe lamp was used, we obtained a maximum concentration of formaldehyde three orders of magnitude higher, which allowed us to obtain also a detectable amount of methanol, although minor with respect to the other intermediate products.

We therefore interpret our experimental results on the basis of the coexistence of a parallel reaction mechanism, involving in one branch the reduction of molecular carbon dioxide to formic acid, which may further evolve to gas phase products, and in the second branch the reduction of carbonates to give formaldehyde and possibly methanol in a further consecutive step, as shown in Scheme 4.2.

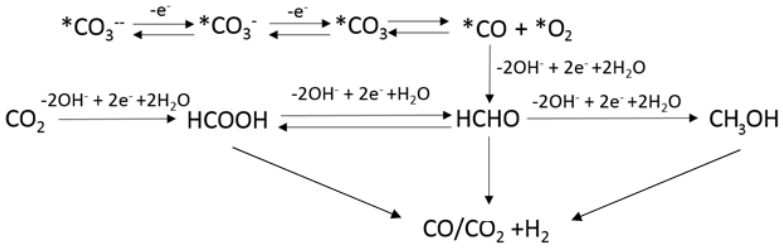

Scheme 4.2. Parallel Pathways for Molecular CO_2 and Carbonate Photoreduction. * indicate the species adsorbed on the photocatalyst surface

More in detail, the existence of consecutive reduction reactions can be assumed, because the presence of hydroxyl anions is not negligible at the catalyst surface, due to the high pH of the solution. The presence of the possible back-oxidation reaction was in accordance with Ao et al. [267].

The photoreduction of CO_2 had negligible rate in the absence of a hole scavenger. Indeed, if the consumption of conduction band electrons is not efficiently accompanied by holes reduction through electron donating species, the reaction is depressed. In this work we selected sodium sulphite as hole scavenger, being an inorganic, not competing species, which demonstrated very active in our previous screening. Figure 4.3 reports that the hole scavenger concentration decreased steadily during time and in about 24 hours all the Na_2SO_3 was consumed. Indeed, the concentration of scavenger measured in test 1, i.e. after 70 h of reaction, was zero. At the same time, liquid phase products concentration

decreased. In particular, formaldehyde was rapidly converted, formic acid slowly decreased its concentration and gas phase products started forming. Gas phase production expressed as moles of hydrogen and carbon monoxide versus time for tests 1-5 are reported in Figure 4.4.

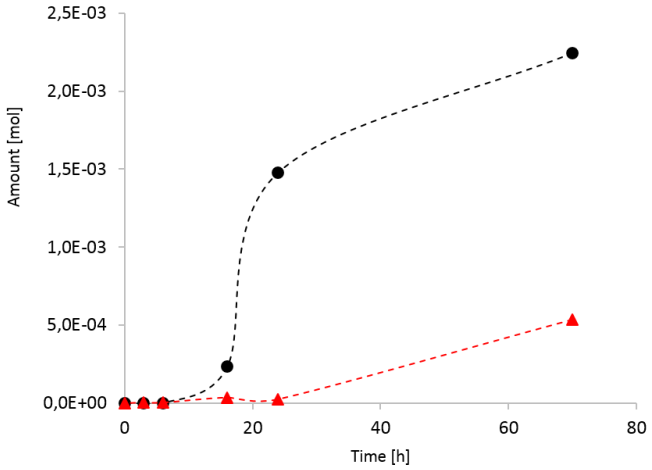

Figure 3.4. Gas Phase Products, i.e. CO (▲) and H_2 (●) Amount Obtained in Tests 1-5.

Gas phase products were detected only after 16 h of reaction, and then steadily increased with reaction time. This observation confirms the consecutive reaction step previously proposed, in particular, the evolution of hydrogen was attributed to the degradation of formic acid (see Scheme 4.2) because, comparing Figure 4.2 and 4.4, the inflection point of the hydrogen formation curve (maximum formation rate) correspond to the maximum peak of formic acid concentration. It should be noticed that photoreforming may also occur with formaldehyde, but the main reaction product after the consumption of the inorganic hole scavenger was formic acid in this case. Therefore, when the inorganic hole scavenger is finally consumed, the oxidation of sacrificial organic species starts. The latter reaction is indeed much more efficient than water oxidation.

The highest amount of hydrogen was obtained after 70 h reaction time, corresponding to a specific productivity of 57.1 mmol h^{-1} kg_{cat}^{-1}. Specific productivities were calculated by dividing the cumulative amount of each species by the catalyst mass and total irradiation time up to the sampling moment (including any induction period). Differently from literature [268,269], no methane was detected in the gas phase. This is reasonable according to literature data on band edge position and potentials of the redox couples involved in the reaction. The reaction involved in the CO and CH_4 generation are the following [270]:

$CO_2 + 2H^+ + 2e^- \rightarrow CO + H_2O$ $\quad E^0 = -0.53V$ (NHE, pH=7)

$CO_2 + 8H^+ + 8e^- \rightarrow CH_4 + 2H_2O$ $\quad E^0 = -0.24V$ (NHE, pH=7)

The potential level of the conduction band of TiO_2 is more negative (E^0= -0.56V vs. NHE, pH=7) [271], therefore both reactions are feasible under UV irradiation. However, the formation of CH_4 requires 8 electrons, compared with the 2 electrons of CO formation. Therefore the formation of CO is favored in the case of a bare semiconductor as in the present case and was confirmed by literature reports [270,272]. Moreover CO may be the precursor for CH_4 generation following an alternative hydrogenation pathway [273]. Furthermore, CH_4 formation was reported for Au-loaded samples, whereas reduction to formic acid was the only reaction path connected with undoped TiO_2 according to different authors [261,265].

A very interesting point is that the photoreforming reaction to gas phase products did not start only after accumulation of organic compounds in liquid phase, but also after exhaustion of the inorganic hole scavenger. Thus, after almost complete conversion of Na_2SO_3 was accomplished, H_2 evolution started. This confirms the hole scavenging role of the organic compounds in liquid phase.
A comparison between the produced amount of hydrogen, carbon monoxide, formaldehyde and formic acid are reported for test 7 and 2, *i.e.* under the same operating conditions for 24 h but at different initial pH (Figure 4.5).

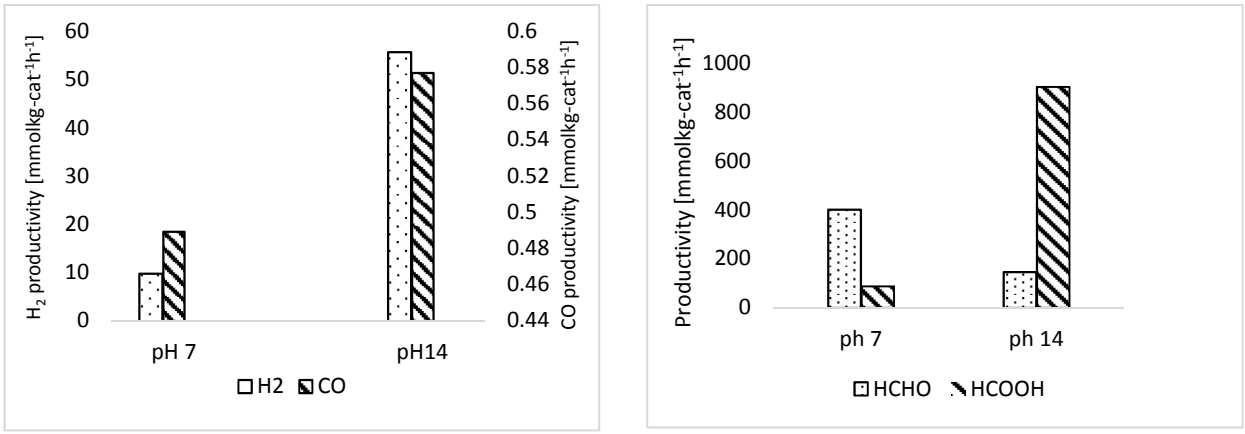

Figure 4.5. Productivity of Gas (a) and Liquid (b) Products as a Function of pH.

The measured initial pH was 14, ending at 9. We worked in most tests at basic pH to raise the solubility of CO_2 in the aqueous medium in the form of carbonates and to enhance the formation $^{\bullet}OH$ species [274]. However, the drawback of working at high pH is the conversion of CO_2 into CO_3^- or HCO_3^- that are harsher to reduce than CO_2 itself [275]. At pH = 14, an increased CO_2 solubility in the liquid phase is obtained in form of carbonate ions, and thus higher gas and liquid phase products concentration was obtained. However, considering the results at neutral pH (test 7), a different product distribution is obtained compared to the one of test 2. In particular, in liquid phase, a higher amount of formaldehyde was detected, while in test 2 higher concentration of formic acid than

formaldehyde was obtained after 24 h. This is probably due to the different carbonate concentration, which decrease significantly at neutral pH, making the reaction mechanism depicted in Scheme 1 predominant with respect to Scheme 4.2. Moreover, considering Scheme 4.2, the amount of hydroxyl anions is greatly reduced from pH 14 to pH 7, and thus the back oxidation of formaldehyde to formic acid is inhibited.

Finally, the results concerning the productivity of liquid and gas phase products is reported for test 2 and 6 in Table 4.2, carried out with different catalyst amounts. The catalyst concentration combined with the mixing conditions adopted assured the negligibility of mass transport limitations [276,277].

Table 4.2. Experimental Results Expressed as Gaseous and Liquid Productivity Changing Catalyst Amount

Test	*Catalyst concentration [g L^{-1}]*	*Productivity [mmol h^{-1} kg_{cat}^{-1}]*				
		H_2	***CO***	***HCOOH***	***HCHO***	***CH_3OH***
1	0.5	54.24	12.81	58.97	80.94	0
2	0.5	102.56	1.69	902.58	145.98	0
3	0.5	23.71	3.59	655.63	1411.38	0
4	0.5	0.00	0.72	1859.31	16537.13	350.98
5	0.5	0.00	0.91	2954.37	12350.14	0
6	0.25	98.21	8.85	1784.64	0	0

For gas phase products distribution, the increase of CO concentration and the slight decrease of the H_2 can be attributed to the less effective photoreforming activity. This leads to incomplete oxidation of the substrate back to CO_2, leaving a greater amount of CO and limiting slightly the H_2 productivity. Accordingly, formic acid was the only product of reaction in liquid phase using the lower amount of catalyst (test 6).

Conclusion - The photoreduction of CO_2 has been explored under unconventional reaction conditions og high pressure using bare TiO_2 P25. Considering products distribution vs. reaction time, the formaldehyde formation was unexpectedly independently from formic acid, being the major product at the beginning of the reaction. Two parallel pathways were hypothesised for the formation of the aldehyde and the acid, the former active when CO_2 is chemically dissolved as carbonate, the other involving the physical dissolution in molecular form.

Sulphite confirmed its role as inorganic hole scavenger. When it was completely converted, the oxidation of organic compounds accumulating in the reactor started. This allows confirming that gas phase products (CO and H_2) form through a consecutive mechanism by photoreforming of the formaldehyde and formic acid produced by CO_2 photoreduction.

4.1.2. High pressure tests using Au/TiO_2

Effect of gold-loading - Au/TiO_2 photocatalysts were prepared as detailed in Chapter 3. DRIFTS analysis, XPS, HRTEM and STEM were carried out and reported in Chapter 3. Testing were carried out at neutral pH, which is more interesting from an applicative point of view. The results of activity testing at 7 bar, 80°C, 24 h reaction time, with Au/TiO_2 P25 at variable metal loading are reported in Figure 4.6.

Methanol was the main product in liquid phase, demonstrating the higher reactivity of the present Au-doped samples with respect to the bare semiconductor. By looking to the relative products amounts, the intermediate concentration of formaldehyde confirms the validity of the reaction Scheme 2.1, where formaldehyde is formed through carbonates photoreduction and it can be further reduced to methanol or oxidized to formic acid. The highest methanol productivity was achieved with Au loading 0.2 and 0.5 wt.%, with a slightly higher yield of the less desirable products (formic acid and formaldehyde) for Au 0.2 wt.%.

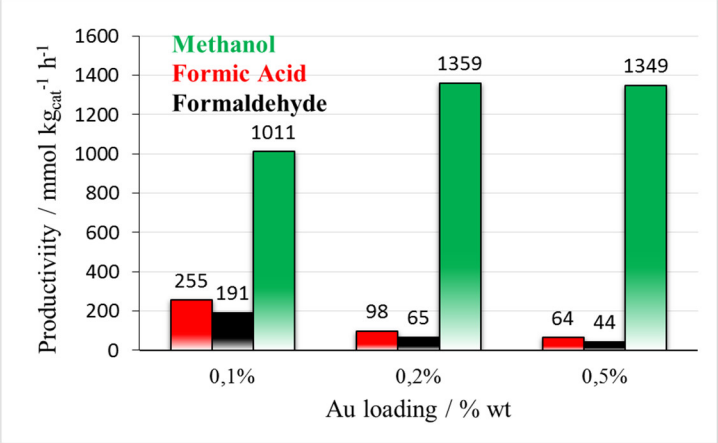

Figure 4.6. Liquid phase productivities changing the Au loading (T=80 °C, p=7 bar, pH=7).

A rough comparison of the present methanol productivity with respect to literature data is reported in the following Table 4.3. Of course, this comparison cannot take into account the reactor configuration, the distribution of the radiation and of the suspended particles, issues very important but difficult to evaluate if there are not specific fluid dynamic models of the photo-reactor used. Nevertheless, the good high methanol productivity achieved when testing the present Au-doped catalysts under high CO_2 pressure is well evident.

Table 4.2. Comparison of Au/TiO_2 catalysts synthetized and tested for CO_2 photoreduction processes.

Catalyst	*UV Power*	*UV λ*	*Methanol prod. (mmol kg_{cat}^{-1} h^{-1})*	*Reference*
0.5% Au/TiO_2	77 W m^{-2}	254-365 nm	1456	This work
1% Cu-3%In_2O_3/TiO_2	250 W m^{-2}	365 nm	35	[278]
Cu/TiO_2	8 W	254 nm	20	[279]
Ti-β zeolite	-	254-365 nm	680	[155]
Cu/TiO_2/MS	250W	365 nm	2	[280]
NiO	960 W m^{-2}	340 nm	393	[281]

The samples were conveniently active also for the formation of gas phase products, *i.e.* H_2, CO and methane. Methane is produced by direct photoreduction of CO_2. As exposed in Chapter 4.1.1, it was not observed for bare titania photocatalysts, whereas Au doping allowed its formation. The productivity of methane increased abruptly when doubling the Au amount from 0.1 to 0.2 wt.%, then very slightly when passing to 0.5 wt.%. This can be correlated to the dispersion of Au and confirms the role of the surface area of the exposed Au nanoparticles on this reaction pathway. CO can be either obtained by *i)* as a product of direct photoreduction, or *ii)* as a product of photoreforming of the organic compounds obtained in liquid phase by CO_2 photoreduction, or even *iii)* by catalytic reduction of CO_2 by using the photogenerated H_2. The productivity trend of CO and H_2 are well visible in Figure 4.7. This suggests that both species are produced by photoreforming of the primary organic products of photoreduction.

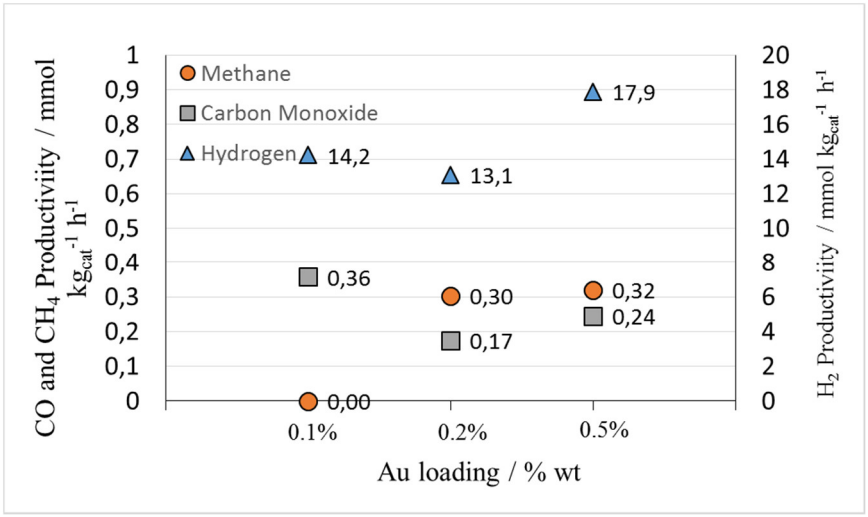

Figure 4.7. Gas phase productivities changing the Au loading (T=80 °C, p=7 bar, pH=7)

A methane productivity of 0.30 and 0.32 mmol kg_{cat}^{-1} h^{-1} was obtained for 0.2 and 0.5%Au/TiO_2-P25 respectively. By contrast, no traces were detected in gas effluents after tests using bare P25 and 0.1%Au/TiO_2-P25. This critical point must be discussed due to the implications associated.

Collado et al. performed several CO_2-photoreduction tests using a gas-phase configuration and gold/titania catalysts prepared by DP method using NaOH [282]. The highest CH_4 production was obtained with 1.0% Au/TiO_2-anatase sample at a maximum rate of *ca*. 8.86 mmol $kgcat^{-1}$ h^{-1}, using as UV illumination with a maximum wavelength at 365 nm and an average intensity of 71.7 W m^{-2}. Hydrogen productivity was maximum 9.5 mmol $kgcat^{-1}$ h^{-1}, and was attributed to the competitive reaction of H_2O reduction by photo-generated electrons. Although only the anatase crystalline form was investigated, a stronger enhancement of carbon monoxide productivity was obtained decreasing the metal loading, combined with a decrease of methane selectivity.

Matejová and co-workers studied several gold-oxide photocatalysts, obtaining a maximum hydrogen and methane productivity at 160 and 6 mmol kg_{cat}^{-1} h^{-1} respectively [283], but no liquid phase product was reported.

The highest loaded sample revealed the highest methane and hydrogen productivity. Thus, it can be considered the most promising among this series, although leading to a slightly lower formation of liquid products (1456 mmol h^{-1} kg_{cat}^{-1}) with respect to sample 0.2 wt.% Au (1522 mmol h^{-1} kg_{cat}^{-1}). The increase of metal loading in the present case showed beneficial, although a possible drawback could be the inhibition of substrate adsorption by gold nanoparticles. In the case of carbon dioxide and the products involved in its photoreduction this aspect seems irrelevant, if compared with other photoreacting systems where reactants and products are more sterically hindered (e.g. the photo-oxidation of azo-dyes [284]). The good performance of very low gold loading on titania was confirmed recently by Tahir et al. [285]. In particular, they investigated the incorporation of gold nanoparticles at low loading within TiO_2 nanowires as suitable materials for the CO_2 photoreduction in gas-phase under visible light. The optimum loading of Au for methane productivity was obtained using the 0.5 wt.%, However lower activity revealed the analogues 0.2 wt.% and 0.7 wt.%.

Effect of the Titania Polymorph Phase - The crystal phase of the titania photocatalyst was also varied. This aspect is important because many papers are available on the effect of titania polymorphs in the oxidative photocatalytic applications, but only few for the reductive photocatalysis. The highest metal loading was chosen (0.5 wt.% rather than 0.2) for all the samples because of the slightly enhanced total productivity and due to the much stronger plasmonic band associated. We believe this latter point can be of major interest for next process implementation using visible radiation under high pressure, in order to improve visible light harvesting.

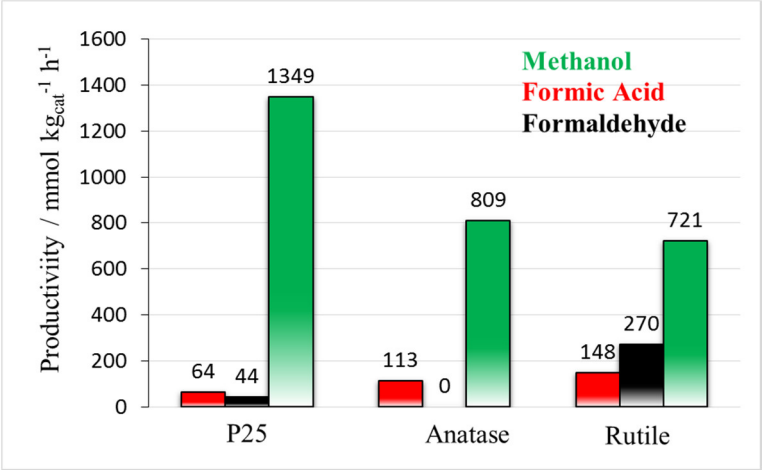

Figure 4.8. Liquid phase productivities changing the titania cristalline phase (T=80°C, p=7bar, pH=7)

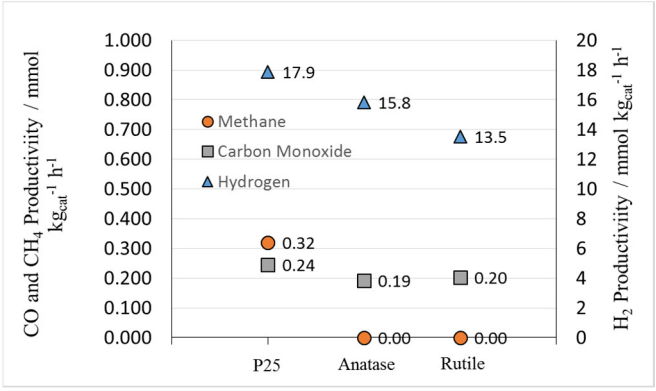

Figure 4.9. Gas phase productivities changing the titania cristalline phase

In particular, the commercial Degussa (Evonik) P25 was used as mixed oxide titania phase, while pure anatase and rutile as single titania phase supports.

Methanol productivity (Figure 4.8) was very high for all the samples and promising with respect to the most representative papers reported in literature (Table 2). Much higher methanol productivity was achieved for the P25-based sample, at the expenses of the more oxidized intermediates. On the

other hand, the complete absence of formaldehyde for the anatase-based sample and its highest productivity for the rutile base sample suggests the promotion of the carbonate-based reaction path by rutile. This hypothesis is supported by the low productivity of formaldehyde for P25, which is a mixture ca. 80:20 of anatase and rutile.

Methane was obtained only for the mixed phase P25 sample. The direct photoreduction of CO_2 to methane is indeed a complex multielectronic pathway. The greatest activity usually exhibited by the titania mixed phase is ascribed to the electron transfer from one phase to the other, which acts as electron sink, thus inhibiting the electron-hole recombination. Therefore, only by increasing the lifetime of the photogenerated electron the direct CO_2 photoreduction can safely proceed to methane. Also the photocatalytic activity towards H_2 and CO production was higher in the case of the P25 mixed phase than for the pure anatase and rutile phases. As highlighted before, their productivity trend was similar, confirming their origin from the photoreforming of organic compounds rather than by direct reduction.

Delavari et al. explored the gas phase reaction using immobilized TiO_2 nanoparticles on a stainless steel mesh [286]. Considering the crystalline phase, an increase of CO_2 and CH_4 conversions were detected due to the increase of the anatase/rutile ratio in TiO_2, in such a case directly correlated with the enhancement of surface area. A detailed Langmuir-Hinshelwood model was applied to the experimental results, but no considerations about the crystalline form and the direct consequences on CO_2 reduction were advanced by the authors. Furthermore, the co-feeding of methane with CO_2 did not allow to study the effect on methane formation.

Mixed-phase titania nanomaterials were studied by Chen et al., for gas phase CO_2 photoreduction involving the DC magneton sputtering as preparation method [287]. All the mixed-phase sputtered samples displayed greater extent of reaction compared to single phase ones. The results explanation was correlated to the high density of interfacial sites.

The synergistic effect between rutile and anatase for photo-catalytic applications is not new in the literature, but the deep explanation of the phenomena is still under debate [264]. The more consistent argumentation consider the low electron-hole recombination as consequence of the spatial separation caused by the interconnection between rutile and anatase particles. Li et al. investigated several TiO_2 polymorphs as a photo-catalyst for CO_2 reduction under UV light illumination [288]. They found a very different methane production varying the crystalline phase of the titania. The synergistic effect was apparently demonstrated because higher photocatalytic activity was obtained using a mixed-phase TiO_2 nanocomposite prepared by a low-temperature hydrothermal method (SSA=8.6 $m^2\ g^{-1}$) with respect to commercial P25 (SSA~50 $m^2\ g^{-1}$) followed by commercial anatase. On the contrary,

Ohtani et al. supported a contrasting explanation, considering the lack of information about the direct evidence of the inter-particle charge migrations and the expected lower level of activity of pure anatase or rutile particles alone [264]. For this reason in another work [289] they prepared a reconstructed P25 (mixture of pure anatase, rutile and amorphous titania) and demonstrated a less probable synergistic effect for the oxidative decomposition of acetic acid, acetaldehyde and methanol dehydrogenation. However, no reductive photo-catalytic processes was considered in their results. Recently Kafizas et al. [290] employed transient absorption spectroscopy to study the hole transfer process across the anatase-rutile heterojunction in films as a function of phase composition, revealing a concrete difference between the electron hole recombination time using different titania forms. In addition Kullgren et al. [291] investigated the phenomena by photoelectron spectroscopy and flat-band potential measurements in the case of mixed-phase nanoparticles in humid environment. Although the explanation is still far from an unmistakable solution, the higher activity of mixed rutile-anatase TiO_2 was still reported for CO_2 photo-reduction in literature, and our results confirmed this trend also for the present unconventional high pressure conditions.

Similar CO selectivity was obtained for all the samples, ascribable to two main reasons: i) the CO formation occurred through a reaction independent and without any contribution of the photo-catalyst, such as the CO_2 photolysis; ii) the CO formation occurred independent from the metal loading; iii) photoreforming. The directly photolysis of CO_2 is the less probable option in our conditions. The CO_2 splitting occurs in the so called deep UV region (wavelengths below 200 nm requiring pure quartz or metal halides and vacuum):

$CO_2 + hv(<200nm) \rightarrow CO + 1/2\ O_2$ ($\Delta H = +257$ kJ mol^{-1}) [275]

A blank test without the catalyst revealed negligible CO productivity and ruled out definitely the first hypothesis. The independence on metal loading can be explained considering a detailed work of Lin et al. [292]. A direct correlation between Ti centers and CO_2 reduction to CO by water in presence of the UV irradiation was obtained using mesoporous framework substituted Ti silicalites. The proposed mechanism involved the formation of a transient Ti^{3+} and a hole on a framework oxygen (Ti^{+3}-O^{-}) after the excitation of the Ti centers (Ti^{4+}-O^{2-}). Thus, the effective role of Au, as electron sink is not useful in this context.

The hydroxylation of the surface, examining the characteristic Ti−OH bonds, changing the support was carried out in order to investigate this feature often correlated with the photo-activity of the catalysts [293]. Indeed, hydroxyl groups have been recognized to play an important role in the photo-catalytic processes through their interactions with photo-generated holes [294,295], and the preparation method directly affects the hydroxylation state of the catalyst surface. The experimental

DRIFTS spectra reported also in the present case the different OH species depending on the titania (Figure 4.10). Generally, hydroxyl groups can be divided in two main types considering the TiO_2 surface: isolated hydroxyls (3600-3700 cm^{-1}) and H-bonded hydroxyls (3400-3450 cm^{-1}) [294–296]. The peak at 3691 cm^{-1} relative to the stretching vibration of H-bound OH group was present for all the samples but in different intensity [295]. P25 revealed also a peak at 3629 cm^{-1} corresponding to physically adsorbed H_2O [297] while rutile a peak at 3410 cm^{-1} often ascribed to symmetric and antisymmetric OH modes of molecular water coordinated to Ti^{4+} cations [297]. All these hydroxyl species are more intensive in the case of P25, whilst decrease shifting to anatase and rutile. Although not a significant correlation can be found considering the liquid-phase product obtained by the photoreduction process, the results are in line with the hydrogen productivity obtained as graphed in Figure 4.11. This is in accordance with Maira et al. that reported the correlation between isolated hydroxyl groups and adsorption/photooxidation activity [295].

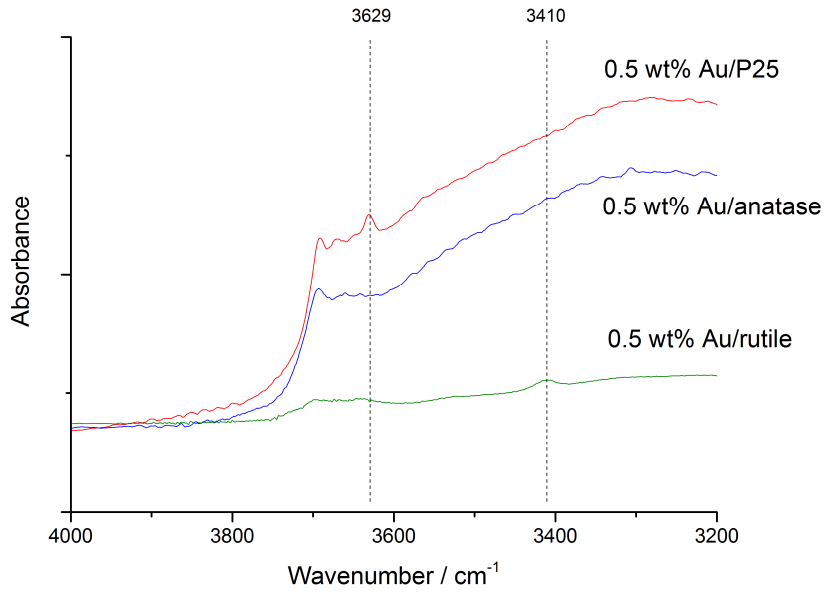

Figure 4.10. DRIFTS spectra of OH groups in the region of 3200−4000 cm^{-1} for the different titania samples.

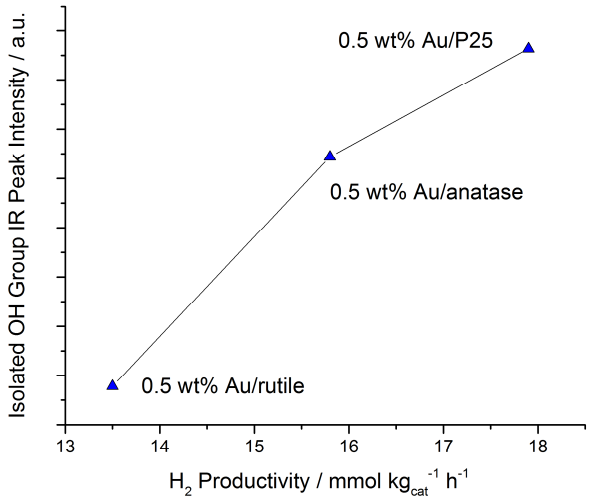

Figure 4.11. H_2 productivities versus OH peak intensities for the different titania samples.

In order to compare the reactivity towards hydrogen production through direct water splitting and CO_2 photoreduction, a test at 7 bar of nitrogen was compared with the ones in CO_2 atmosphere. In presence of nitrogen the main use of the photo-generated electrons in the CB, besides recombination, is the reduction of H^+ to H_2. The test with nitrogen confirmed this result, with an unexpectedly high productivity of 134.6 mmol H_2 kg_{cat}^{-1} h^{-1} with respect to the 17.9 mmol H_2 kg_{cat}^{-1} h^{-1} obtained under CO_2 atmosphere. The fundamental role of the photocatalyst was finally confirmed by the blank test without any sample, where no hydrogen was detected.

Conclusion - The photocatalytic reduction of CO_2 in water was studied at high pressure, investigating the role of metal doping and TiO_2 crystalline phase. In particular, a modified deposition/precipitation method was adopted for the synthesis on 0.1 wt.%, 0.2 wt.% and 0.5 wt.% Au/TiO_2. Commercial P25, pure anatase and pure rutile were used. Methanol productivities of 1359 and 1349 mmol kg_{cat}^{-1} h^{-1} were detected for 0.2 wt.% Au/TiO_2 and 0.5 wt.% Au/TiO_2 respectively. However, the highest loaded sample revealed the highest H_2 and CH_4 productivities (17.9 and 0.32 mmol kg_{cat}^{-1} h^{-1}). By contrast, lower activity was obtained using anatase and rutile pure phases, confirming the key role of interfacial defects between borders of different crystalline phases.

5. NH_3 Production

Introduction – The hydrogen production in sustainable ways was deeply reported in Chapter 1. The use of "renewable hydrogen" for different processes can lead to the production of "sustainable compounds". In this perspective, ammonia is one the main compounds produced starting from hydrogen. The use of "renewable hydrogen" would lead to the production of "renewable ammonia". The ammonia synthesis is mainly accomplished through the well known Haber-Bosch process [298] on a plant scale of 1,000 ton/day (100 millions tons per year around the world). This technology represents the major success of heterogeneous catalytic process used on large scale [299,300].

Although the chemistry of ammonia synthesis is relatively well known, critical operating conditions of pressure (100-200 bar) and temperature (380-450°C) are used industrially. These are very demanding both from the economic and safety points of view. For this reason, the technology is very sophisticated and its study continued during the last century, both in the scientific and industrial communities. Iron based catalyst can be used at 120-220 bar and 380-520°C [301], they are sufficiently active and poorly expensive, but the maximum conversion achievable is limited by their inhibition by the product. Thus, high pressure is usually applied to achieve sufficiently high conversion. The research of new materials to decrease the operating pressure is still intriguing and debated in the literature [302–306], relying basically on the search of more active materials.

Ruthenium showed higher activity toward ammonia production, combined with a much greater tolerance under high ammonia partial pressure (it is not inhibited by the product). Although the Ru-based catalyst still has similar sensitivity to oxygen-containing impurities than Fe, and therefore requires similar feed gas purity than magnetite, it is less sensitive to permanent poisons such as sulphur [307]. The industrial application of ruthenium supported on graphitized carbon was achieved in the so called Kellogg's Advanced Ammonia Process (KAAP). This process is active in seven world-scale plants, each producing ca. 2,000 tonnes per day of ammonia [308]. The catalyst is doped with K and Ba promoters. This process couples the use of Ru and Fe catalysts in a single converter. In particular, the Ru catalyst is placed in different fixed beds (two or three) after an iron bed catalyst, so exploiting Ru better ability to resist toward catalyst inhibition by NH_3. Furthermore, the higher activity of Ru allows lower operating pressure. The main drawbacks of Ru/C catalysts are *i)* their inhibition by hydrogen, which advices the use of understoichiometric reaction conditions and *ii)* carbon resistance towards methanation, which is catalysed by Ru and may corrode the support and promote Ru sintering [309].

Aspen Plus© process simulator has been effectively used to investigate high pressure processes, such as methanol synthesis [107], coal gasification [311], biomass gasification [312], Fischer-Tropsch synthesis [313], partial oxidation of natural gas [314]. A basic requirement for a reliable simulation of reactive systems, is the availability of appropriate kinetic equations [315]. Surprisingly, only few authors tried to simulate the ammonia synthesis process implementing real kinetic expressions. Yu et al. tried to implement the kinetic parameters of ammonia synthesis for the evaluation of a coal-based polygeneration process to coproduce synthetic natural gas and ammonia [316]. Unfortunately, the authors did not detail how the kinetic parameters were implemented in the simulation, likely for the sake of conciseness due to the huge size of the work, which was a complete design and economic evaluation from air and coal to ammonia and electric energy production. Arora and co-workers investigated small scale ammonia production from biomass [317]. Gibbs and equilibrium reactors were used to model the ammonia converter, since the reactor was operated close to equilibrium and the model was validated against some plant data reported in literature. Ammonia production via integrated biomass gasification was also studied by Andersson and Lundgren [318]. Aspen Plus© was used to model energy and material balances for the complete biomass gasification system including the NH_3 synthesis. Also in this case the reactor was simulated using a Gibbs reactor, with operating condition 180 bar and 440°C, using a promoted iron catalyst.

A control structure design for the ammonia synthesis process was carried out by Araujo and Skogestad [319]. The reactor configuration was based on an industrial fixed-bed autothermal reactor. The reaction kinetics was described by the Temkin–Pyzhev expression and the beds were modelled in Aspen Plus© by means of its built-in catalytic plug-flow reactor. The evaluation of the effectiveness of a control structure against disturbance was carried out using the dynamic simulation tool.

The assumption concerning the use of a Gibbs reactor (RGibbs reactor block in Aspen Plus©) for the ammonia converter represents a critical point. This kind of reactor does not consider any reaction rate and the process is represented performing a complete equilibrium calculation based on the minimization of Gibbs free energy. Neglecting kinetics can also induce some fundamental mistake in the identification of suitable operating conditions, since for this reaction kinetic and thermodynamics obey to opposite requirements.

In this part of the PhD project, the simulation of a low pressure ammonia synthesis reactor was carried out. The kinetic description of the process is based on an original kinetic model, derived on purpose on a patented promoted Ru/C catalyst, obtained as a result of 20 years of research in the laboratories of Professor Ilenia Rossetti. The full details on catalyst properties and its performance under industrially relevant conditions can be found elsewhere [105,320,321]. Temperature lower than

500°C are suitable for carbon supported catalysts, preventing the methanation of the graphitised carbon used as support [54,105,322] . A detailed kinetic model was already developed, modifying the Temkin equation with the addition of H_2 and NH_3 adsorption terms, in order to consider their possible inhibiting effect on catalyst performance [322]. This model was adapted here for implementation in the Aspen Plus© process simulator. Finally, the sizing of the reactor was here carried out comparing the advantage of commercial catalyst with a home-made catalysts tested previously in out labs.

5.1. Kinetic implementation

Preparation of catalyst - Details about the preparation route of the support, catalyst and activation can be found in the related patent [301] and papers published elsewhere [322]. Briefly, a graphitised carbon was used as support and promoters were added by impregnation from aqueous solutions of hydroxides (K and Cs) or nitrates (Ba), in the previously optimized amount to obtain: Ba/Ru = 0.6 (mol/mol), Cs/Ru = 1 (mol/mol), and K/Ru = 3.5 (mol/mol). The Ru content, referred to the final catalyst weight, was 3.2 wt.%.

Experimental set up – As explained in the introduction, the catalytic activity has been determined in previous works. To better understand the catalytic data elaborated, a brief explanation of the catalytic apparatus is necessary. A continuous tubular reactor (9 mm internal diameter) was adopted, by feeding a reactant gas mixture consisting of hydrogen and nitrogen in different volumetric ratio (3:1 or 1.5:1 v/v), with different Gas Hourly Space Velocity (GHSV) through a catalyst bed of 0.15-0.25 mm particles. The GHSV was defined as the ratio of the inlet gas flow rate at standard conditions and the volume of the catalyst bed, $Nm_g^3\ m_{cat}^{-3}\ h^{-1}$. The catalyst was diluted with quartz of the same particle size in volumetric ratio catalyst/quartz = 1/22, to limit the hot spot across the bed. Before the run the catalyst was activated in situ in a flow of the same reactant gas mixture at 30 bar, 450° C, GHSV = 20000 h^{-1} for 5 h. Activity has been determined by evaluating the volumetric concentration of ammonia in the effluent gas, by bubbling it in an excess of sulphuric acid solution and back-titrating the excess acid with a standardized NaOH solution. The flowsheet of the microplant is reported in Figure 5.1.

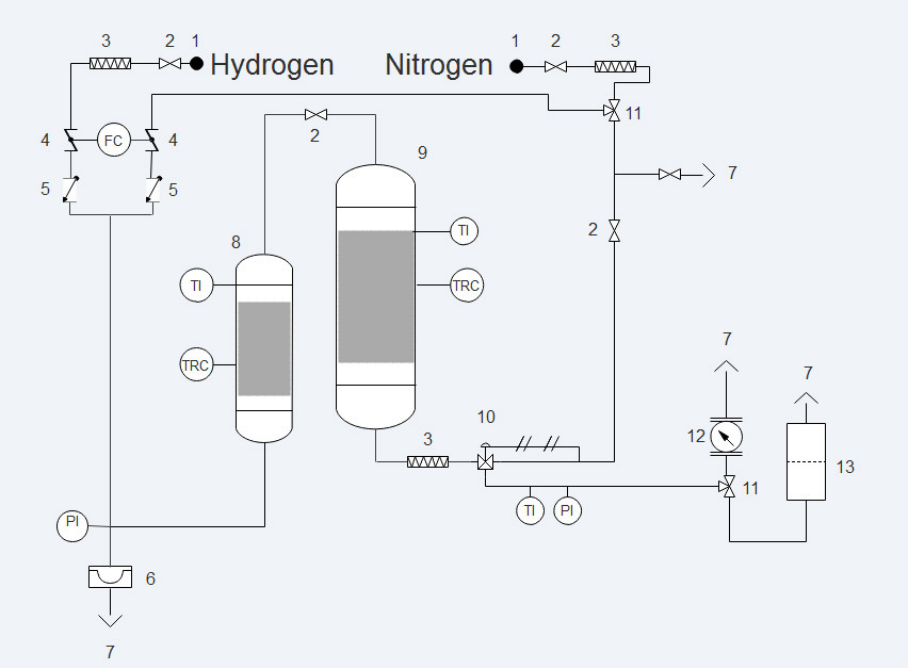

Figure 5.1. Scheme of the microplant adopted. 1) Inlet gas from cylinder; 2) Shut off globe valve; 3) Filter (2 μm); 4) MSK mass flowmeter; 5) Check valve; 6) Bursting disc; 7) Vent; 8) Chemical trap containing iron commercial catalyst coupled with electric oven; 9) Reactor coupled with electric oven; 10) PTFE-membrane relief valve; 11) Three-way valve; 12) Bubble flowmeter; 13) Chemical absorption (H_2SO_4)

Kinetic Model implementation - The ammonia synthesis process follows the ideal stoichiometry reported in Eq 1.

$N_2 + 3\ H_2 \leftrightarrows 2\ NH_3$ $\Delta H^0 = -46\ kJ\ mol^{-1}$ [308] (Eq.1)

However, the reaction proceeds through several adsorption and dissociation steps [323]. The kinetic parameters related are complex functions of the coverage and of the surface structure. A Langmuir–Hinshelwood–Hougen–Watson (LHHW) model was used in our approach. Aspen Plus© provides a built-in LHHW kinetics for calculating the rate of the reaction. This kinetic model consists of a kinetic factor, a driving force expression and an adsorption term (Eq. 2).

$$r = \frac{(\text{kinetic factor})(\text{driving force})}{\text{adsorption term}} \qquad \text{(Eq. 2)}$$

The reaction occurs in the vapor phase and the reaction rate is based on catalyst weight. The concentration basis for the driving force is fugacity powered by the concentration exponents for forward and backward reactions (terms 1 and 2, respectively). In a previous work, a detailed kinetic analysis on the promoted Ru/C prepared by impregnation has been developed [105]. The rate equation obtained is reported in Eq. 3.

$$\frac{d\eta}{d\tau} = k_f \lambda(q) \frac{(a_{N2})^{0.5}\left[\frac{(a_{H2})^{0.375}}{(a_{NH3})^{0.25}}\right] - \frac{1}{K_a}\left[\frac{(a_{NH3})^{0.75}}{(a_{H2})^{1.125}}\right]}{1+K_{H2}(a_{H2})^{0.3}+K_{NH3}(a_{NH3})^{0.2}} \qquad \text{(Eq. 3)}$$

Where $d\eta/d\tau$ represented the rate of consumption of the defective reactant in mol h^{-1} dm^{-3}_{cat}, k_f was the kinetic constant of the direct reaction, K_a the equilibrium constant of the reaction and a_i the activities of reactants and product. $\lambda(q)$ was a stoichiometric parameter set to 1 or 1.2 when the H_2/N_2 feeding ratio was 3 or 1.5 respectively. The consistency of the optimized parameters was checked by the Arrhenius and Van't Hoff equations, leading to the values reported in Table 5.1. In order to implement the data in Aspen Plus©, the pre-exponential factor was corrected considering the experimental catalyst density equal to 0.59 g cm^{-3}. In this way, the rate of reaction was expressed in mol h^{-1} g^{-1}_{cat}. The pre-exponential factor (A) in the LHHW rate expression has the units needed to match an overall rate expression in kmol s^{-1} kg_{cat}^{-1}. The equilibrium constant was originally calculated according to Gillespie and Beattie as reported elsewhere [322,324,325]. The quadratic term reported in Eq. 4 [322,324,325] was neglected according to Aspen Plus© format for the temperature dependence of equilibrium constants. Proper conversions from $\log_{10}$ to $\log_e$ and from bar to Pa were performed.

$$\log_{10} K_{H2} = -\frac{59.9024}{R} + \frac{37656}{RT} - 2.691122 * \log_{10} T - 5.519265 * 10^{-5} T + 1.848863 * 10^{-7} T^2 \qquad \text{(Eq. 4)}$$

Adsorption equilibrium constants were obtained considering the ΔH_{ads} and ΔS_{ads} for H_2 and NH_3 and the expressions are reported in Eq. 5 and 6.

$$\log_e K_{H2} = -\frac{56.9024}{R} + \frac{37656}{RT} \qquad \text{(Eq. 5)}$$

$$\log_e K_{NH3} = -\frac{34.7272}{R} + \frac{29228}{RT} \qquad \text{(Eq. 6)}$$

Overall, the kinetic equation was based on Temkin model, on purpose modified considering the features of Ru with respect to Fe. This point is crucial because, as already mentioned, Fe is kinetically inhibited by NH_3 adsorption, whilst Ru by H_2 due to its competitive adsorption with N_2. For this reason, in the denominator of the equation an adsorption term for hydrogen was added.

Table 5.1. Thermodynamic and kinetic parameters of promoted Ru/C catalyst (modified Temkin equation) implemented in process simulation using the Aspen Plus© software.

Kinetic parameters	
E_a (kcal mol^{-1})	23.0
A (kmol sec^{-1} kg^{-1}_{cat})	426
ΔH_{ads}, H_2 (J mol^{-1})	-37656
ΔH_{ads}, NH_3 (J mol^{-1})	-29228
ΔS_{ads}, H_2 (J K^{-1} mol^{-1})	-56.9024
ΔS_{ads}, NH_3 (J K^{-1} mol^{-1})	-34.7272
Driving force parameters	
Term 1	
conc. exponents for reactants	N_2 = 0.5; H_2 = 0.375
conc. exponents for products	NH_3 = -0.25
coefficients	A = -7.196 B = 0
Term 2	
conc. exponents for reactants	N_2 = 0; H_2 = -1.125
conc. exponents for products	NH_3 = 0.75
coefficients	A = -1.876376592; B= -4608.8; C = 2.691122; D = 0.000127
Adsorption parameters	
Term 1	
conc. exponents for reactants	N_2 =0; H_2 = 0
conc. exponents for products	NH_3 = 0
coefficients	A = B = C = D =0
Term 2	
conc. exponents for reactants	N_2 =0; H_2 = 0.3
conc. exponents for products	NH_3 = 0
coefficients	A = -10.29804411; B = 4529.227809; C=D=0
Term 3	
conc. exponents for reactants	N_2 =0; H_2 = 0
conc. exponents for products	NH_3 = 0.2
coefficients	A = -6.479539628; B = 3522.73274; C = D = 0

Table 5.1 gives a quick reference to the kinetic and adsorption parameters used during reactor simulation. In accordance with the kinetic expression, the Aspen LHHW reaction model was used for the kinetic implementation. The RPlug model was adopted in both isothermal and adiabatic conditions. The Peng-Robinson equation of state was adopted as thermodynamic model to compute the non-ideality of the gaseous mixture.

5.2. Results and discussion of the kinetic implementation

Validation of the kinetic model - The validation of the kinetic model was carried out using Aspen Plus© in order to check the computational consistency of the equation adopted. In general, a good agreement between the experimental and simulation results was obtained for a H_2/N_2 feeding ratio equal to 3, in the whole range of temperature, pressure and space velocity experimentally explored (50,000- 400,000 h^{-1}, 360-430 °C, 70-100 bar). Figure 5.1 exemplifies the results for the test at T = 430 °C, P = 70 bar and H_2/N_2 = 3 (v/v).

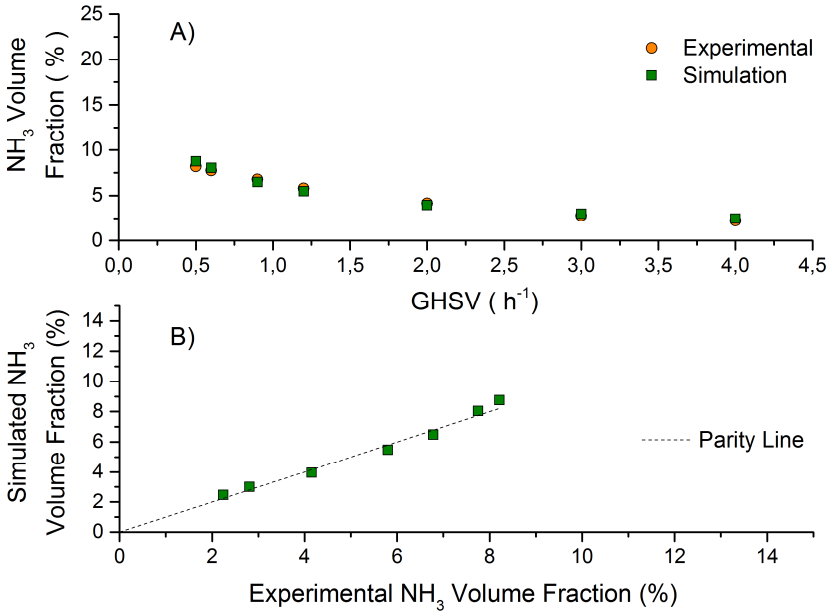

Figure 5.1. A) Example of data simulation for the test at T = 430°C, p = 70 bar and H_2/N_2 = 3 v/v. Experimental points (orange circles), simulated values (green squares). B) Parity plot for the outlet ammonia vol%.

For the tests with H_2/N_2 ratio equal to 1.5 (v/v) only the simulation at temperature below 430°C revealed a satisfactory agreement between the simulated ammonia fraction in the reactor outlet gas and the experimental values. In Figures 5.2 and 5.3 two examples considering the best and the worst cases are reported, respectively.

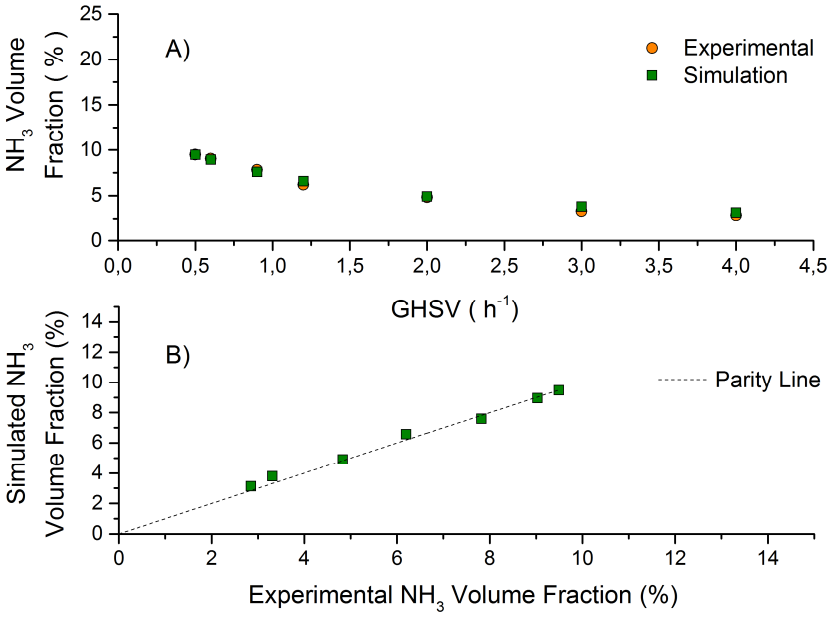

Figure 5.2. A) Example of data simulation for test at T = 430°C, P = 70 bar and H_2/N_2 = 1.5 (v/v). Experimental points (orange circles), simulated values (green squares). B) Parity plot.

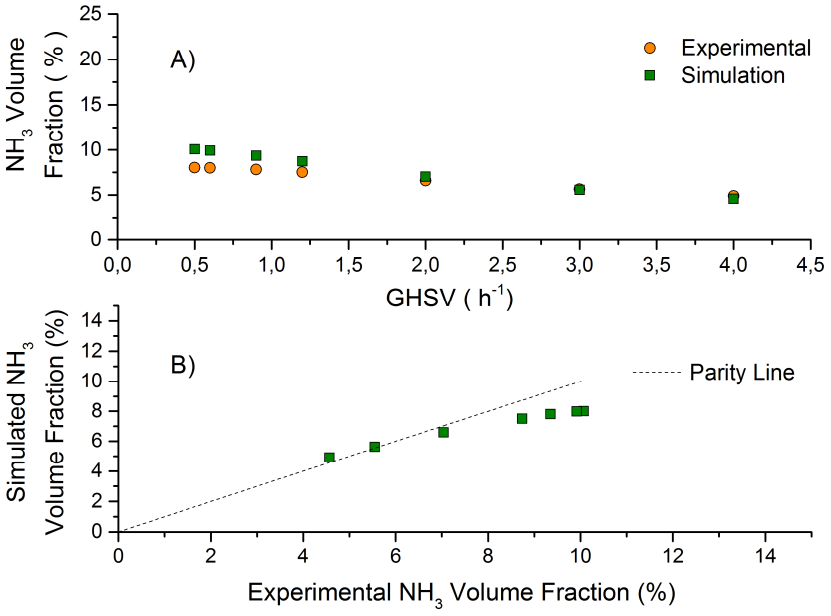

Figure 5.3. A) Example of data simulation for test at T = 460°C, P = 70 bar and H_2/N_2 = 1.5 (v/v). Experimental points (orange circles), simulated values (green squares). B) Parity plot.

The maximum discrepancy between the calculated and the experimental values were observed at the highest temperature and lowest space velocity (i.e. at highest contact time). This occurs for the most favorable understoichiometric feeding ratios. This means that the model is critical in reproducing the best performing catalyst conditions, i.e. the ones approaching the equilibrium conversion, but overall it gets the catalyst performance over a wide conditions range.

Space velocity and temperature effect - The production capacity of an ammonia synthesis reactor is directly affected by the space velocity. Increasing space velocity will normally decrease outlet ammonia concentration, but it increases total ammonia production flow rate. Examples of the relationship between activity and space velocity are shown in Figure 5.1-5.3. The decrease of ammonia concentration in the outlet stream leads to a decrease of ammonia in the recycle stream. Moreover, the outlet temperature of the converter was lower due to the decrease of the exothermic contribution of the reaction, and also the pressure drop, consequently decreasing in the recycle has to be taken into account.

Another point is the reduction of energy consumption for cooling the recycle gas. Generally, an economic optimum value of space velocity is calculated for every specified process according to the pressure of the system, the structure of reactor and energy costs. For a low-pressure ammonia synthesis loop, space velocity in the range of 5,000 –10,000 h^{-1} are commonly chosen, while 15,000–30,000 h^{-1} and ≥ 60,000 h^{-1} are common selected for middle and low-pressure systems, respectively, using traditional iron catalysts [326]. The use of a very active catalyst such as the catalyst adopted in this work can significantly reduce the contact time maintaining high ammonia yield. Therefore, a trade off with productivity has to be newly searched.

Figure 5.4 compares the ammonia production predicted by the kinetic model for low and high residence times (GHSV = $2.0*10^5$ h^{-1} and $0.5*10^5$ h^{-1}, respectively) with the predictions of the thermodynamic model calculated using the Equilibrium Reactor Model (REquil). This kind of reactor model available in the Aspen Plus© software is used, when the reaction stoichiometry is known, to evaluate the conversion at chemical equilibrium. The comparison was done for a range of reactor temperatures under isothermal conditions choosing the H_2/N_2 ratio equal to 1.5 (v/v). Ru catalyst, as aforementioned, is preferably operated at understoichiometric ratios because of the inhibition effect of H_2.

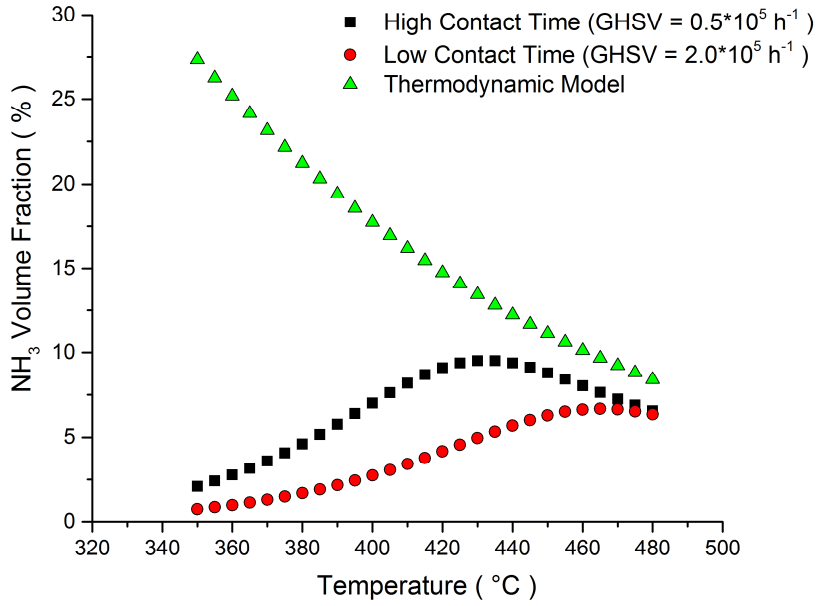

Figure 5.4. Comparison of ammonia production predicted by the here proposed kinetic model at low and high residence times (GHSV = $2.0*10^5$ h^{-1} and $0.5*10^5$ h^{-1}, respectively) and thermodynamic model under isothermal condition (P = 70bar, H_2/N_2 = 1.5 v/v).

The ammonia production increases as the reactor temperature increases, reaches a maximum at a temperature strictly depending on GHSV (430°C and 465°C for the high and low contact time, respectively) and then decreases with temperature following the equilibrium conversion. The reaction shows a transition from kinetic to an equilibrium regime of operation where the results from kinetic model match with those of the thermodynamic model. The increase of conversion before the maximum with temperature in the kinetic approach is attributed to the increase in the reaction rate while the following decrease is due to the approaching of the thermodynamic limit, unfavoured by increasing temperature due to the exothermicity of the reaction.

The design of a chemical reactor is a strictly logical process, but there are a multitude of different solutions for the same problem. The reaction is exothermal (ΔH^0 = -46 kJ mol^{-1}) [308] and the suitable configurations are the isothermal and the adiabatic ones. The first choice implies the direct heat exchange within the bed, ensuring the proper temperature at the inlet of the reactor and homogeneous thermal profile along the reactor length. This choice implies the use of multitubular reactor configuration to achieve optimal heat exchange. The second choice is usually more common for ammonia reactors. For this reason and in order to study the thermal profile through the reactor length, adiabatic conditions were here studied.

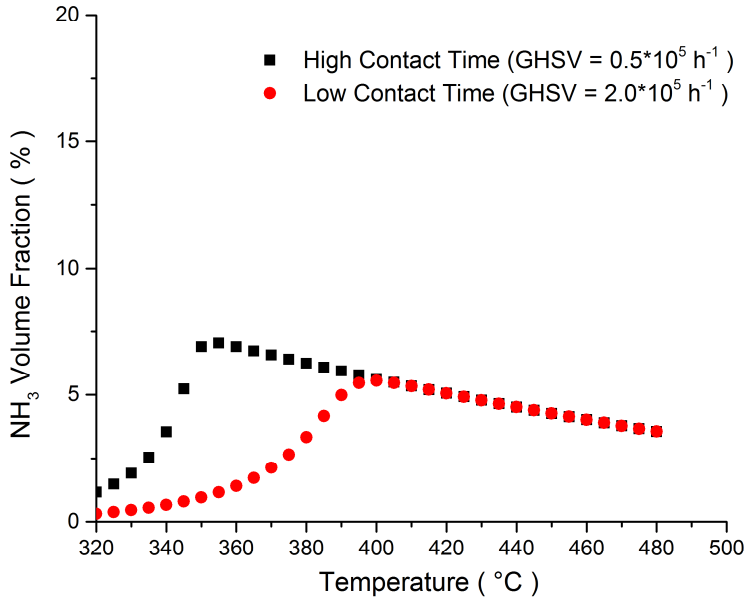

Figure 4.5. Comparison of ammonia production predicted by kinetic model at low and high residence times (GHSV = $2.0*10^5$ h^{-1} and $0.5*10^5$ h^{-1} respectively) and thermodynamic model under adiabatic condition (P = 70bar, H_2/N_2 = 1.5 v/v).

Ammonia volume fraction at the outlet of the reactor predicted by the kinetic model under adiabatic conditions is shown in Figure 4.5. The threshold temperatures at which the transition from kinetic to thermodynamic condition occurs, are 355 °C and 400°C for the high and low contact time respectively.

Influence of feed composition - The effect of the H_2/N_2 ratio on the activity of the novel Ru/C catalyst is shown in Figure 5.6. Temperature was set at 430°C. The proper adjusting of the kinetic expression varying the λ(q) was implemented. After the maximum conversion, where the thermodynamic regime governs the process, the ammonia production increases with the increase of the H_2/N_2 ratio as expected, because when all the hydrogen is reacted no ammonia formation can occur. On the other side, the opposite trend in the kinetic regime confirmed the consistency of the kinetic expression for ruthenium catalyst. Indeed, Ru is inhibited by H_2, and low H_2/N_2 ratios are more advantageous in terms of ammonia conversion with respect to the stoichiometric one. The kinetic expression considers the competitive adsorption between H_2 and N_2 on the Ru-based catalyst, modifying accordingly the classical Temkin equation. The adsorption term related to N_2 shows a negligible influence and only hydrogen and ammonia remain in the adsorption term of the LHHW expression (Eq. 3). The second branch of the curves, to the right after the maximum, converge towards

equilibrium lines characterized by higher ammonia conversion, since the increase of H_2/N_2 increases the equilibrium ammonia concentration in the mixture.

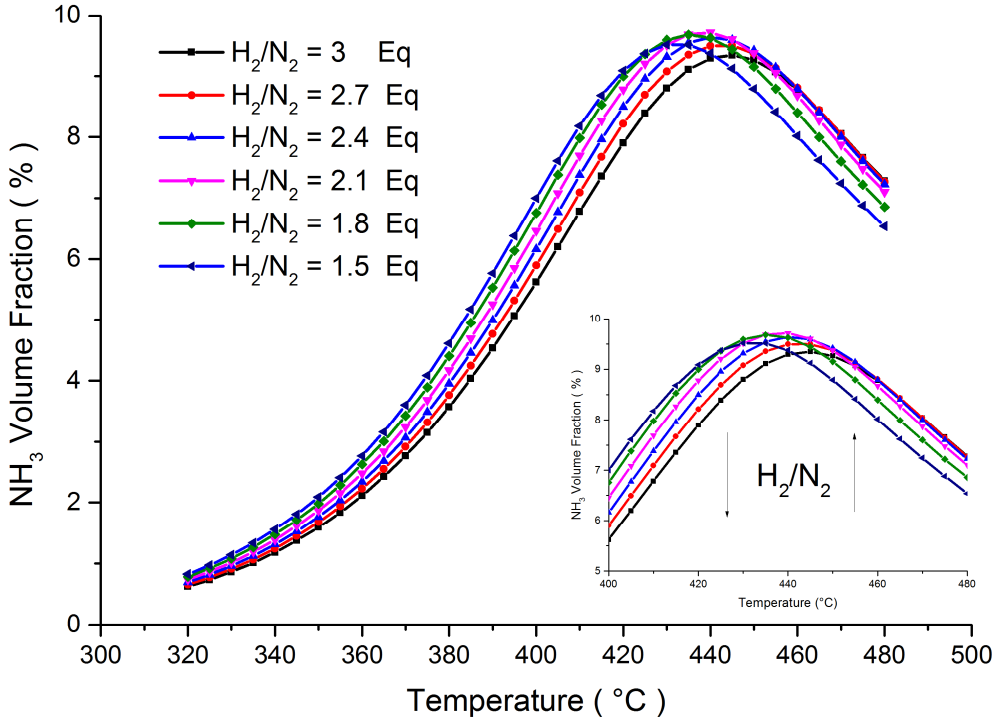

Figure 5.6. Comparison of ammonia production predicted by the kinetic model at different H_2/N_2 ratios GHSV = $0.5*10^5$ h^{-1}, P = 70bar).

Effect of reaction pressure - Ammonia synthesis is a reaction occurring with mole reduction, therefore from the thermodynamic standpoint, the equilibrium conversion should be enhanced by raising the reaction pressure. The evaluation of optimal pressure is fundamental because it influences also the gas/liquid equilibrium in the product separation after the reactor. Furthermore, the power consumption for gas compression, recirculation and refrigeration depends critically on the operating pressure. In order to study the pressure effect, the lowest value of GHSV ($0.5*10^5$ h^{-1}) was used under isothermal conditions. The simulation results are shown in Figure 5.7. The relationship between the activity (ammonia concentration in the outlet stream) and reaction pressure was linear: the higher the pressure, the higher would be the concentration of outlet ammonia.

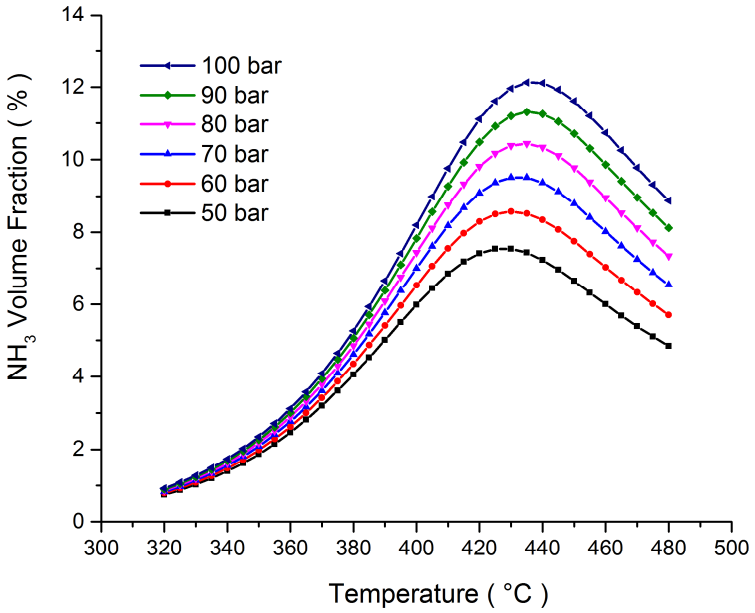

Figure 5.7. Comparison of ammonia concentration in the outlet gas predicted by the used kinetic model at different pressures (GHSV = $0.5*10^5$ h^{-1} , H_2/N_2 = 1.5 v/v).

Conclusion - Ammonia synthesis was the first high pressure catalytic process and its development became the testing ground for high pressure reactor and process technology eventually applied to other reactions. Within the wide range of specialized software for process simulation in chemical engineering, the software Aspen Plus© positioned today as one of the best in its class and it is increasingly used in industry and academia worldwide.

The performance of the catalyst is influenced significantly by the operating conditions adopted in the ammonia production process and with proper operation and maintenance. In selecting the optimum conditions, it is necessary to consider many factors including thermodynamics, reaction kinetics, yields and energy consumption. Both the process and the equipment need to be considered. In this work, the goal was a detailed study of the reactor implemented with the new kinetic and thermodynamic parameters. The process simulation with the implemented kinetic parameters developed in detail in a previous work [105], was validated, establishing that Aspen Plus© is a credible platform to simulate the industrial process under these conditions.

6. References

This PhD thesis incorporates material from papers published as main author and co-author by Matteo Compagnoni. In particular, Chapter 1 uses material from references [327–329], coauthored with Antonio Tripodi, Ilenia Rossetti, Ehsan Mostafavi, Nader Mahinpey, Alessandro Di Michele, Paola Sassi, Michela Signoretto. Chapter 2 uses material from reference [158], coauthored with Ilenia Rossetti, Antonio Tripodi, Elisabetta Finocchio, Gianguido Ramis, Alessandro Di Michele, Yannick Millot, Stanislaw Dzwigaj. Chapter 3 uses material from reference [330], coauthored with Simon A. Kondrat, Ilenia Rossetti, Carine E. Chan-Thaw, David J. Morgan, Di Wang, Laura Prati. Chapter 4 uses material from reference [331] coauthored with Davide Vitali, Carlo Pirola, Claudia L. Bianchi, Federico Galli, Ilenia Rossetti, Alberto Villa, Laura Prati.

[1] J. Sun, Y. Wang, ACS Catal. 4 (2014) 1078–1090.
[2] M. Ni, D.Y.C. Leung, M.K.H. Leung, Int. J. Hydrogen Energy 32 (2007) 3238–3247.
[3] K.O. Christensen, D. Chen, R. Lødeng, A. Holmen, Appl. Catal. A Gen. 314 (2006) 9–22.
[4] G. Busca, T. Montanari, C. Resini, G. Ramis, U. Costantino, Catal. Today 143 (2009) 2–8.
[5] R.M. Navarro, M. a Pea, J.L.G. Fierro, M. a Pen, Chem. Rev. 107 (2007) 3952–3991.
[6] W. Xu, Z. Liu, A.C. Johnston-Peck, S.D. Senanayake, G. Zhou, D. Stacchiola, E. a. Stach, J. a. Rodriguez, ACS Catal. 3 (2013) 975–984.
[7] J. Rass-Hansen, C.H. Christensen, J. Sehested, S. Helveg, J.R. Rostrup-Nielsen, S. Dahl, Green Chem. 9 (2007) 1016.
[8] L. V. Mattos, G. Jacobs, B.H. Davis, F.B. Noronha, Chem. Rev. 112 (2012) 4094–4123.
[9] F. Wang, Y. Li, W. Cai, E. Zhan, X. Mu, W. Shen, Catal. Today 146 (2009) 31–36.
[10] Z. Ferencz, A. Erd, K. Baan, A. Oszkó, L. Óvári, Z. Konya, C. Papp, H. Steinrück, J. Kiss, ACS Catal. 4 (2014) 1205–1218.
[11] D. Zanchet, J.B.O. Santos, S. Damyanova, J.M.R. Gallo, J.M.C. Bueno, ACS Catal. 5 (2015) 3841–3863.
[12] A.M. Karim, Y. Su, M.H. Engelhard, D.L. King, Y. Wang, ACS Catal. 1 (2011) 279–286.
[13] G. Ramis, I. Rossetti, E. Finocchio, M. Compagnoni, M. Signoretto, A. Di Michele, in:, Prog. Clean Energy, 2015, pp. 695–711.
[14] F. Frusteri, S. Freni, J. Power Sources 173 (2007) 200–209.
[15] D. Mei, V. Lebarbier Dagle, R. Xing, K.O. Albrecht, R.A. Dagle, ACS Catal. 6 (2015) 315–325.
[16] J. Baltrusaitis, W.L. Luyben, ACS Sustain. Chem. Eng. 3 (2015) 2100–2111.
[17] M. Dömök, A. Oszkó, K. Baán, I. Sarusi, A. Erdőhelyi, Appl. Catal. A Gen. 383 (2010) 33–42.
[18] I. Rossetti, A. Gallo, V. Dal Santo, C.L. Bianchi, V. Nichele, M. Signoretto, E. Finocchio, G. Ramis, A. Di Michele, ChemCatChem 5 (2013) 294–306.
[19] I. Rossetti, C. Biffi, C.L. Bianchi, V. Nichele, M. Signoretto, F. Menegazzo, E. Finocchio, G. Ramis, A. Di Michele, Appl. Catal. B Environ. 117-118 (2012) 384–396.
[20] J. Ma, C. Jiang, P.A. Connor, M. Cassidy, J.T.S. Irvine, J. Mater. Chem. A 3 (2015) 19068–19076.
[21] V.R. Choudhary, B.S. Uphade, A.S. Mamman, Microporous Mesoporous Mater. 23 (1998) 61–66.
[22] M. Kusche, F. Enzenberger, S. Bajus, H. Niedermeyer, A. Bösmann, A. Kaftan, M. Laurin, J.

Libuda, P. Wasserscheid, Angew. Chemie - Int. Ed. 52 (2013) 5028–5032.
[23] Harshini, D.H. Lee, J. Jeong, Y. Kim, S.W. Nam, H.C. Ham, J.H. Han, T.-H. Lim, C.W. Yoon, Appl. Catal. B Environ. 148-149 (2014) 415–423.
[24] L. Pino, A. Vita, F. Cipitì, M. Laganà, V. Recupero, Appl. Catal. B Environ. 104 (2011) 64–73.
[25] M.. Sanchez-Sanchez, R.M. Navarro, J.L.. Fierro, Int. J. Hydrogen Energy 32 (2007) 1462–1471.
[26] V. Nichele, M. Signoretto, F. Pinna, F. Menegazzo, I. Rossetti, G. Cruciani, G. Cerrato, A. Di Michele, Appl. Catal. B Environ. 150-151 (2014) 12–20.
[27] I. Rossetti, J. Lasso, V. Nichele, M. Signoretto, E. Finocchio, G. Ramis, A. Di Michele, Appl. Catal. B Environ. 150-151 (2014) 257–267.
[28] L. Mädler, H.K. Kammler, R. Mueller, S.E. Pratsinis, J. Aerosol Sci. 33 (2002) 369–389.
[29] B. Pongthawornsakun, O. Mekasuwandumrong, S. Prakash, E. Ehret, F.J.C. Santos Aires, J. Panpranot, Appl. Catal. A Gen. 506 (2015) 278–287.
[30] G.L. Chiarello, I. Rossetti, L. Forni, J. Catal. 236 (2005) 251–261.
[31] G.L. Chiarello, I. Rossetti, L. Forni, P. Lopinto, G. Migliavacca, Appl. Catal. B Environ. 72 (2007) 227–232.
[32] G.L. Chiarello, I. Rossetti, L. Forni, P. Lopinto, G. Migliavacca, Appl. Catal. B Environ. 72 (2007) 218–226.
[33] V. García, J.J. Fernández, W. Ruíz, F. Mondragón, A. Moreno, Catal. Commun. 11 (2009) 240–246.
[34] Z.J. Li, H. a Prescott, J. Deutsch, a Trunschke, H. Lieske, E. Kemnitz, Catal. Letters 92 (2004) 175–180.
[35] R. Strobel, S.E. Pratsinis, J. Mater. Chem. 17 (2007) 4743–4756.
[36] R. Mueller, L. Mädler, S.E. Pratsinis, Chem. Eng. Sci. 58 (2003) 1969–1976.
[37] T. Chraska, A.H. King, C.C. Berndt, Mater. Sci. Eng. A 286 (2000) 169–178.
[38] Y.J.O. Asencios, J.D.A. Bellido, E.M. Assaf, Appl. Catal. A Gen. 397 (2011) 138–144.
[39] M.-S. Fan, A.Z. Abdullah, S. Bhatia, Appl. Catal. B Environ. 100 (2010) 365–377.
[40] W.Y. Teoh, D.E. Doronkin, G.K. Beh, J.A.H. Dreyer, J.-D. Grunwaldt, J. Catal. 326 (2015) 182–193.
[41] R. Büchel, A. Baiker, S.E. Pratsinis, Appl. Catal. A Gen. 477 (2014) 93–101.
[42] W.M. Haynes, CRC Handbook of Chemistry and Physics, 95th Ed., 2015.
[43] Y.Q. Song, D.H. He, B.Q. Xu, Appl. Catal. A Gen. 337 (2008) 19–28.
[44] W.S. Dong, H.S. Roh, K.W. Jun, S.E. Park, Y.S. Oh, Appl. Catal. A Gen. 226 (2002) 63–72.
[45] S.D. Angeli, L. Turchetti, G. Monteleone, A.A. Lemonidou, Appl. Catal. B Environ. 181 (2016) 34–46.
[46] J.D. a Bellido, E.M. Assaf, J. Power Sources 177 (2008) 24–32.
[47] F. Frusteri, S. Freni, V. Chiodo, L. Spadaro, O. Di Blasi, G. Bonura, S. Cavallaro, Appl. Catal. A Gen. 270 (2004) 1–7.
[48] H. Laversin, D. Courcot, E. a. Zhilinskaya, R. Cousin, A. Aboukaïs, J. Catal. 241 (2006) 456–464.
[49] J.H. Oakley, a. F. a Hoadley, Int. J. Hydrogen Energy 35 (2010) 8472–8485.
[50] D.A. Morgenstern, J.P. Fornango, Energy and Fuels 19 (2005) 1708–1716.
[51] P.D. Vaidya, A.E. Rodrigues, Chem. Eng. J. 117 (2006) 39–49.
[52] J. Rostrup-Nielsen, Catalytic Steam Reforming, 1984.
[53] I. Rossetti, L. Sordelli, P. Ghigna, S. Pin, M. Scavini, L. Forni, Inorg. Chem. 50 (2011) 3757–3765.
[54] I. Rossetti, F. Mangiarini, L. Forni, Appl. Catal. A Gen. 323 (2007) 219–225.
[55] I. Rossetti, N. Pernicone, L. Forni, Appl. Catal. A Gen. 208 (2001) 271–278.
[56] J.D. a Bellido, J.E. De Souza, J.C. M'Peko, E.M. Assaf, Appl. Catal. A Gen. 358 (2009) 215–223.

[57] J.R. Rostrup-Nielsen, Catal. Today 63 (2000) 159–164.
[58] I. Rossetti, J. Lasso, V. Nichele, M. Signoretto, E. Finocchio, G. Ramis, A. Di Michele, Appl. Catal. B Environ. 150-151 (2014) 257–267.
[59] I. Rossetti, M. Compagnoni, M. Torli, Chem. Eng. J. 281 (2015) 1024–1035.
[60] I. Rossetti, M. Compagnoni, M. Torli, Chem. Eng. J. 281 (2015) 1036–1044.
[61] I. Rossetti, M. Compagnoni, E. Finocchio, G. Ramis, A. Di Michele, A. Zucchini, S. Dzwigaj, Int. J. Hydrogen Energy 41 (2016) 16878–16889.
[62] A. Comazzi, C. Pirola, A. Di Michele, M. Compagnoni, F. Galli, I. Rossetti, F. Manenti, C.L. Bianchi, Appl. Catal. A Gen. 520 (2016) 92–98.
[63] A.E. Galetti, M.F. Gomez, L. a. Arrúa, M.C. Abello, Appl. Catal. A Gen. 348 (2008) 94–102.
[64] C. Choong, Z. Zhong, L. Huang, A. Borgna, L. Hong, L. Chen, J. Lin, ACS Catal. 4 (2014) 2359–2363.
[65] A.M. Karim, Y. Su, J. Sun, C. Yang, J.J. Strohm, D.L. King, Y. Wang, Appl. Catal. B Environ. 96 (2010) 441–448.
[66] T.S. Moraes, R.C. Rabelo Neto, M.C. Ribeiro, L.V. Mattos, M. Kourtelesis, S. Ladas, X. Verykios, F.B. Noronha, Appl. Catal. B Environ. 181 (2016) 754–768.
[67] F.D. Alvarado, F. Gracia, 165 (2010) 649–657.
[68] D.L. Trimm, Catal. Today 37 (1997) 233–238.
[69] A. Donazzi, D. Pagani, A. Lucotti, M. Tommasini, A. Beretta, G. Groppi, C. Castiglioni, P. Forzatti, Appl. Catal. A Gen. 474 (2014) 149–158.
[70] a. Serrano-Lotina, L. Daza, Appl. Catal. A Gen. 474 (2014) 107–113.
[71] P.D. Vaidya, a E. Rodrigues, Ind. Eng. Chem. Res. 45 (2006) 6614–6618.
[72] D.R. Sahoo, S. Vajpai, S. Patel, K.K. Pant, Chem. Eng. J. 125 (2007) 139–147.
[73] I. Llera, V. Mas, M.L. Bergamini, M. Laborde, N. Amadeo, Chem. Eng. Sci. 71 (2012) 356–366.
[74] V. Mas, M.L. Bergamini, G. Baronetti, N. Amadeo, M. Laborde, Top. Catal. 51 (2008) 39–48.
[75] J.H. Wang, C.S. Lee, M.C. Lin, J. Phys. Chem. C 113 (2009) 6681–6688.
[76] M. a. Christiansen, G. Mpourmpakis, D.G. Vlachos, J. Catal. 323 (2015) 121–131.
[77] J.E. Sutton, D.G. Vlachos, Ind. Eng. Chem. Res. 54 (2015) 4213−4225.
[78] R.J. Berger, J. Perez-Ramìrez, F. Kapteijn, J.A. Moulijn, Chem. Eng. Sci. 57 (2002) 4921.
[79] I. Rossetti, J. Lasso, M. Compagnoni, G. De Guido, L. Pellegrini, Chem. Eng. Trans. 43 (2015) 229–234.
[80] F. Wang, W. Cai, C. Descorme, H. Provendier, W. Shen, C. Mirodatos, Y. Schuurman, Int. J. Hydrogen Energy 39 (2014) 18005–18015.
[81] A.N. Fatsikostas, X.E. Verykios, J. Catal. 225 (2004) 439–452.
[82] G. Zeng, Y. Li, U. Olsbye, Catal. Today 259 (2015) 312–322.
[83] H. Song, L. Zhang, U.S. Ozkan, Ind. Eng. Chem. Res. 2 (2010) 8984–8989.
[84] T. Hou, S. Zhang, Y. Chen, D. Wang, W. Cai, Renew. Sustain. Energy Rev. 44 (2015) 132–148.
[85] P. Ciambelli, V. Palma, a. Ruggiero, Appl. Catal. B Environ. 96 (2010) 190–197.
[86] J.E. Sutton, P. Panagiotopoulou, X.E. Verykios, D.G. Vlachos, J. Phys. Chem. C 117 (2013) 4691–4706.
[87] F. Frusteri, S. Freni, V. Chiodo, S. Donato, G. Bonura, S. Cavallaro, Int. J. Hydrogen Energy 31 (2006) 2193–2199.
[88] J.C. Escobar, E.S. Lora, O.J. Venturini, E.E. Yáñez, E.F. Castillo, O. Almazan, Renew. Sustain. Energy Rev. 13 (2009) 1275–1287.
[89] (2017).
[90] D.M. Alonso, J.Q. Bond, J.A. Dumesic, Green Chem. 12 (2010) 1493–1513.
[91] F. Lee, R.H. Pahl, Ind. Eng. Chem. Process Des. Dev. 24 (1985) 168–172.
[92] P.K. Seelam, S. Liguori, A. Iulianelli, P. Pinacci, V. Calabrò, M. Huuhtanen, R. Keiski, V.

Piemonte, S. Tosti, M. De Falco, A. Basile, Catal. Today 193 (2012) 42–48.
[93] H. Habe, T. Shinbo, T. Yamamoto, S. Sato, H. Shimada, K. Sakaki, J. Japan Pet. Inst. 56 (2013) 414–422.
[94] T. Mondal, K.K. Pant, A.K. Dalai, Appl. Catal. A Gen. 499 (2015) 19–31.
[95] A. Le Valant, F. Can, N. Bion, D. Duprez, F. Epron, Int. J. Hydrogen Energy 35 (2010) 5015–5020.
[96] J. Chaichanawong, T. Yamamoto, T. Ohmori, A. Endo, Chem. Eng. J. 165 (2010) 218–224.
[97] W. Torres, S.S. Pansare, J.G. Goodwin, Catal. Rev. 49 (2007) 407–456.
[98] P. Forzatti, Catal. Today 52 (1999) 165–181.
[99] N. Bion, D. Duprez, F. Epron, ChemSusChem 5 (2012) 76–84.
[100] A. Le Valant, A. Garron, N. Bion, D. Duprez, F. Epron, Int. J. Hydrogen Energy 36 (2011) 311–318.
[101] J. Rass-Hansen, R. Johansson, M. Møller, C.H. Christensen, Int. J. Hydrogen Energy 33 (2008) 4547–4554.
[102] P. Alvira, E. Tomàs-Pejò, M. Ballesteros, M.J. Negro, Bioresour. Technol. 101 (2010) 4851–4861.
[103] G. Garbarino, A. Romero Perez, E. Finocchio, G. Busca, Catal. Commun. 38 (2013) 67–73.
[104] R.M. Navarro, M. a. Peña, J.L.G. Fierro, Chem. Rev. 107 (2007) 3952–3991.
[105] I. Rossetti, N. Pernicone, F. Ferrero, L. Forni, Ind. Eng. Chem. Res. 45 (2006) 4150–4155.
[106] W.L. Luyben, Ind. Eng. Chem. Res. 49 (2010) 6150–6163.
[107] J. Baltrusaitis, W.L. Luyben, ACS Sustain. Chem. Eng. 3 (2015) 2100–2111.
[108] F. Gallucci, M. Van Sint Annaland, J.A.M. Kuipers, Top. Catal. 51 (2008) 133–145.
[109] M.A. Mujeebu, M.Z. Abdullah, M.Z.A. Bakar, A.A. Mohamad, M.K. Abdullah, Prog. Energy Combust. Sci. 35 (2009) 216–230.
[110] S. Galera, F.J. Gutiérrez Ortiz, Fuel 144 (2015) 307–316.
[111] P. Giunta, C. Mosquera, N. Amadeo, M. Laborde, J. Power Sources 164 (2007) 336–343.
[112] V. Spallina, D. Pandolfo, A. Battistella, M.C. Romano, M. Van Sint Annaland, F. Gallucci, Energy Convers. Manag. 120 (2016) 257–273.
[113] H. Song, U.S. Ozkan, Int. J. Hydrogen Energy 35 (2010) 127–134.
[114] J.H. Oakley, A.F.A. Hoadley, Int. J. Hydrogen Energy 35 (2010) 8472–8485.
[115] M.S. Peters, K.D. Timmerhaus, Plant Design and Economics for Chemical Engineers, 1991.
[116] S.S. Hla, D. Park, G.J. Duffy, J.H. Edwards, D.G. Roberts, A. Ilyushechkin, L.D. Morpeth, T. Nguyen, Chem. Eng. J. 146 (2009) 148–154.
[117] Y. Choi, H.G. Stenger, J. Power Sources 124 (2003) 432–439.
[118] J. Zhang, N. Fatah, S. Capela, Y. Kara, O. Guerrini, A.Y. Khodakov, Fuel 111 (2013) 845–854.
[119] J. Zhang, N. Fatah, S. Capela, Y. Kara, O. Guerrini, A.Y. Khodakov, Fuel 111 (2013) 845–854.
[120] C.H. Bartholomew, R. Farrauto, Fundamentals of Industrial Catalytic Processes, John Wiley & Sons, 2011.
[121] J.S.S. Mohammadzadeh, A. Zamaniyan, Chem. Eng. Res. Des. 80 (2002) 383–390.
[122] A. Tripodi, M. Compagnoni, G. Ramis, I. Rossetti, Int. J. Hydrogen Energy (2017) in press.
[123] H. Er-rbib, C. Bouallou, Chem. Eng. Trans. 35 (2013) 541–546.
[124] A. Criscuoli, A. Basile, E. Drioli, O. Loiacono, J. Mem 181 (2001) 21–27.
[125] (2017).
[126] M. Compagnoni, J. Lasso, A. Di Michele, I. Rossetti, Catal. Sci. Technol. 6 (2016) 6247–6256.
[127] S. Cavallaro, Energy & Fuels 14 (2000) 1195–1199.
[128] W.L. Luyben, J. Process Control 39 (2016) 77–87.
[129] A. Mivechian, M. Pakizeh, Chem. Eng. Technol. 36 (2013) 519–527.
[130] A.-M. Cormos, C.-C. Cormos, Int. J. Hydrogen Energy (2016) 1–13.

[131] E. Esmaili, E. Mostafavi, N. Mahinpey, Appl. Energy 169 (2016) 341–352.
[132] E. Mostafavi, M.H. Sedghkerdar, N. Mahinpey, Ind. Eng. Chem. Res. 52 (2013) 4725–4733.
[133] P. Baladincz, J. Hancsòk, Chem. Eng. J. 282 (2015) 152–160.
[134] F.K. Kazi, J.A. Fortman, R.P. Anex, D.D. Hsu, A. Aden, A. Dutta, G. Kothandaraman, Fuel 89 (2010) S20–S28.
[135] M. Nasidi, J. Akunna, Y. Deeni, D. Blackwood, G. Walker, Energy Environ. Sci. 3 (2010) 1447.
[136] P. Unrean, S. Khajeeram, Renew. Energy 99 (2016) 1062–1072.
[137] M. Bornapour, R.A. Hooshmand, A. Khodabakhshian, M. Parastegari, Appl. Energy 202 (2017) 308–322.
[138] H. Zimmermann, R. Walzl, Ullmann's Encyclopedia of Industrial Chemistry, 2009.
[139] S. Bastianoni, N. Marchettini, Biomass Bioenergy 11 (1996) 411−418.
[140] G. Huber, S. Iborra, A. Corma, Chem. Rev. 106 (2006) 4044−4098.
[141] H. Chiang, A. Bhan, J. Catal. 271 (2010) 251–261.
[142] C. de las Pozas, R. Lopez-Cordero, J.A. Gonzalez-Morales, N. Travieso, R. Roque-Malherbe, J. Mol. Catal. 83 (1993) 145–156.
[143] A. Morschbacker, Polym. Rev. 49 (2009) 79.
[144] T.K. Phung, G. Busca, Chem. Eng. J. 272 (2015) 92–101.
[145] T.K. Phung, L. Proietti Hernández, A. Lagazzo, G. Busca, Appl. Catal. A Gen. 493 (2015) 77–89.
[146] T.K. Phung, R. Radikapratama, G. Garbarino, A. Lagazzo, P. Riani, G. Busca, Fuel Process. Technol. 3 (2015).
[147] K.K. Ramasamy, Y. Wang, Catal. Today 237 (2014) 89–99.
[148] J.M.R. Gallo, U. Schuchardt, 25 (2014) 2229–2243.
[149] J. Sun, Y. Wang, ACS Catal. 4 (2014) 1078–1090.
[150] E.L. First, C.E. Gounaris, J. Wei, C. a. Floudas, Phys. Chem. Chem. Phys. 13 (2011) 17339.
[151] I. Rossetti, M. Compagnoni, E. Finocchio, G. Ramis, A. Di Michele, A. Zucchini, S. Dzwigaj, Int. J. Hydrog. Energy (n.d.).
[152] E. Finocchio, I. Rossetti, G. Ramis, Int. J. Hydrogen Energy 38 (2013) 3213–3225.
[153] V. Nichele, M. Signoretto, F. Menegazzo, I. Rossetti, G. Cruciani, Int. J. Hydrogen Energy 39 (2014) 4252–4258.
[154] I. Rossetti, C. Biffi, C.L. Bianchi, V. Nichele, M. Signoretto, F. Menegazzo, E. Finocchio, G. Ramis, A. Di Michele, Appl. Catal. B Environ. 117-118 (2012) 384–396.
[155] G. Centi, S. Perathoner, Catal. Today 148 (2009) 191–205.
[156] V. Gonzalez De La Cruz, J. Holgado, R. Pereniguez, A. Caballero, J. Catal. 257 (2008) 307–314.
[157] D. Chen, K.O. Christensen, E. Ochoa-Fernández, Z. Yu, B. Tøtdal, N. Latorre, A. Monzón, A. Holmen, J. Catal. 229 (2005) 82–96.
[158] I. Rossetti, M. Compagnoni, E. Finocchio, G. Ramis, A. Di Michele, Y. Millot, S. Dzwigaj, Appl. Catal. B Environ. 210 (2017) 407–420.
[159] J.P. Marques, I. Gener, P. Ayrault, J.C. Bordado, J.M. Lopes, F.. Ramôa Ribeiro, M. Guisnet, Microporous Mesoporous Mater. 60 (2003) 251–262.
[160] A. Simon-Masseron, J.P. Marques, J.M. Lopes, F. Ramôa Ribeiro, I. Gener, M. Guisnet, Appl. Catal. A Gen. 316 (2007) 75–82.
[161] J.M. Müller, G.C. Mesquita, S.M. Franco, L.D. Borges, J.L. de Macedo, J. a. Dias, S.C.L. Dias, Microporous Mesoporous Mater. 204 (2015) 50–57.
[162] R. Hajjar, Y. Millot, P.P. Man, M. Che, S. Dzwigaj, J. Phys. Chem. C 112 (2008) 20167–20175.
[163] A.J. Jones, R.T. Carr, S.I. Zones, E. Iglesia, J. Catal. 312 (2014) 58.
[164] K. Hadjiivanov, Adv. Catal. 57 (2014) 99–318.
[165] I. Takahara, M. Saito, M. Inaba, K. Murata, Catal. Letters 105 (2005) 249–252.

[166] H. Xin, X. Li, Y. Fang, X. Yi, W. Hu, Y. Chu, F. Zhang, A. Zheng, H. Zhang, X. Li, J. Catal. 312 (2014) 204–215.
[167] R. Le Van Mao, T.M. Nguyen, J. Yao, Appl. Catal. 61 (1990) 161–173.
[168] T.M. Nguyen, R. Le Van Mao, Appl. Catal. 58 (1990) 119–129.
[169] C.B. Phillips, R. Datta, Ind. Eng. Chem. Res. 36 (1997) 4466–4475.
[170] V. V. Bokade, G.D. Yadav, Appl. Clay Sci. 53 (2011) 263–271.
[171] A.T. Aguayo, A.G. Gayubo, A. Atutxa, M. Olazar, J. Bilbao, Ind. Eng. Chem. Res. 41 (2002) 4216–4224.
[172] J.F. DeWilde, H. Chiang, D. a Hickman, C.R. Ho, A. Bhan, ACS Catal. 3 (2013) 798–807.
[173] T. Maihom, P. Khongpracha, J. Sirijaraensre, J. Limtrakul, ChemPhysChem 14 (2013) 101–107.
[174] Q. Sheng, S. Guo, K. Ling, L. Zhao, J. Braz. Chem. Soc. 25 (2014) 1365–1371.
[175] Q. Sheng, K. Ling, Z. Li, L. Zhao, Fuel Process. Technol. 110 (2013) 73–78.
[176] G.J. Hutchings, Top. Catal. 57 (2014) 1265–1271.
[177] G. Li, L. Li, D. Jiang, J. Phys. Chem. C 119 (2015) 12502–12507.
[178] M. Du, D. Sun, H. Yang, J. Huang, X. Jing, T. Odoom-wubah, H. Wang, L. Jia, Q. Li, J. Phys. Chem. C 118 (2014) 19150–19157.
[179] M. Haruta, Chem. Rec. 3 (2003) 75–87.
[180] S. Lin, X. Ye, R.S. Johnson, H. Guo, J. Phys. Chem. C 117 (2013) 17319–17326.
[181] a. S.K. Hashmi, G.J. Hutchings, Angew. Chemie - Int. Ed. 45 (2006) 7896–7936.
[182] N. Dimitratos, J.A. Lopez-Sanchez, G.J. Hutchings, Chem. Sci. 3 (2012) 20–44.
[183] B.K. Min, C.M. Friend, Chem. Rev. 107 (2007) 2709–2724.
[184] E.D. Park, J.S. Lee, J. Catal. 186 (1999) 1–11.
[185] B. Yoon, H. Häkkinen, U. Landman, A.S. Wörz, J.-M. Antonietti, S. Abbet, K. Judai, U. Heiz, Science 307 (2005) 403–407.
[186] W.T. Wallace, R.L. Whetten, J. Am. Chem. Soc. 124 (2002) 7499–7505.
[187] K. Chakarova, M. Mihaylov, S. Ivanova, M. a. Centeno, K. Hadjiivanov, J. Phys. Chem. C 115 (2011) 21273–21282.
[188] R. Zanella, L. Delannoy, C. Louis, Appl. Catal. A Gen. 291 (2005) 62–72.
[189] W.C. Li, M. Comotti, F. Schüth, J. Catal. 237 (2006) 190–196.
[190] T. Venkov, K. Fajerwerg, L. Delannoy, H. Klimev, K. Hadjiivanov, C. Louis, Appl. Catal. A Gen. 301 (2006) 106–114.
[191] N. Dimitratos, J.A. Lopez-Sanchez, D. Morgan, A. Carley, L. Prati, G.J. Hutchings, Catal. Today 122 (2007) 317–324.
[192] L. Prati, A. Villa, Catalysts 2 (2011) 24–37.
[193] S. Chen, B. Zhang, D. Su, W. Huang, ChemCatChem 7 (2015) 3290–3298.
[194] K.C. Petallidou, S. Boghosian, A.M. Efstathiou, Catal. Today 242 (2015) 153–167.
[195] N. Dimitratos, A. Villa, C.L. Bianchi, L. Prati, M. Makkee, Appl. Catal. A Gen. 311 (2006) 185–192.
[196] H. Huang, X. Ye, H. Huang, L. Zhang, D.Y.C. Leung, Chem. Eng. J. 230 (2013) 73–79.
[197] F.E. López-Suárez, a. Bueno-López, K.I.B. Eguiluz, G.R. Salazar-Banda, J. Power Sources 268 (2014) 225–232.
[198] A. Kumar, V. Pavan, V.P. Kumar, B.P. Kumar, V. Vishwanathan, K.V.R. Chary, Catal. Letters 144 (2014) 1450–1459.
[199] F. Zaera, Chem. Soc. Rev. 43 (2014) 7624–7663.
[200] C. Lamberti, A. Zecchina, E. Groppo, S. Bordiga, Chem. Soc. Rev. 39 (2010) 4951–5001.
[201] K. Hadjiivanov, D. Klissurski, G. Ramis, G. Busca, Appl. Catal. B Environ. 7 (1996) 251–267.
[202] W. Zhou, Y. Zhang, M. Abe, K. Uosaki, M. Osawa, Y. Sasaki, S. Ye, Langmuir 24 (2008) 8027–35.
[203] G. Busca, Catal. Today 41 (1998) 191–206.

[204] I. Rossetti, G.F. Mancini, P. Ghigna, M. Scavini, M. Piumetti, B. Bonelli, F. Cavani, A. Comite, J. Phys. Chem. C 116 (2012) 22386–22398.
[205] K.I. Hadjiivanov, G.N. Vayssilov, Adv. Catal. 47 (2002) 307–511.
[206] G. Blyholder, J. Phys. Chem. 79 (1974) 756–761.
[207] S. Zou, R. Go, M.J. Weaver, Langmuir 7463 (1997) 6713–6721.
[208] C. Liu, M. Virginie, A. Griboval-Constant, A. Khodakov, Appl. Catal. A Gen. 504 (2015) 1–11.
[209] M. a. Debeila, N.J. Coville, M.S. Scurrell, G.R. Hearne, Catal. Today 72 (2002) 79–87.
[210] F. Boccuzzi, A. Chiorino, J. Phys. Chem. 100 (1996) 3617–3624.
[211] D. a. Panayotov, S.P. Burrows, J.T. Yates, J.R. Morris, J. Phys. Chem. C 115 (2011) 22400–22408.
[212] F. Boccuzzi, a Chiorino, J. Phys. Chem. B 104 (2000) 5414–5416.
[213] J. Wang, V.F. Kispersky, W. Nicholas Delgass, F.H. Ribeiro, J. Catal. 289 (2012) 171–178.
[214] F. Boccuzzi, a Chiorino, M. Manzoli, P. Lu, T. Akita, S. Ichikawa, M. Haruta, J. Catal. 202 (2001) 256–267.
[215] S. Oros-Ruiz, R. Zanella, R. López, A. Hernández-Gordillo, R. Gómez, J. Hazard. Mater. 263 (2013) 2–10.
[216] B. Schumacher, Y. Denkwitz, V. Plzak, M. Kinne, R.J. Behm, J. Catal. 224 (2004) 449–462.
[217] M. Manzoli, a. Chiorino, F. Boccuzzi, Surf. Sci. 532-535 (2003) 377–382.
[218] A. Villa, C.E. Chan-Thaw, G.M. Veith, K.L. More, D. Ferri, L. Prati, ChemCatChem 3 (2011) 1612–1618.
[219] A. Villa, D. Ferri, S. Campisi, C.E. Chan-Thaw, Y. Lu, O. Kröcher, L. Prati, ChemCatChem 7 (2015) 2534–2541.
[220] E. del Río, S.E. Collins, A. Aguirre, X. Chen, J.J. Delgado, J.J. Calvino, S. Bernal, J. Catal. 316 (2014) 210–218.
[221] F. Boccuzzi, A. Chiorino, M. Manzoli, D. Andreeva, T. Tabakova, J. Catal. 188 (1999) 176–185.
[222] T. Tabakova, F. Boccuzzi, M. Manzoli, D. Andreeva, Appl. Catal. A Gen. 252 (2003) 385–397.
[223] J.D. Henao, T. Caputo, J.H. Yang, M.C. Kung, H.H. Kung, J. Phys. Chem. B 110 (2006) 8689–8700.
[224] A. Villa, G.M. Veith, D. Ferri, A. Weidenkaff, K. a. Perry, S. Campisi, L. Prati, Catal. Sci. Technol. (2013) 394–399.
[225] M. Sterrer, M. Yulikov, E. Fischbach, M. Heyde, H.P. Rust, G. Pacchioni, T. Risse, H.J. Freund, Angew. Chemie - Int. Ed. 45 (2006) 2630–2632.
[226] a. M. Venezia, V. La Parola, G. Deganello, B. Pawelec, J.L.G. Fierro, J. Catal. 215 (2003) 317–325.
[227] M. Boronat, P. Concepción, a. Corma, J. Phys. Chem. C 113 (2009) 16772–16784.
[228] L.-C. de Me´norval, A. Chaqroune, B. Coq, and François Figueras, J. Chem. Soc. Faraday Trans. 93 (1997) 3715–3720.
[229] T. Yajima, H. Uchida, M. Watanabe, J. Phys. Chem. B 108 (2004) 2654–2659.
[230] S.M. Rogers, C.R. a. Catlow, C.E. Chan-Thaw, D. Gianolio, E.K. Gibson, A.L. Gould, N. Jian, A.J. Logsdail, R.E. Palmer, L. Prati, N. Dimitratos, A. Villa, P.P. Wells, ACS Catal. 5 (2015) 4377–4384.
[231] L. Piccolo, H. Daly, A. Valcarcel, F.C. Meunier, Appl. Catal. B Environ. 86 (2009) 190–195.
[232] S. Gaur, H. Wu, G.G. Stanley, K. More, C.S.S.R. Kumar, J.J. Spivey, Catal. Today 208 (2013) 72–81.
[233] O.H. Laguna, a. Pérez, M. a. Centeno, J. a. Odriozola, Appl. Catal. B Environ. 176-177 (2015) 385–395.
[234] M. Chen, Y. Cai, Z. Yan, D.W. Goodman, J. Am. Chem. Soc. 128 (2006) 6341–6346.
[235] M. a. Bollinger, M.A. Vannice, Appl. Catal. B Environ. 8 (1996) 417–443.

[236] M. Mihaylov, H. Knözinger, K. Hadjiivanov, B.C. Gates, Chemie Ing. Tech. 79 (2007) 795–806.
[237] G.M. Lari, E. Nowicka, D.J. Morgan, S. a. Kondrat, G.J. Hutchings, Phys. Chem. Chem. Phys. 17 (2015) 23236–23244.
[238] D. V. Kozlov, E.A. Paukshtis, E.N. Savinov, Appl. Catal. B Environ. 24 (2000) L7–L12.
[239] H. a. Rojas, J.J. Martínez, G. Díaz, A. Gómez-Cortés, Appl. Catal. A Gen. 503 (2015) 196–202.
[240] A. Sandoval, C. Louis, R. Zanella, Appl. Catal. B Environ. 140-141 (2013) 363–377.
[241] S. Arrii, S. Arrii, F. Morfin, F. Morfin, a J. Renouprez, a J. Renouprez, J.L. Rousset, J.L. Rousset, J. Am. Chem. Soc. 126 (2004) 1199–205.
[242] S. Albonetti, T. Pasini, A. Lolli, M. Blosi, M. Piccinini, N. Dimitratos, J. a. Lopez-Sanchez, D.J. Morgan, A.F. Carley, G.J. Hutchings, F. Cavani, Catal. Today 195 (2012) 120–126.
[243] J.M. López, R. Arenal, B. Puértolas, Á. Mayoral, S.H. Taylor, B. Solsona, T. García, J. Catal. 317 (2014) 167–175.
[244] C.C. Chusuei, X. Lai, K. Luo, D.W. Goodman, Top. Catal. 14 (2000) 71–83.
[245] A. Zwijnenburg, A. Goossens, W.G. Sloof, M.W.J. Craje, J. Phys. Chem. B 106 (2002) 9853–9862.
[246] K. Mori, T. Hara, T. Mizugaki, K. Ebitani, K. Kaneda, J. Am. Chem. Soc. 126 (2004) 10657–10666.
[247] M. Comotti, C. Della Pina, R. Matarrese, M. Rossi, Angew. Chemie - Int. Ed. 43 (2004) 5812–5815.
[248] M. Haruta, M. Daté, Appl. Catal. A Gen. 222 (2001) 427–437.
[249] F. Moreau, G. Bond, a Taylor, J. Catal. 231 (2005) 105–114.
[250] B.J. Auten, H. Lang, B.D. Chandler, Appl. Catal. B Environ. 81 (2008) 225–235.
[251] I.N. Remediakis, N. Lopez, J.K. Nørskov, Appl. Catal. A Gen. 291 (2005) 13–20.
[252] T. Fujitani, I. Nakamura, M. Haruta, Catal. Letters 144 (2014) 1475–1486.
[253] M.A. Larrubia, G. Ramis, G. Busca, Appl. Catal. B Environ. 27 (2000) L145–L151.
[254] H.L. Fang, H.F.M. DaCosta, Appl. Catal. B Environ. 46 (2003) 17–34.
[255] A.M. Bernhard, D. Peitz, M. Elsener, O. Kröcher, Top. Catal. 56 (2013) 130–133.
[256] W. Su, J. Zhang, Z. Feng, T. Chen, P. Ying, C. Li, J. Phys. Chem. C 112 (2008) 7710–7716.
[257] Z. Bacsik, N. Ahlsten, A. Ziadi, G. Zhao, A.E. Garcia-Bennett, B. Martín-Matute, N. Hedin, Langmuir 27 (2011) 11118–11128.
[258] F. Zaera, ChemCatChem 4 (2012) 1525–1533.
[259] T. Böcking, K. a. Kilian, T. Hanley, S. Ilyas, K. Gaus, M. Gal, J.J. Gooding, Langmuir 21 (2005) 10522–10529.
[260] Y. Izumi, in:, Adv. CO2 Capture, Sequestration Convers., American Chemical Society, Washington, 2015, p. 46.
[261] I. Rossetti, A. Villa, M. Compagnoni, L. Prati, G. Ramis, C. Pirola, C.L. Bianchi, W. Wang, D. Wang, Catal. Sci. Technol. 5 (2015) 4481–4487.
[262] I. Rossetti, A. Villa, C. Pirola, L. Prati, G. Ramis, RSC Adv. 4 (2014) 28883–28885.
[263] S.N. Habisreutinger, L. Schmidt-Mende, J.K. Stolarczyk, Angew. Chemie Int. Ed. 52 (2013) 7372–7408.
[264] B. Ohtani, J. Photochem. Photobiol. C Photochem. Rev. 11 (2010) 157–178.
[265] I. Rossetti, A. Villa, C. Pirola, L. Prati, G. Ramis, RSC Adv. 4 (2014) 28883–28885.
[266] K. Chandrasekaran, J.K. Thomas, Chem. Phys. Lett. 99 (1983) 7–10.
[267] C.H. Ao, S.C. Lee, J.Z. Yu, J.H. Xu, Appl. Catal. B Environ. 54 (2004) 41–50.
[268] S.S. Tan, L. Zou, E. Hu, Catal. Today 115 (2006) 269–273.
[269] H. Yamashita, A. Shiga, S. ichi Kawasaki, Y. Ichihashi, S. Ehara, M. Anpo, Energy Convers. Manag. 36 (1995) 617–620.
[270] Y. Li, W.-N. Wang, Z. Zhan, M.-H. Woo, C.-Y. Wu, P. Biswas, Appl. Catal. B Environ. 100 (2010) 386–392.

[271] S. Sakthivel, M.C. Hidalgo, D.W. Bahnemann, S.U. Geissen, V. Murugesan, A. Vogelpohl, Appl. Catal. B Environ. 63 (2006) 31–40.
[272] L. Liu, D.T. Pitts, H. Zhao, C. Zhao, Y. Li, Appl. Catal. A Gen. 467 (2013) 474–482.
[273] K. Kočí, L. Obalová, L. Matějová, D. Plachá, Z. Lacný, J. Jirkovský, O. Šolcová, Appl. Catal. B Environ. 89 (2009) 494–502.
[274] I.H. Tseng, W.C. Chang, J.C.S. Wu, Appl. Catal. B Environ. 37 (2002) 37–48.
[275] A. Corma, H. Garcia, J. Catal. 308 (2013) 168–175.
[276] M. de los M. Ballari, R. Brandi, O. Alfano, A. Cassano, Chem. Eng. J. 136 (2008) 50–65.
[277] M. de los M. Ballari, R. Brandi, O. Alfano, A. Cassano, Chem. Eng. J. 136 (2008) 242–255.
[278] M. Tahir, B. Tahir, N.A. Saidina Amin, H. Alias, Appl. Surf. Sci. 389 (2016) 46–55.
[279] I.H. Tseng, J.C.S. Wu, H.Y. Chou, J. Catal. 221 (2004) 432–440.
[280] B. Srinivas, B. Shubhamangala, K. Lalitha, P. Anil Kumar Reddy, V. Durga Kumari, M. Subrahmanyam, B.R. De, Photochem. Photobiol. 87 (2011) 995–1001.
[281] A.H. Yahaya, M.A. Gondal, A. Hameed, Chem. Phys. Lett. 400 (2004) 206–212.
[282] L. Collado, A. Reynal, J.M. Coronado, D.P. Serrano, J.R. Durrant, V.A. de la Peña O'Shea, Appl. Catal. B Environ. 178 (2015) 177–185.
[283] L. Matějová, K. Kočí, M. Reli, L. Capek, V. Matějka, O. Solcová, L. Obalová, Appl. Surf. Sci. 285 (2013) 688–696.
[284] M.V. Dozzi, L. Prati, P. Canton, E. Selli, Phys. Chem. Chem. Phys. 11 (2009) 7171–7180.
[285] M. Tahir, B. Tahir, N.A.S. Amin, Appl. Surf. Sci. 356 (2015) 1289–1299.
[286] S. Delavari, N.A.S. Amin, Appl. Energy 162 (2016) 1171–1185.
[287] L. Chen, M.E. Graham, G. Li, D.R. Gentner, N.M. Dimitrijevic, K.A. Gray, Thin Solid Films 517 (2009) 5641–5645.
[288] G. Li, S. Ciston, Z. V. Saponjic, L. Chen, N.M. Dimitrijevic, T. Rajh, K.A. Gray, J. Catal. 253 (2008) 105–110.
[289] B. Ohtani, O.O. Prieto-Mahaney, D. Li, R. Abe, J. Photochem. Photobiol. A Chem. 216 (2010) 179–182.
[290] A. Kafizas, X. Wang, S.R. Pendlebury, P. Barnes, M. Ling, C. Sotelo-Vazquez, R. Quesada-Cabrera, C. Li, I.P. Parkin, J.R. Durrant, J. Phys. Chem. A 120 (2016) 715–723.
[291] J. Kullgren, B. Aradi, T. Frauenheim, L. Kavan, P. De??k, J. Phys. Chem. C 119 (2015) 21952–21958.
[292] W. Lin, H. Han, H. Frei, J. Phys. Chem. B 108 (2004) 18269–18273.
[293] L. Liu, Y. Jiang, H. Zhao, J. Chen, J. Cheng, K. Yang, Y. Li, ACS Catal. 6 (2016) 1097–1108.
[294] F. Zhang, M. Wang, X. Zhu, B. Hong, W. Wang, Z. Qi, W. Xie, J. Ding, J. Bao, S. Sun, C. Gao, Appl. Catal. B Environ. 170-171 (2015) 215–224.
[295] A. Maira, J. Coronado, V. Augugliaro, K.. Yeung, J.. Conesa, J. Soria, J. Catal. 202 (2001) 413–420.
[296] F. Fresno, M.D. Hernández-Alonso, D. Tudela, J.M. Coronado, J. Soria, Appl. Catal. B Environ. 84 (2008) 598–606.
[297] G. Liu, N. Hoivik, K. Wang, H. Jakobsen, Sol. Energy Mater. Sol. Cells 105 (2012) 53–68.
[298] T. Kandemir, M.E. Schuster, A. Senyshyn, M. Behrens, R. Schlögl, Angew. Chemie - Int. Ed. 52 (2013) 12723–12726.
[299] N. Cherkasov, A.O. Ibhadon, P. Fitzpatrick, Chem. Eng. Process. Process Intensif. 90 (2015) 24–33.
[300] R. Lan, J.T.S. Irvine, S. Tao, Int. J. Hydrogen Energy 37 (2012) 1482–1494.
[301] L. Forni, Pernicone, CATALYSTS FOR AMMONIA SYNTHESIS, 2002.
[302] B. Lin, Y. Qi, Y. Guo, J. Lin, J. Ni, Catal. Sci. Technol. 5 (2015) 2829–2838.
[303] M. Karolewska, E. Truszkiewicz, B. Mierzwa, L. Keopiński, W. Raróg-Pilecka, Appl. Catal. A Gen. 445-446 (2012) 280–286.
[304] C. Fernández, C. Pezzotta, E.M. Gaigneaux, N. Bion, D. Duprez, P. Ruiz, Catal. Today 251

(2015) 88–95.
[305] K. Narasimharao, P. Seetharamulu, K.S. Rama Rao, S.N. Basahel, J. Mol. Catal. A Chem. 411 (2015) 157–166.
[306] Z. Lendzion-Bieluń, R. Jdrzejewski, E. Ekiert, W. Arabczyk, Appl. Catal. A Gen. 400 (2011) 48–53.
[307] D. Carpenter, K. Maloney, SYSTEM AND METHOD FOR AMMONIA SYNTHESIS, 2012.
[308] D.E. Brown, T. Edmonds, R.W. Joyner, J.J. McCarroll, S.R. Tennison, Catal. Letters 144 (2014) 545–552.
[309] Z. Kowalczyk, S. Jodzis, W. Raróg, J. Zieliński, J. Pielaszek, Appl. Catal. A Gen. 173 (1998) 153–160.
[310] É.S. Van-Dal, C. Bouallou, J. Clean. Prod. 57 (2013) 38–45.
[311] D.-H. Jang, H.-T. Kim, C. Lee, S.-H. Kim, Int. J. Hydrogen Energy 38 (2013) 6021–6026.
[312] M.B. Nikoo, N. Mahinpey, Biomass and Bioenergy 32 (2008) 1245–1254.
[313] S. Srinivas, S.M. Mahajani, R.K. Malik, Ind. Eng. Chem. Res. 49 (2010) 9673–9692.
[314] M. Khoshnoodi, Y.S. Lim, Fuel Process. Technol. 50 (1997) 275–289.
[315] A. Tripodi, M. Compagnoni, R. Martinazzo, G. Ramis, I. Rossetti, Catalysts 7 (2017) 159.
[316] B.Y. Yu, I.L. Chien, Ind. Eng. Chem. Res. 54 (2015) 10073–10087.
[317] P. Arora, A.F.A. Hoadley, S.M. Mahajani, A. Ganesh, Ind. Eng. Chem. Res. 55 (2016) 6422–6434.
[318] J. Andersson, J. Lundgren, Appl. Energy 130 (2014) 484–490.
[319] A. Aráujo, S. Skogestad, Comput. Chem. Eng. 32 (2008) 2920–2932.
[320] N. Pernicone, F. Ferrero, I. Rossetti, L. Forni, P. Canton, P. Riello, G. Fagherazzi, M. Signoretto, F. Pinna, Appl. Catal. A Gen. 251 (2003) 121–129.
[321] I. Rossetti, L. Forni, Appl. Catal. A Gen. 282 (2005) 315–320.
[322] I. Rossetti, N. Pernicone, L. Forni, Catal. Today 102-103 (2005) 219–224.
[323] J.R. Jennings, Catalytic Ammonia Synthesis, 1991.
[324] L.J. Gillespie, J.A. Beattie, 36 (1930) 743–753.
[325] D.C. Dyson, J.M. Simon, Ind. Eng. Chem. Fundam. 7 (1968) 605–610.
[326] H. Liu, Ammonia Synthesis Catalysts, 2013.
[327] M. Compagnoni, A. Tripodi, A. Di Michele, P. Sassi, M. Signoretto, I. Rossetti, Int. J. Hydrogen Energy (2017) in press.
[328] M. Compagnoni, A. Tripodi, I. Rossetti, Appl. Catal. B Environ. 203 (2017) 899–909.
[329] M. Compagnoni, E. Mostafavi, A. Tripodi, N. Mahinpey, I. Rossetti, ACS Sustain. Chem. Eng. (2017) submitted.
[330] M. Compagnoni, S.A. Kondrat, C.E. Chan-Thaw, D.J. Morgan, D. Wang, L. Prati, A. Villa, N. Dimitratos, I. Rossetti, ChemCatChem 8 (2016) 2136–2145.
[331] F. Galli, M. Compagnoni, D. Vitali, C. Pirola, C.L. Bianchi, A. Villa, L. Prati, I. Rossetti, Appl. Catal. B Environ. 200 (2017) 386–391.

6.1. Journal Publications by Matteo Compagnoni

- **M. Compagnoni**, A. Tripodi, E. Mostafavi, N. Mahinpey, I. Rossetti: "Techno-economic analysis of a bioethanol to hydrogen centralized plant" Energy & Fuels (2017) in press
- **M. Compagnoni***, A. Tripodi, E. Mostafavi, N. Mahinpey, I. Rossetti: "Hydrogen Production by Steam Reforming of Bio-ethanol: Process Design and Economic Assessment" DGMK-Tagungsberich, (2017) in press
- **M. Compagnoni**, A. Tripodi, A. Di Michele, P. Sassi, M. Signoretto, I. Rossetti: "Low Temperature Ethanol Steam Reforming for process intensification: new Ni/M_xO-ZrO_2 active and stable catalysts prepared by Flame Spray Pyrolysis", International Journal of Hydrogen Energy, in press (2017)
- A. Tripodi, D. Manzini, **M. Compagnoni**, G. Ramis, I. Rossetti: "Alternative Integrated Distillation Strategies for the Purification of Acetonitrile from Ethanol Ammoxidation", Journal of Industrial and Engineering Chemistry, in press (2017)
- A. Tripodi, **M. Compagnoni**, G. Ramis, I. Rossetti: "Pressure-swing or extraction-distillation for the recovery of pure acetonitrile from ethanol ammoxidation process: A comparison of efficiency and cost", Chemical Engineering Research and Design, 2017, 127 (2017) 92-102
- A. Tripodi, **M. Compagnoni**, G. Ramis, I. Rossetti: "Process simulation of hydrogen production by steam reforming of diluted bioethanol solutions: Effect of operating parameters on electrical and thermal cogeneration by using fuel cells", International Journal of Hydrogen Energy, 42 (2017) 23776-23783
- I. Rossetti, **M. Compagnoni**, G. De Guido, L. A. Pellegrini, G. Ramis, S. Dzwigaj; "Ethylene Production From Diluted Bioethanol Solutions", The Canadian Journal of Chemical Engineering, 95 (2017) 1752-1759
- A. Olivo, E. Ghedini, M. Signoretto, M. Compagnoni, I. Rossetti, "Liquid vs. gas phase CO_2 photoreduction process: which is the effect of reaction medium?" Energies, 10 (2017) 1394
- F. S. Freyria, **M. Compagnoni**, I. Rossetti, M. Piumetti, G. Ramis, B. Bonelli "Pure and Fe-Doped Mesoporous Titania Catalyse the Oxidation of Acid Orange 7 by H_2O_2 under Different Illumination Conditions: Fe Doping Improves Photocatalytic Activity under Simulated Solar Light", Catalysts, 7 (2017) 213
- I. Rossetti, **M. Compagnoni**, G. Ramis, F. S. Freyria, M. Armandi, B. Bonelli; "Development of Unconventional Photocatalytic Reactors and Processes for the Abatement of Harmful N-containing Pollutants", Chemical Engineering Transactions, 57 (2017) 319-324
- **M. Compagnoni***, G. Ramis, F. S. Freyria, M. Armandi, B. Bonelli, I. Rossetti; "Innovative Photoreactors for Unconventional Photocatalytic Processes", Rendiconti dei Lincei, 28 (2016) 151-158
- A. Tripodi, **M. Compagnoni**, R. Martinazzo, G. Ramis, I. Rossetti: "Process simulation for the design and scale up of heterogeneous catalytic process: Kinetic modelling issues", Catalysts, 2017, 7 (2017) 159
- I. Rossetti, **M. Compagnoni**, E. Finocchio, G. Ramis, A. Di Michele, Y. Millot, S. Dzwigaj; "Ethylene production via catalytic dehydration of diluted bioethanol: a step towards an integrated biorefinery", Applied Catalysis B: Environmental, 210 (2017) 407-420
- G. Ramis, I. Rossetti, A. Tripodi, **M. Compagnoni**, "Diluted bioethanol solutions for the production of hydrogen and ethylene", Chemical Engineering Transactions, 57 (2017) 1663-1668
- **M. Compagnoni**, A. Tripodi, I. Rossetti, "Parametric Study and Kinetic Testing for Ethanol Steam Reforming", Applied Catalysis B: Environmental 203 (2017) 899-909

- **M. Compagnoni**, G. Ramis, F. S. Freyria, M. Armandi, B. Bonelli, I. Rossetti, "Photocatalytic processes for the abatement of N-containing pollutants from waste water. Part 1: Inorganic pollutants", Journal of Nanoscience and Nanotechnology 17 (2016) 3632-3653
- **M. Compagnoni***, S. A. Kondrat, C. E. Chan-Thaw, D. J. Morgan, D. Wang, L. Prati, A. Villa, N. Dimitratos, I. Rossetti, "Spectroscopic Investigation of Titania Supported Gold Nanoparticles Prepared by a Modified DP Method for the Oxidation of CO", ChemCatChem, 8 (2016) 2136-2145
- A. Tripodi, **M. Compagnoni**, I. Rossetti, "Kinetic Modeling and Reactor Simulation for Ethanol Steam Reforming, ChemCatChem, 8 (2016) 3804 – 3813
- I. Rossetti, **M. Compagnoni**, E. Finocchio, G. Ramis, A. Di Michele, A. Zucchini, S. Dzwigaj, "Syngas Production via Steam Reforming of Bioethanol over Ni-BEA Catalysts: a BTL Strategy", International Journal of Hydrogen Energy, 41 (2016) 16878-16889
- F. S. Freyria, M. Armandi, **M. Compagnoni**, G. Ramis, I. Rossetti, B. Bonelli, "Catalytic and photocatalytic processes for the abatement of N-containing pollutants from wastewater. Part 2: Organic pollutants", Journal of Nanoscience and Nanotechnology 17 (2016) 3654-3672
- F. Galli, **M. Compagnoni**, Davide Vitali, Carlo Pirola, Claudia L. Bianchi, Alberto Villa, Laura Prati, Ilenia Rossetti, "CO_2 Photoreduction at High Pressure to both Gas and Liquid Products over Titanium Dioxide, Applied Catalysis B: Environmental, 200 (2016) 386-391
- **M. Compagnoni**, J. Lasso F., A. Di Michele, I. Rossetti, "Flame pyrolysis prepared catalysts for the steam reforming of ethanol", CatSci&Techn., 6 (2016) 6247-6256
- A. Comazzi, C. Pirola, A. Di Michele, **M. Compagnoni**, F. Galli, I. Rossetti, F. Manenti, C.L. Bianchi, "Flame Spray Pyrolysis as fine preparation technique for stable Co and Co/Ru based catalysts for FT process", Appl. Catal. A: General, 520 (2016) 92-98
- I. Rossetti, **M. Compagnoni**, "Chemical reaction engineering, process design and scale up issues at the frontier of synthesis: flow chemistry", Invited Review, Chem. Eng. J., 296 (2016) 56-70
- I. Rossetti, A. Villa, **M. Compagnoni**, L. Prati, G. Ramis, C. Pirola, C.L. Bianchi, W. Wang, D. Wang, "CO_2 photoconversion to fuels under high pressure: effect of TiO_2 phase and of unconventional reaction conditions", CatSci&Techn., 5 (2015) 4481
- I. Rossetti, J. Lasso, **M. Compagnoni**, G. De Guido, L. Pellegrini. "H_2 production from bioethanol and its use in fuel cells", Chemical Engineering Transactions, 43 (2015) 229
- I. Rossetti, **M. Compagnoni**, M. Torli, "Process simulation and optimisation of H_2 production from ethanol steam reforming and its use in fuel cells. 1. Thermodynamic and kinetic analysis", Chemical Engineering Journal, 281 (2015) 1024-1035
- I. Rossetti, **M. Compagnoni**, M. Torli, "Process simulation and optimization of H_2 production from ethanol steam reforming and its use in fuel cells. 2. Process analysis and optimizations", Chemical Engineering Journal, 281 (2015) 1036-1044
- A. Comazzi, C. Pirola, A. Di Michele, **M. Compagnoni** , F. Galli, S. Cane, F. Manenti, I. Rossetti, C.L. Bianchi, "Flame Spray Pyrolysis Synthesized Co and Co/Ru Based Catalysts for the Thermochemical GTL – Fischer Tropsch Process", DGMK-Tagungsberich, (2015) 197-204
- V. Nichele, M. Signoretto, F. Pinna, E. Ghedini, **M. Compagnoni**, I. Rossetti, G. Cruciani, A. Di Michele, "Bimetallic Ni-Cu catalysts for the low-temperature ethanol steam reforming: importance of metal-support interactions", Catal. Lett., 145 (2015) 549

6.2. Conference Presentations by Matteo Compagnoni

1) **Petrochemistry and Refining in a Changing Raw Materials Landscape (DGMK),** 9-11 October 2017, Dresden (GE): "Hydrogen Production by Steam Reforming of Bioethanol: Catalytic Tests and Process Design" (oral presentation)
2) **Europacat, 13th European Congress of Catalysis,** 27-31 August 2017, Florence, (IT): "Innovative photoreactors to remove N-containing pollutants from water" (oral presentation); **"**Kinetic analysis and reactor design of ethanol steam reforming" (poster display by Antonio Tripodi); **"**Process simulation for the production of hydrogen and ethylene: exploitation of diluted 2nd generation bioethanol solutions as poorly expensive raw material" (oral presentation by Ilenia Rossetti); Chairman of the session: Catalysis for biomass use
3) **International Conference on Chemical & Process Engineering (ICheaP13),** 28-31 May 2017, Milan (IT): "Development of Unconventional Photocatalytic Reactors and Processes for the Abatement of Harmful N-containing Pollutants" (oral presentation); "Diluted bioethanol solutions for the production of hydrogen and ethylene" (co-author of the oral presentation made by A. Tripodi)
4) **Merck Young Chemists Symposium International Conference,** 25-27/Oct/2016, Rimini (IT): "Innovative Photoreactors for Unconventional Sustainable Processes" (Oral Presentation); Speaker and organizer of the conference.
5) **GRICU Italian Engineering National Congress,** 12-14/Sep/2016, Anacapri , NA (IT): "Ethylene Production from Diluted Bioethanol Solutions", I. Rossetti, M. Compagnoni, E. Finocchio, G. Ramis, G. De Guido, L. Pellegrini, S. Dzwigajd (Poster display); "Optimization of CO_2 capture in a natural gas-fired power plant" G. De Guido, M. Compagnoni, L. A. Pellegrini, I. Rossetti (Oral presentation by G. De Guido)
6) **6th EuCheMS Chemistry Congress**, 11-15/Sep/2016, Seville (ES): "CO_2 Photoconversion to Fuels and Chemicals under High Pressure", M. Compagnoni, A. Olivo, F. Galli, A. Villa, C. Pirola, L. Prati, M. Signoretto, N. Dimitratos, I. Rossetti. (oral presentation); Recived grant for participation from the Industrial Chemistry Division (Società Chimica Italiana)
7) **Forum Nazionale dei Giovani Ricercatori di Scienza e Tecnologia dei Materiali (INSTM)**, 11-13/Jul/2016, Ischia (IT): "Flame Synthesized Catalysts for Hydrogen-Enriched Syngas Production by Low Temperature Steam Reforming" M. Compagnoni, J. Lasso, A. Di Michele, I. Rossetti (oral presentation); Recived grant for participation
8) **Accademia Nazionale dei Lincei: Concepts in Catalysis: From Heterogeneous to Homogeneous and Enzymatic Catalysis,** 25-26/Feb/2016, Rome (IT): International conference organized by Accademia Nazionale dei Lincei – Fondazione "Guido Donegani"; Received a grant for the participation
9) **I Congresso Nazionale Enerchem-1,** 18-20/Feb/2016, Florence (IT): "Steam Reforming of crude bio-ethanol for hydrogen production over FP catalysts" M. Compagnoni, J. Lasso, A. Di Michele, I. Rossetti (poster display). Received a grant for the participation
10) **XV Sigma Aldrich Young Chemists Symposium,** 27-29/Oct/2015, Rimini (IT): "Flame Spray Pyrolysis: catalysts for the Steam Reforming of bio-ethanol" M. Compagnoni, I. Rossetti, J. Lasso, V. Nichele, M. Signoretto (oral presentation)
11) **XIX Congresso Nazionale Divisione di Chimica Industriale** (SCI), 14-16/Sep/2015, Salerno (IT): "High pressure photoreactor for CO_2 conversion to fuels", M. Compagnoni, I. Rossetti, A. Villa, C. Pirola, L. Prati, G. Ramis, D. Wang (oral presentation); Received a grant for the participation
12) **Gold Conference**, 27-29/Jul/2015, Cardiff University (UK)
13) **M4 Colloids Symposium,** 2/Jul/2015, University of Bristol (UK)
14) **14th Annual Cardiff Chemistry Conference,** 11-12/May/2015, Cardiff (UK)

15) **Offshore Mediterranean Conference**, 25-27/Mar/2015, Ravenna (IT): "Production of renewable hydrogen by reformation of bioethanol", M. Compagnoni (oral presentation)

16) **13° Sigma Aldrich Young Chemists Symposium,** SCI, 28/Oct/2014, Riccione (IT): "Flame pyrolysis prepared catalysts for the steam reforming of ethanol: effect of support basicity", M. Compagnoni, J. Lasso, I. Rossetti (poster display)

17) **XXV Congresso SCI**, 7/Sep/2014, Arcavacata di Rende (IT): "Flame-made ZrO_2 supported catalysts for the steam reforming of ethanol", M. Compagnoni, J. Lasso, I. Rossetti (poster display); "Steam reforming of second generation bioethanol", J. Lasso, M. Compagnoni, I. Rossetti (oral presentation); Received a grant for the participation

7. Acknowledgments

Questo progetto di dottorato è il prodotto di una reazione durata tre anni, in cui la mia persona rappresenta il reagente principale, ma che non sarebbe potuta avvenire in assenza degli altri reagenti, del solvente, delle condizioni operative e del catalizzatore.
Gli altri preziosi reagenti sono stati tutti i ragazzi che si sono succeduti come tesisti triennali e magistrali sul progetto, e voglio ricordarli tutti proprio perché sono stati essenziali. In ordine cronologico: Nicola Bagnaresi, Eleonora Fumagalli, Davide Vitali, Luca Ressel, Pierluigi Moimare, Andrea Villa, Alberto Riva, Gaia Mascetti, Anna Dell'Angelo, Matteo Ferrando, Antonio Pizzonia, Dario Manzini, Veronica Pellegatta, Veronica Praglia.
Il solvente è stato l'insieme di persone che anche se non ha contribuito direttamente al progetto, mi ha aiutato nei momenti critici, sia pratici che di svago che di supporto.
Grazie a tutti gli amici dei sotterranei (di cui anche io orgogliosamente faccio parte): Marco, Sebastiano, Mavi e Ivan.
Grazie agli amici e compagni d'avventura Alberto e Veronica, la nostra amicizia e le nostre serate saranno sicuramente una cosa che mi mancherà, ma che proprio per questo continueremo a mantenere pur non vedendoci tutti i giorni.
Grazie a Josè, PhD senior con cui ho condiviso la prima metà del dottorato e in cui ho trovato sempre un aiuto nel momento del bisogno.
Grazie ad Antonio, Giovanni ed Elnaz per la collaborazione e condivisione in questi anni.
Grazie Guido, spero di trovare in futuro persone del tuo calibro morale oltre che professionale.
Grazie agli amici di Cardiff, dove ho passato cinque mesi eccezionali.
Grazie agli amici canadesi e iraniani durante il mio soggiorno a Calgary, i -25°C provati si sono sentiti di meno.
Il catalizzatore di tutto è stata sicuramente Ilenia, professoressa-capo-amica, che ha condiviso con me gioie e dolori, vittorie e sconfitte.
Jack Ma, fondatore di una grande multinazionale asiatica, durante un congresso internazionale ha voluto condividere con dei giovani dei consigli per una carriera importante (nel lavoro e nella vita), raccomandando prima dei trent'anni di lavorare con capi da cui imparare oltre che il lavoro soprattutto la passione, il sogno, il fine. E questo è molto più importante di qualsiasi esperienza tecnica, perché senza idee importanti le competenze sono mero progresso materiale. Grazie al mio supervisor questo stadio per me si può dire più che raggiunto, e di questo ne sarò sempre grato.
Dedico questo lavoro a mia madre e mio padre, per il loro supporto e amore in questi anni.
L'ultima frase è per te Chiara, perché l'impegno, la dedizione e ovviamente anche questo minimo lampo di creatività nei ringraziamenti, sono stati possibili grazie a te e alle parole d'ogni giorno.

Matteo Compagnoni